# The Effect of Impurities on Permeance through Chabazite Zeolite Membranes

by

Nicholas Odell Chisholm

B.S., Cornell University, 2010

A thesis submitted to the

Faculty of the Graduate School of the

University of Colorado in partial fulfillment

of the requirements for the degree of

Doctor of Philosophy

Department of Chemical and Biological Engineering

2017

This thesis entitled:
The Effect of Impurities on Permeance through Chabazite Zeolite Membranes
written by Nicholas O. Chisholm
has been approved for the Department of Chemical and Biological Engineering

_____
Professor John L. Falconer

_____
Professor Richard D. Noble

Date _____

The final copy of this thesis has been examined by the signatories, and we find that both the content and the form meet acceptable presentation standards of scholarly work in the above-mentioned discipline

Chisholm, Nicholas O. (Ph.D., University of Colorado, Chemical and Biological Engineering)

The Effect of Impurities on Permeance through Chabazite Zeolite Membranes

Thesis directed by Professor John L. Falconer and Professor Richard D. Noble

Zeolite membranes selectively permeate gases based on differences in size, diffusivity, and loading. The chabazite zeolites SAPO-34 and SSZ-13 have 0.38-nm pores, which make them suitable for separating $CO_2$ (0.33-nm kinetic diameter) from $CH_4$ (0.38 nm) for natural gas purification. Natural gas also contains ethane, propane, butane, and higher hydrocarbon impurities that can adsorb in the membranes and affect their performance.

We studied the effect of small alkanes on $H_2/N_2$ separations in SAPO-34 by adding ethane, propane, or n-butane to the feed. Propane reduced the permeance of both gases, but it reduced the $H_2$ permeance less than the $N_2$ permeance, so that the selectivity increased from about 4 to about 9. n-Butane had a similar effect, but ethane caused no change in selectivity. Reduced $H_2$ loading due to competitive adsorption would decrease $H_2/N_2$ selectivity if competitive adsorption were the dominant mechanism. Therefore, diffusion plays a significant role and the alkanes must have decreased $N_2$ diffusivity more than $H_2$ diffusivity.

We studied the effects of toluene, which is too large (0.59 nm) to diffuse into zeolite pores, on $CO_2$ and $N_2$ permeance through SAPO-34 membranes. When 0.65 mol% toluene was added to the feed, the $CO_2$ permeance decreased by 45% and the $N_2$ permeance decreased by 50% at 172-kPa pressure. At 10-kPa feed pressure, 8.5% toluene decreased $CO_2$ permeance by 20%. Binary isotherm models predict that competitive adsorption between toluene and $CO_2$ on the external surface significantly reduced the $CO_2$ coverage, and thus the driving force for $CO_2$ transport.

Finally, we measured the effect of $C_1$ through $C_4$ alkanes on $CO_2$ permeance through SSZ-13 membranes. Propane and n-butane have kinetic diameters (0.43 nm) larger than the SSZ-13 pores, but they adsorb to high loadings in SSZ-13 crystals because these molecules are flexible. Methane decreased $CO_2$ permeance by 5%, and ethane decreased $CO_2$ permeance by 45% at the same concentration. Propane, however, only decreased $CO_2$ permeance by 10%, and n-butane decreased the permeance by 15%. Apparently, the larger alkanes did not adsorb into the SSZ-13 pores, likely due to an altered external pore structure, and propane and n-butane only reduced $CO_2$ permeance by adsorbing on the external surface.

## Dedication

To my parents, Joan Odell and Dexter Chisholm, for instilling in me a love of science, and to my wife, Carly Chisholm, for her love and support throughout this chapter of our lives.

# Acknowledgements

I would like to thank my advisors John Falconer and Rich Noble for their guidance in completing this thesis. They have taught me much about experimental design, the merits of efficient project management, effective presenting of scientific results, and the wonderful world of zeolites. I would also like to thank Associate Professor Hans Funk, who I think of as an advisor and mentor. Hans has taught me so much about building, running, troubleshooting, modifying, and troubleshooting flow systems, reactors, and the electronics/programming that controls them; as well as fundamental (and practical) lab science, and technical writing. I couldn't have done this without you, Hans. I also thank the rest of my committee members, Alan W. Weimer, Prashant Nagpal, and Wei Zhang, for their helpful feedback over the years.

I have had the pleasure of training and/or working with several undergrads and two high school students. Thank you Kirsten Runyan for all your hard work on solar cell construction and membrane testing; Merritt Diaz, Grace Anderson, and Jordan McNally, for your work with low pressure membrane testing; Michael Chen, for your work measuring adsorption isotherms; Peter Chen for your work programming and running the MLD reactor; Michael Mulder and Nathan Edwards, for your work with high pressure membrane testing.

I would like to thank the grad students and post-docs that I have worked with. Thank you Matthias Young and Daniel Higgs from the George group in Chemistry for expertise on MLD growth. Thank you Will McDanel and Matt Cowan from the Gin and Noble group for your collaboration on a polymer membrane project. Thank you to the joint group members Troy Gould and Staci van Norman for teaching me how to give group presentations. Thank you Alan Izar for empathizing with challenging projects, and coating zeolite samples with your MLD reactor. Thank

you Ignacio Castellanos for being the best group member a grad student could ask for. I also thank the visiting students from China, Ting Wu and Yiwei Luo, for making membranes, taking SEM images and XRD scans, and spending your time abroad in our lab, and the visiting Chinese professors, Wein-Duo Yang and Yinxiao Yan, all for teaching me that research brings people together and friendships can be made across continents.

And thank you to my friends and family for keeping me going. My time in Boulder, CO has been very special because of you. Mom, Dad, Mitch, and all the in-laws, thanks for staying in close touch while we were states away. Lastly, and mostly, thank you to my wife Carly. Your support means the world to me.

# Contents

# Tables

# Figures

# Chapter 1 Introduction

## 1.1 Thesis Summary

This thesis investigates the effects of hydrocarbon impurities on the permeance of small gases through Chabazite membranes and the effect of these impurities on mixture selectivities. The first chapter introduces zeolite crystals, zeolite membranes, diffusion of gases through pores, and surface adsorption, and provides a brief review of the literature related to SAPO-34 and SSZ-13 membranes. The second chapter describes experimental methods of zeolite membrane synthesis, and the gas flow systems used to measure membrane performance. The third chapter discusses the effects of propane, ethane, and n-butane on $H_2$ and $N_2$ permeances and separation selectivities through SAPO-34 membranes. Propane increased the $H_2/N_2$ selectivity by decreasing the $N_2$ diffusivity more than the $H_2$ diffusivity, and n-butane had a similar effect. The fourth chapter discusses the effect of toluene and $SF_6$ on $CO_2$ and $N_2$ permeance through SAPO-34 membranes. Toluene, which only adsorbs on the external surface of the membrane, significantly decreased $CO_2$ and $N_2$ permeances, and a competitive adsorption model is used to give a thermodynamic explanation for the observed changes. The fifth chapter discusses the effects of methane, ethane, propane, n-butane, and iso-butane on $CO_2$ permeance through SSZ-13 membranes. All of these hydrocarbons decreased $CO_2$ permeance; methane and ethane adsorbed in the zeolite pores, whereas the effects of propane and butane were primarily due to external adsorption at room temperature. The sixth chapter summarizes the findings, presents concluding remarks, and outlines recommendation for future studies.

## 1.2 Zeolite Crystals

### 1.2.1 Structure and chemistry

Zeolites are porous, crystalline metal-oxides with uniform pores the size of small molecules. Historically, only aluminosilicate structures with these features were considered zeolites, but the definition has been expanded in the *Atlas of Zeolite Structure* to include related materials with elements other than Si and Al for the backbone (T-atoms), including phosphorous, cobalt, gallium, zinc, arsenic, and titanium [1]. Some zeolites do not even include silicon (AlPO) or aluminum (Ti-beta). Zeolites are categorized by their crystal structures. The structure family, or framework type, is often named after a naturally-occurring mineral with the same crystal structure. Zeolite crystal-structures are experimentally determined by X-ray diffraction (XRD), and this technique is typically used to identify or confirm the correct crystal phase after synthesizing zeolites. The Structure Commission of the International Zeolite Association lists over 200 zeolite frameworks [2], and often, the same framework structure can be formed with many variations in the molecular composition of the framework atoms. Zeolites lattices are often not charge-neutral due to mismatches in valencies of the structure atoms, and these charges are compensated by counter-ions incorporated in the zeolite cages. These counter-ions can be ion-exchanged to modify the pore or cage geometries and chemical properties of the zeolites. The main framework of interest for this thesis is Chabazite (CHA), which includes both SAPO-34 and SSZ-13 zeolites.

Figure 1.1 shows a schematic of the chabazite unit cell, which has a pore and cage structure with rings of 8, 6, and 4 T-atoms. Each T-atom is covalently bonded to 4 oxygen atoms, and each oxygen is bonded to 2 T-atoms. In SAPO-34 and SSZ-13, the rings of 8 T-atoms define pores with 0.38-nm diameter. These pores connect cages, with cross sections close to 0.74 nm, in a 3D

network. Even the smallest gases such as helium cannot fit through the 6- or 4-member rings, and the 8-member rings limit of the size of molecules that can enter the zeolite pores.

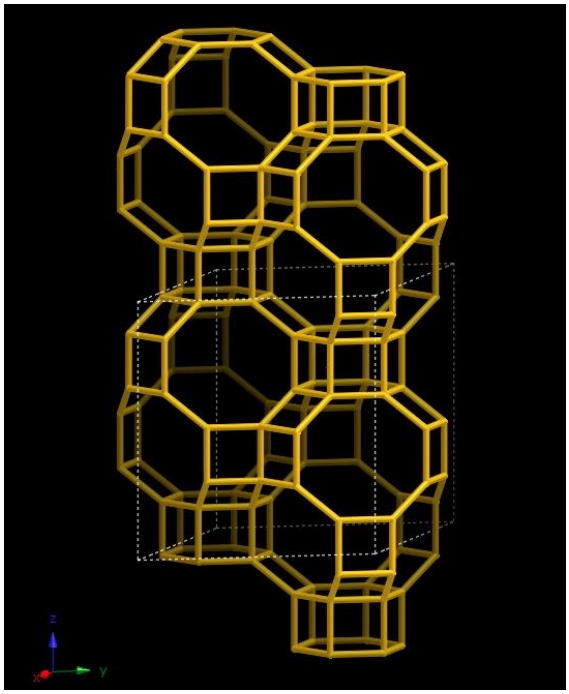

**Figure 1.1.** Structure of chabazite framework showing the T-atoms in the crystal [2]. Cages are formed from rings of 4, 6, or 8 T-atoms and are connected in a 3D network.

SAPO-34 is named after the elements in its structure (Si, Al, P, and O) and the number indicates the order in a list of similar materials when it was first synthesized by Flanigan at Union Carbide in 1984. The chemical formula is $Si_xAl_yP_zO_2$ where $x + y + z = 1$. Typically x is 0.01 - 0.98, y is 0.01 – 0.6, and z is 0.01 – 0.52 [3]. SSZ-13 was named for "Socal Silica Zeolites" by workers at Chevron, and it has the chemical formula $Si_xAl_yO_2$ where $x + y = 1$ and $x > 0.8$. Crystalline $SiO_2$ is electrically neutral, whereas aluminum T-atoms in the structure have a net negative change, and phosphorous T-atoms in the structure have a net positive charge. Both the SAPO-34 and SSZ-13 frameworks are negatively charged as a result of the unbalanced ratio of T-atoms with different valences and thus contain positive counter-ions to balance the charge,

typically hydrogen ions. The $H^+$ ions within the zeolite cages can be exchanged with other counter-ions to affect the pore geometry and chemical properties, but the present work was carried out with SAPO-34 and SSZ-13 membranes in the $H^+$ form.

This thesis work focuses on zeolite membranes, and to a lesser extent on zeolites as adsorbents, but zeolites are also widely used as catalysts and as an ion-exchange medium. The Bronsted acid sites of zeolites in their $H^+$ form are catalytically active, and zeolites can also be synthesized to incorporate catalytically-active metal sites. In addition to providing reaction sites, the small pores often result in enhanced reaction selectivity by sterically limiting reactant molecules, transition states, and/or products. Many hydrocarbon cracking and reforming processes use heterogeneous zeolite catalysts.

### 1.2.2 Molecular sieving and equilibrium adsorption

Molecules that are smaller than the zeolite pores can enter the cages and diffuse through the pore network whereas molecules that are larger than the pore openings are completely excluded. This discrimination between molecules on the basis of size (molecular sieving) provides major selectivity advantages for microporous materials with uniform pores over other separation materials such as polymers, which often rely solely on solution adsorption/diffusion differences or some less uniform porosity. The molecular kinetic diameter, which is based on diffusion behavior in the gas phase, is often used as a measure of molecular dimensions, but it may not be sufficient to determine if a molecule will be excluded from a microporous material. For example, propane has a kinetic diameter of 0.43 nm, which is larger than the 0.38-nm pores of SAPO-34, but it is sufficiently flexible to enter the pores, resulting in relatively high equilibrium loadings in the large cages [4].

Zeolites have high internal surface areas as a result of their large internal pore volume (as much as 25%) and therefore are able to adsorb large amounts of gases and vapors. The 'ideal' surface area of SAPO-34 based on the pore structure is about 600 $m^2/g$ [5,6] and that of SSZ-13 is about 700 $m^2/g$ [7], but the surface area can vary by several hundred $m^2/g$ depending on the synthesis method and degree of crystallinity. The amount of adsorbed molecules (or loading, typically in mol/g or $mol/m^2$) depends on the temperature, partial pressure, the type of zeolite, and the chemical properties of the adsorbate. Figure 1.2 shows the loading of several gases on SAPO-34 crystals at room temperature. At constant temperature, increasing the partial pressure of gas or vapor (or increasing the concentration of a species in solution) in contact with the zeolite increases the loading. Surface adsorption is an exothermic process that lowers the entropy of adsorbing molecules, so at constant partial pressure, increasing the temperature decreases the zeolite loading. Guest molecules adsorb because they interact with the zeolite surface through electrostatic interactions and/or hydrogen bonding. Polar molecules such as $CO_2$, and large molecules such as linear hydrocarbons with three or more carbon atoms, interact more strongly with the zeolite surface than smaller, non-polar species, have higher heats of adsorption, and have higher loadings for a given partial pressure and temperature. For some cases, entropic or steric effects are also important [8,9].

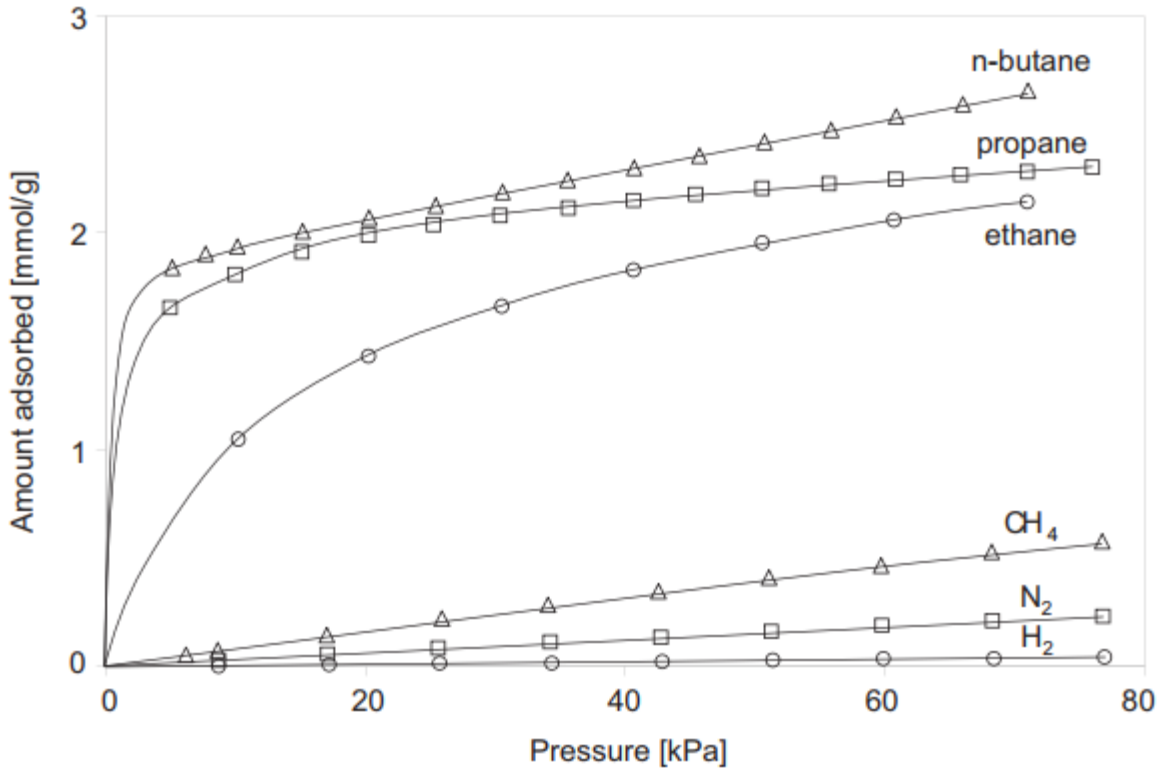


**Figure 1.2.** Adsorption isotherms of n-butane, propane, ethane, methane, nitrogen, and hydrogen on SAPO-34 crystals at room temperature [10].

Zeolites are commonly used as adsorbents for removing impurities such as water vapor and small hydrocarbons from mixtures of gases, or VOCs from aqueous solutions. Zeolites can also be used for selective adsorption separations by taking advantage of the different loading capacity for different molecules. For example, if a mixture of $C_2H_6$ and $N_2$ is introduced to an evacuated vessel that contains SAPO-34, more $C_2H_6$ adsorbs onto the zeolite than $N_2$ (Figure 1.2). After allowing time for diffusion into the pores, the bulk gas that is now enriched in $N_2$ can be removed, and the zeolite can then be heated to release $C_2H_6$-enriched gas. This process is known as pressure-swing adsorption and is used commercially for gas separations.

Adsorption occurs at different rates depending on the diffusivity of the adsorbate molecules in the adsorbent pores. For example, the equilibrium loadings shown in Figure 1.2 were measured by dosing a known amount of gas into a known volume that contains the zeolite sample and then measuring the equilibrium pressure. Pressures equilibrated within few minutes for each data point of the $H_2$ and $N_2$ isotherms, but propane and butane isotherms required several hours for equilibration for each measurement as a result of slow diffusion into the SAPO-34 pores. Equilibrium loadings are useful for designing adsorption systems and membranes, but the time to reach equilibrium must also be taken into account.

Adsorption isotherms can be described with kinetic models such as the Langmuir or BET equations where rates of adsorption and desorption depend on the surface coverage. The Langmuir model has the form:

$$\theta_i = \frac{q_i}{q_m} = \frac{K_{eq}^i P_i}{1 + K_{eq}^i P_i} \quad (1)$$

where $\theta$ is the fractional occupancy, $q$ is the loading, $q_m$ is the saturated loading, $K_{eq}$ is the temperature-dependent equilibrium constant, and $P$ is the partial pressure – all for species $i$. The BET isotherm, which is commonly used to model cryogenic $N_2$ adsorption to measure surface areas, adds more parameters to account for multilayer adsorption and follows a similar form. When two or more species adsorb on a surface, they compete for surface sites, increasing the total number of sites covered but decreasing the loading of the individual compounds compared to their single-component loadings at the same partial pressure. A strongly-adsorbing species thus can significantly reduce the loading of more weakly-adsorbing molecules. The binary Langmuir isotherm for species $i$ and $j$:

$$\theta_i = \frac{q_i}{q_m} = \frac{K_{eq}^i P_i}{1 + K_{eq}^i P_i + K_{eq}^j P_j} \quad (2) \qquad \theta_j = \frac{q_j}{q_m} = \frac{K_{eq}^j P_j}{1 + K_{eq}^i p_i + K_{eq}^j P_j} \quad (3)$$

describes this with reasonable accuracy for some binary mixtures. Ideal adsorbed solution theory (IAST) provides a more thermodynamically-consistent description of multicomponent adsorption and reflects experimental results with better accuracy for mixtures with ideal adsorption. The IAST is covered in detail in chapter 4.

### 1.2.3 Molecular diffusion

Molecular diffusion is the random motion of molecules in space due to elastic reflections by walls and other molecules. The average displacement is a function of the thermal and thus kinetic energy of the system [11]. Macroscopically, diffusion causes molecules to move following a gradient in the chemical potential. Diffusion in zeolites is often described as activated surface transport where adsorbed molecules move between adsorption sites by overcoming an activation energy barrier instead of moving freely in the zeolite cavities. Fick's Law assumes that transport is a linear function of the concentration gradient and can be applied to single-component diffusion in zeolites with reasonable accuracy:

$$\frac{\partial C}{\partial t} = D\frac{\partial^2 C}{\partial x^2} \quad (4) \qquad J = -D(C)\frac{dC}{dx} \quad (5)$$

where $C$ is concentration, $t$ is time, $D(C)$ is the diffusion coefficient which can be concentration-dependent, $x$ is the diffusion direction, and $J$ is the flux. Equation (4) is Fick's second law in one dimension that describes concentration changes as a function of time, and equation (5) is the solution of (4) for steady state. Fick's diffusion equations are less accurate for multicomponent systems because sufficiently-narrow channels restrict molecular motion, and cross-interference between different species is observed. For example, pore openings in CHA zeolites are too small to allow even small molecules to pass each other, but diffusion in the larger cages is less restricted and faster-diffusing species may pass slower diffusing molecules. When two or more species

diffuse through CHA channels, the slower molecules may inhibit the movement of faster-moving molecules, and faster compounds may speed up the diffusion of slower molecules [12], though these effects are stronger in zeolites with one-dimensional channels. Inter-species interactions are accounted for by the diffusion coefficients in the Maxwell-Stefan equations. The Maxwell-Stefan equations for molecular diffusion have been successfully applied to diffusion through zeolite pores [12,13]. The driving force for transport is a gradient in chemical potential, and inter-species diffusion coefficients address interaction and friction between the different diffusing molecules:

$$\frac{\nabla \mu_i}{RT} = \sum_{\substack{j=1 \\ j \neq i}}^{n} \frac{x_i x_j}{Đ_{ij}} \left( \vec{v}_j - \vec{v}_i \right) \quad (6)$$

where $\nabla$ is the vector differential operator, $\mu$ is chemical potential, $R$ is the gas constant, $T$ is temperature, $i$ and $j$ represent components $i$ and $j$, $n$ is the total number of components, $x$ is mole fraction, Đ is the Maxwell-Stefan diffusion coefficient, and $v$ is diffusion velocity. For diffusion in zeolites, one of the 'species' j can be taken as the zeolite adsorption sites. The chemical potential can be calculated from the adsorption loadings using adsorption models such as Langmuir or IAST. The approach to solving these equations to describe membrane transport is described in detail by Krishna et al. [14]. Multicomponent diffusion coefficients may be calculated from single-component diffusion data, and loading may be determined from single-component adsorption isotherms [15]. Even single component diffusion measurements are challenging, and diffusivities can vary strongly depending on the experimental technique used [17]. Diffusivities not only depend on the specific type of zeolite but also may vary from sample to sample. In addition, diffusion coefficients Đ often are strongly loading-dependent [16], and thus Maxwell-Stefan diffusion coefficients are not readily available.

If accurate transport parameters are not available for the Maxwell-Stefan approach, diffusion can be estimated with Fick's Law using intrinsic (or corrected) diffusion coefficients, $D_0$, that are defined for the gradient in chemical potential instead of the gradient in concentration. The Fickian diffusivities D are calculated from the corrected diffusivities with the Darken Equation, equation (9) [17]:

$$D_0 \frac{d\mu_i}{dx} = -J_i \quad (7)$$

$$D \frac{dq_i}{dx} = -J_i \quad (8)$$

$$D = D_0 \frac{d \ln P}{d \ln q} \quad (9)$$

where $P$ is the partial pressure and $q$ is the loading (proportional to $C$ in equations 3 and 4). This approach accounts for the non-linear relationship between chemical potential and concentration by using an isotherm model (e.g., Langmuir) to relate $P$ and $q$.

## 1.3 Membranes

### 1.3.1 Separation technologies

Industrial separations with membranes often require significantly less energy than other separation processes such as distillation or batch adsorption. The energy requirements are highest for traditional and cryogenic distillation where the feed mixtures are continuously evaporated and re-condensed in separation columns, either at cryogenic or elevated temperatures. Batch processes such as pressure- or temperature-swing adsorption with solid or liquid adsorbents require energy to desorb the selectively-removed molecules by heating or evacuation of the saturated adsorbent beds. Both membrane separators and pressure-swing adsorption systems consume less energy than separations that require phase changes, such as distillation. Typically, only electrically-operated

compressors and/or vacuum pumps are required to drive the separation with membranes, and membrane installations are less complex. Thus, depending on the specific challenges of a separation such as the required selectivity and availability of feasible membrane materials, membrane technologies may be more economical than traditional separation methods.

### 1.3.2 Classification of membranes

Membranes are essentially thin barriers that are selective on a nanometer or even sub-nanometer scale. In contrast to cell membranes in living organisms where some transport is active (pumped), commercial separation membranes for industrial applications passively separate molecules based on different rates of permeation. The thermodynamic driving force for movement across the membrane is differences in the chemical potential, which may be the result of differences in concentration or pressure between the feed/retentate (upstream) side and permeate (downstream) side. A wide variety of membranes materials have been reported in the literature for applications in chemical separations. Most focus is placed on organic polymers, but inorganic membrane materials such metals or a wide range of ceramic have also been studied intensively. Metal membranes such as those based on palladium have high selectivities for separating $H_2$ from other light gases because only $H_2$ can diffuse, dissociated in the form of protons, through the metal matrix. However, metal membranes are expensive and require high temperatures for operation. Dense polymer membranes are more widely used commercially for both gas and liquid separations including reverse osmosis, because of their low manufacturing cost. Particles larger than 5 nm can be removed from fluid streams with porous polymer membranes. Diffusion through polymer membranes is often described by a solution-diffusion mechanism where both solubility and mobility in the polymer matrix determines transport. Ceramic membranes, including zeolite membranes, are generally more expensive than polymer membranes but they are much more

chemically, thermally, and structurally stable. Ceramic membranes can be used in conditions that would melt or rupture polymer membranes, and for certain separations, molecular sieves can be much more selective and permeable than polymer membranes. Also ceramic membranes can have significant advantages at higher pressures where gases such as $CO_2$ swell many polymer membranes. The upper performance boundaries for currently-available polymer membranes can be illustrated in Robeson plots where selectivity is displayed as a function of permeability.

### 1.3.3 Zeolite membranes

Some of the zeolites that are useful for selective adsorption processes may be deposited as a continuous film of intergrown crystals on porous supports to form separation membranes. Zeolite membranes separate molecules based on differences in loading and diffusivity. Size and shape affect both loading, due to molecular sieving (sufficiently large molecules may be completely excluded), and diffusivity, due to steric hindrance in the narrow zeolite pores (larger molecules tend to diffuse slower). The loading is also affected by the interaction of the diffusing molecules with the zeolite pore walls, and strong interactions result in higher loadings. High fluxes require both high loadings and high diffusivities.

Zeolite membranes typically have some defects because complete intergrowth of the crystals that form the separation layer is difficult to achieve. These defects are often larger than the zeolite pores, and thus flux through the defects is less selective than the zeolite pore flux. Depending on the defect size, the defect flux may be due to Knudsen diffusion, where the permeance is proportional to the inverse square root of molecular weight, surface diffusion, or viscous flow. In this thesis, estimates for defect fluxes are based on Knudsen diffusion. Even though defect-free membranes are most desirable, membranes with defects may still be useful if the majority of the diffusion is through the zeolite pores so that the selectivities remain acceptable.

One of the main challenges for commercial application of zeolite membranes is scale-up because large-area membranes with few defects are difficult to synthesize. Several types of zeolite membranes have been synthesized on a laboratory scale (few $cm^2$) with both high fluxes and selectivities that often far exceed the best polymer membrane, but, with few exceptions (e.g., NaA zeolite membranes for pervaporation from Mitsui), successful scale-up has not been demonstrated to date. Because of the large potential for energy savings, membranes with zeolites and other types of molecular sieving materials as a separation layer are still actively investigated for applications such as natural gas separation or $CO_2$ capture from power plant flue gas. Since scale-up often results in more defects, techniques for post-synthesis treatments to close defects such as polymer depositions, coke depositions, and surface modification [18] are also of interest.

The zeolite membranes studied in this thesis were grown on tubular porous alumina supports. Figure 1.3 shows a schematic of the membrane module used for the gas separation experiments, and a close-up of the membrane cross-section with permeating species A and B. The flow system is described in detail in chapter 2. During separation measurements, a *feed* of two or more components enters one end of the tubular membrane. As the feed gases flow along the membrane surface, some of the molecules enter the zeolite layer and diffuse to the low-pressure permeate side. The permeating gas then leaves the membrane module as the *permeate*. Any components of the feed mixtures that do not permeate through the membrane are collected as the *retentate*. The permeate is enriched in the faster-permeating species, and, depending on the specific separation, either outlet stream may contain higher concentrations of the desired component.

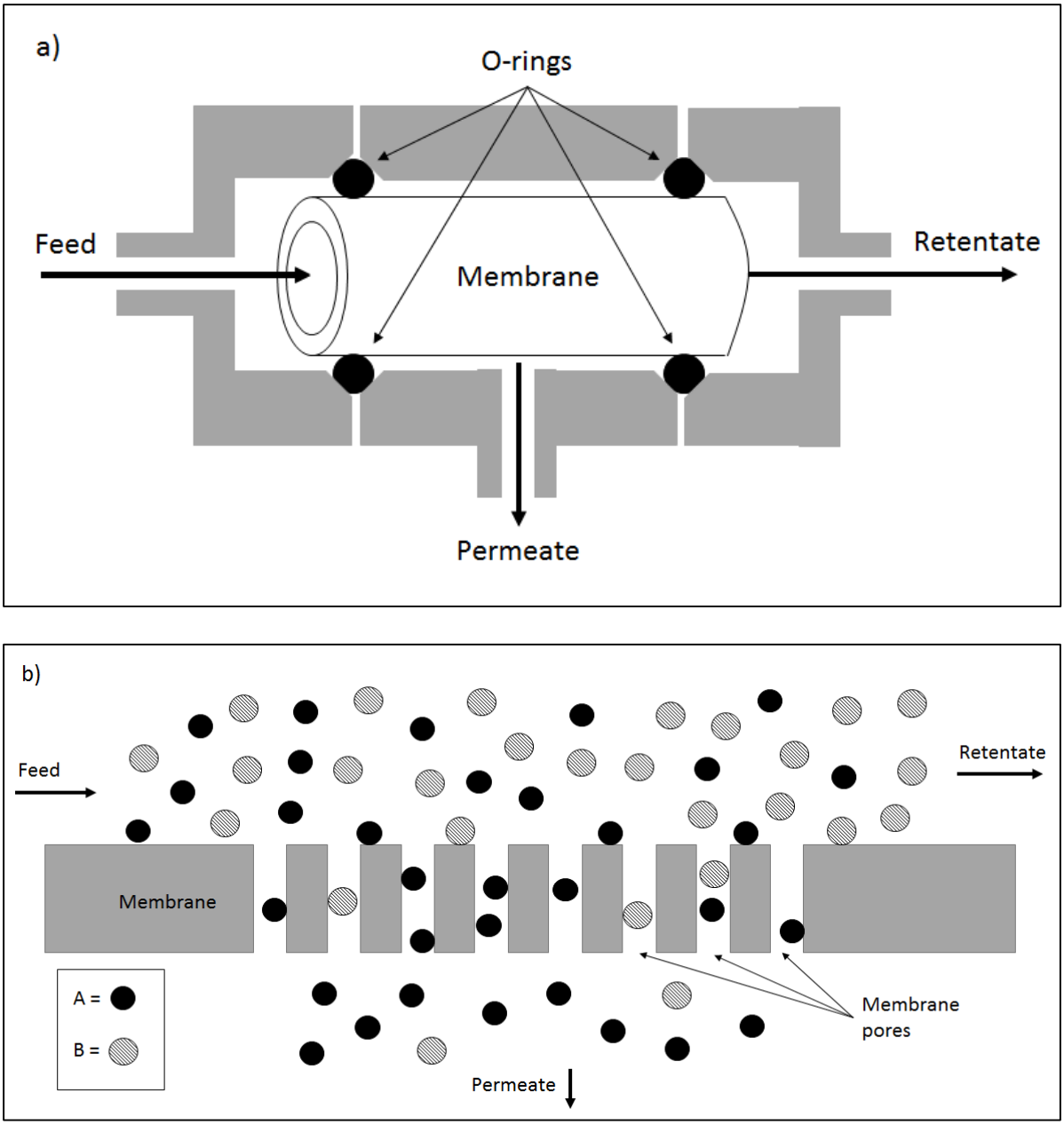


**Figure 1.3** a) A tubular membrane mounted in a membrane module with o-ring seals, b) Representation of the selective layer that preferentially permeates species *A* over species *B.*

The schematic in Figure 1.3b illustrates operation of a selective membrane. Species A is more permeable than species B and thus it passes through the membrane pores at a higher rate. The permeate is enriched in A and the retentate is depleted of A. The composition on the feed side changes as the feed is depleted of A in the direction of the feed flow, and thus the driving force for

transport changes. This change in driving force is addressed by using a log-mean concentration gradient (equation 11) to calculate permeances (flux normalized by driving force and surface area), as shown in equation 10. High permeances are desired because they decrease the membrane area necessary for a given flux and thus decrease the cost of the membrane installation. The separation selectivity determines the purity of the product streams, and for mixed gas feeds it is typically defined as the ratio of the permeances of the individual components (equation 12). The *ideal selectivity* is the ratio of single-component permeances, which are measured more easily than separation selectivities, and it is often used to identify the potential feasibility of a membrane. However, separation selectivities can be significantly different from ideal selectivities, depending on the specific interactions of the different species in the membrane pores, and thus separations selectivities are necessary to determine whether a membrane is capable to carry out a specific separation.

$$\mathcal{P}_i = \frac{\dot{m}_i}{A\,\Delta P_i} = \frac{J_i}{\Delta P_i} \quad (10)$$

$$\Delta P_{i,lm} = \frac{P_{i,f} - P_{i,r}}{\ln\left(P_{i,f} - P_{i,p}\right) - \ln\left(P_{i,r} - P_{i,p}\right)} \quad (11)$$

$$S_{A/B} = \frac{\mathcal{P}_A}{\mathcal{P}_B} \quad (12)$$

Equation 10 defines permeance, $\mathcal{P}$ for species $i$ where $\dot{m}$ is the mass flow rate, $A$ is membrane area, $P$ is the partial pressure, and $J$ is the flux. The gradient in partial pressure, $\Delta P_i$ is calculated from the log-mean pressure difference given in equation 11, where P is pressure and the subscripts $f$, $r$, and $p$ indicate feed, retentate, and permeate respectively. Equation 12 defines selectivity $S$ as the ratio of the permeances.

### 1.3.4 Natural gas purification

One of the main applications where CHA membranes have shown potential on a laboratory scale is the purification of natural gas to obtain sufficiently pure methane as an energy source for heating and electricity production, and as a precursor for specialty chemicals and hydrogen generation. World energy consumption continues to increase, and while renewable energy is the fastest-growing energy source (based on the fractional increase), fossil fuels account for over 75% of use and natural gas/methane is the fastest-growing fossil fuel [19]. In addition to methane, natural gas wells contain a significant fraction of $CO_2$, $N_2$, ethane, propane, and higher hydrocarbons, and the composition often varies from well to well. These components have to be removed from the methane before it meets regulatory specifications and can be stored or sent to a pipeline. Insufficient purity lowers the heating value, causes acidification, and/or lowers the dew-point.

Carbon dioxide has a kinetic diameter of about 0.29 nm and has high loading and moderate diffusivity in SAPO-34. Methane has a kinetic diameter of 0.38 nm, which is about the same size as SAPO-34 pores, so methane diffuses much slower, and loadings are less than those of $CO_2$. Because SAPO-34 membranes selectively permeate $CO_2$ in mixtures with $CH_4$, they can be used as part of a purification process to remove the $CO_2$ from raw natural gas without the need for depressurization. Recompression for feeding pipelines and liquidation can be a significant fraction of the process cost, which is minimized if the $CH_4$ is maintained at high pressure.

Adsorption using amine-based scrubbing solutions is currently used to separate $CO_2$ from $CH_4$, and although this technology is mature, it requires high capital and operating expenses and has a large footprint. Some commercial plants use polymer membranes for $CO_2$ removal, but they suffer from low permeability or selectivity, plasticization of the polymer by $CO_2$, and thermal and

chemical instability [20]. Zeolite membranes are of significant interest for replacing these technologies, but the challenges of scale-up and economic manufacture have to be solved.

## 1.4 Previous work on SAPO-34 membranes

This and the following section provide an overview of previous studies with SAPO-34 and SZZ-13 (a low-silica CHA zeolite) membranes. The historical developments such as the discovery of these zeolites as well as the first reported membranes are presented. A sample of references then highlights the progress in improving membrane performance. The most recent synthesis methods used in our lab are presented in the first part of chapter 2. Direct side-by-side comparison of both SAPO-34 and SSZ-13 membranes synthesized by different groups and their performances for the $CO_2/CH_4$ separation are emphasized in these sections.

Researchers at Union Carbide first synthesized SAPO-34 zeolite in the 1980s along with a number of other SAPO forms [21]. Other molecular sieves of aluminosilicate, aluminophosphate, and aluminosilicophosphate composition had been reported previously [22–24]. The SAPO-34 was synthesized hydrothermally at 373 - 473 K from reactive T-atom sources such as hydrated aluminum oxide, phosphoric acid, and silica sol. An organic amine is required as a structure-directing agent (templates), and tetraethylammonium was used for SAPO-34. Without the organic templates, amorphous or dense materials form instead of the microporous zeolite structure. Interestingly, the tetramethylammonium ions result in the same crystal structure in synthetic aluminophosphate (AlPO-20) and silicoaluminophosphate (SAPO-20), but tetraethylammonium ion produces different crystal structures without the presence of a silica source (AlPO-5 and AlPO-18) than when silica is present in the gel (SAPO-34). The pore size of SAPO-34 makes it of interest for gas separation and pervaporation, but much of the early research interest in SAPO-34, as with

most zeolites, focused on catalysis; SAPO-34 is still used commercially to convert methanol to olefins (MTO process).

The first SAPO-34 membrane was synthesized in 1997 by Lixiong et al. [25], who grew the zeolite film on an alumina disk support. Several growth cycles were needed to prepare a membrane with a low number of defects. Single gas permeances were reported for $H_2$, $N_2$, $CO_2$, and n-butane. The $CO_2$ permeances were between 6.4 and $8.9 \times 10^{-7}$ mol/($m^2$ s Pa) (feed pressure 220 kPa, permeate pressure 101 kPa, temperature 323 K). These researchers did not measure $CH_4$ permeances but n-butane permeance was too small to measure, which indicates a defect-free membrane layer. The n-butane permeance was likely below their detection limit as typically a sweep gas stream and a gas analyzer are required to accurately measure fluxes of slowly-permeating species such as n-butane.

Soon after, Poshusta et al. reported SAPO-34 membranes grown on the inside of α-alumina tubes [26]. Multiple growth cycles were required to achieve an impermeable layer and the membranes were calcined to remove the structure-directing template between each cycle to detect determine progress in the layer growth. The single-gas permeance decreased in the same order reported by Lixiong: $H_2 > CO_2 > N_2 > CH_4$ ($n\text{-}C_4H_{10}$ in Lixiong). The $CO_2$ permeance was $2.4 \times 10^{-8}$ mol/($m^2$ Pa s), the $CO_2/CH_4$ ideal selectivity was 19, and the $CO_2/CH_4$ separation selectivity was 30 (feed 270 kPa, permeate 132 kPa, 300 K. Poshusta et al. further improved their synthesis and later reported SAPO-34 membranes with $CO_2$ permeances that were higher than the $H_2$ permeances, likely because $CO_2$ adsorbs more strongly in the pores [27], and previous membranes had a larger fraction of defect flux. Both $H_2$ and $CO_2$ molecules are significantly smaller than the SAPO-34 pores so that the difference in steric hindrance to diffusion was less than the difference in adsorption. The $CO_2$ permeance was more than $1 \times 10^{-7}$ mol/($m^2$ Pa s), and the $CO_2/CH_4$

separation selectivity was 36 (feed 270 kPa, permeate 132 kPa, 300 K) for the best membrane. Increasing the temperature of the membrane decreased $CO_2$ permeance and decreased $CO_2/CH_4$ selectivity, likely because $CO_2$ adsorption decreased more with temperature than that of $CH_4$ as a result of the larger heat of adsorption of $CO_2$.

Li et al. grew SAPO-34 membranes on stainless steel tubular supports and measured $CO_2/CH_4$ separations at high pressures (3.1 MPa) [28]. They used three growth cycles, but placed the unseeded, Teflon-wrapped support into an autoclave tube filled with synthesis gel whereas, in previous studies, only the insides of the supports were filled with the synthesis gel. The mixture $CO_2$ permeance was $2.4 \times 10^{-7}$ mol/($m^2$ Pa s), and the $CO_2/CH_4$ separation selectivity increased to 180 (feed 3.1 MPa, permeate 100 kPa, 253 K). As the trans-membrane pressure increased for constant feed pressure, the $CO_2/CH_4$ selectivity increased and the $CO_2$ flux increased, but the permeance decreased. They calculated loading-independent, Maxwell-Stefan diffusion coefficients and used a binary Langmuir isotherm model to describe adsorption. Methane was shown to lower $CO_2$ diffusion, and $CO_2$ lowered $CH_4$ adsorption.

Carreon at al. grew SAPO-34 membranes on stainless steel supports using multiple structure-directing agents (TEAOH, dipropylamine, and cyclohexylamine) in the synthesis solution [29]. They synthesized different-sized seed crystals and were able to obtain membranes with good performance using only one growth step by tuning the chemistry of the synthesis solution. For membranes grown from supports with physically-deposited seeds, the $CO_2$ permeance was $3.8 \times 10^{-7}$ mol/($m^2$ Pa s) and the $CO_2/CH_4$ separation selectivity was 170 for the most-selective membrane (feed at 222 kPa, permeate 84 kPa, 295 K). They also covalently attached seeds to the support by functionalizing the support surface with 3-(chloropropyl)trimethoxysilane and prepared a membrane with a selectivity of 227 and similar

permeance. In a follow-up study, Carreon et al. also investigated the effect of seed crystal size on membrane performance [30]. They were able to grow 6-7.5-μm thin selective layers using small seeds on alumina supports. Their best membrane had a $CO_2/CH_4$ separation selectivity of 171, but they were able to improve the $CO_2$ permeance for mixture separations to about $2x10^{-6}$ mol/($m^2$ Pa s).

Recently, Zhou et al. further improved the synthesis of nearly defect-free, thin SAPO-34 membranes [31,32]. They determined that only one templating agent was necessary and aluminum isopropoxide could be replaced with less hazardous $Al(OH)_3$ as the alumina source for easier commercial scale-up. They also found that impermeable regions formed if the membranes were not thoroughly washed in water after the synthesis to remove gel residues from the support pores before calcination. Their membranes had good thermal stability and were resistant to degradation in water and long-term storage in air.

## 1.5 Previous work on SSZ-13 membranes

Zones first synthesized zeolite SSZ-13 at Chevron in the early 1980s [33]. He succeeded in synthesizing this high-silica CHA zeolite with a variety of organic templates such as 1-adamantamine, 3-quinuclidinol, or 2-exo-aminonorbornane or their quaternary lower alkylammonium cation derivatives. Zones also used different aluminum sources (aluminate, alumina, $AlCl_3$, or $Al_2(SO_4)_3$), several silicon sources (silicate, silica hydrogel, silicic acid, colloidal silica, orthosilicates, or silica hydroxide), and metal cation source (NaCl, or other alkali metal halides). The gel was heated in an autoclave to about 423K for several days. He also described post-synthesis treatments, such as details in the calcination procedures, ion-exchange, and steam treatment to stabilize the lattice.

The first SSZ-13 membranes were reported in 2002 by Kalipcilar et al. who grew the zeolite layer on the inside of porous stainless steel tubes [34]. The support was seeded with SSZ-13 crystals, which were synthesized as described in US patent 4544538 (1985) [35], from an aqueous mixture of amorphous silica, $Al(OH)_3$, NaOH, and N,N,N-trimethyl-1-adamantammonium hydroxide. The seeds were grown in an autoclave at 433 K for 5 days, washed with DI water, and dried at 373 K under vacuum overnight. The membranes were seeded by filling the supports with a suspension of seed crystals in water, shaken for 10 min, and then dried under vacuum. This procedure was repeated three times. The outside of the seeded supports were then wrapped with Teflon tape, and the bottoms were plugged with Teflon plugs. After the tubes were filled with synthesis gel that had the same composition as the gel used for the seed crystal synthesis, the tops of the supports were plugged with Teflon plugs. The supports were then heated for 5 days at 433 K to form one layer of SSZ-13 growth. Then, the synthesis gel was replaced and the membranes heated again to deposit another layer of SSZ-13. After 4-5 such deposition steps, the membranes were impermeable to $N_2$, indicating complete overgrowth. The membranes were then heated at 0.01 K/s to 753 K, held there for 15 h, then cooled at 0.03 K/s to remove the template.

Kalipcilar et al. reported $CO_2/CH_4$ ideal selectivities of 11 and a separation selectivity of 12 for the best membrane, and they showed that the membranes could be used for $H_2O$ removal from a $HNO_3/H_2O$ liquid mixture by pervaporation. The $CO_2$ permeance was about $1.6x10^{-7}$ mol/($m^2$ Pa s) for the most selective membrane (feed pressure 223 kPa, permeate pressure 85 kPa, 298 K). The SEM of the membrane layer cross-section showed a thickness of 10 – 40 μm, which is significantly thicker than many other small-pore zeolite membranes and explains the lower permeance. Carbon dioxide permeated faster than $H_2$ even though $CO_2$ is larger because it adsorbs

more strongly, and $CH_4$ permeated faster than $N_2$ for the same reason. The larger i-butane permeated faster than n-butane so both of those molecules permeate through non-zeolite pores.

More recently, Kosinov et al. synthesized SSZ-13 membranes on α-alumina hollow fiber supports [36]. They measured a $CO_2$ permeance of $3.0 \times 10^{-7}$ mol/($m^2$ Pa s) and a $CO_2/CH_4$ separation selectivity of 42 (feed pressure 0.5 MPa, 293 K). They suggested that the high silica content of their membranes (Si/Al ≈ 100) resulted in fewer defects, and made the membranes quite stable to humidity. In a different study, Kosinov et al. investigated the influence of support morphology on the quality of SSZ-13 or ZSM-5 selective layers [37]. The zeolites were again synthesized hydrothermally, but two types of α-alumina hollow fiber supports with different surface roughness were used. Membranes prepared on the rougher, more-irregular supports were more stable during calcination, which is necessary to remove the template, whereas membranes grown on smooth supports tended to form cracks under similar conditions due to thermal stress in the film. They suggested using low-temperature ozone treatment to remove the template from the membranes that were prone to cracking instead of heating to 720 K or higher in air.

Zheng et al. also prepared high-silica SSZ-13 membranes on tubular mullite supports to investigate their stability in humid environments [38]. Their membrane synthesis required only one hydrothermal growth cycle that used two structure-directing agents, N,N,N,trimethyl-1-adamantammonium hydroxide and tetraethylammonium hydroxide. Their best membrane had a $CO_2$ permeance of $2.0 \times 10^{-7}$ mol/($m^2$ Pa s) and $CO_2/CH_4$ selectivity of 300 (0.2 MPa feed, 303 K).

Kosinov et al. also prepared SSZ-13 membranes with Si/Al ratios between 5 and 100 on α-alumina supports to determine changes in the membrane properties [39]. Changes in hydrophobicity improved the performance of the low-silica (hydrophilic) membranes for $H_2O$/EtOH pervaporation because the $H_2O$ loading increased more than the EtOH loading. The

high-silica (hydrophobic) membranes were better for $CO_2/CH_4$ separations with $CO_2$ permeances of $3x10^{-7}$ mol/($m^2$ Pa s) and $CO_2/CH_4$ selectivities around 40 (0.6 MPa feed, 293 K), mostly because the less polar membranes had fewer defects.

## 1.6 Effects of contaminants/impurities on zeolite membrane performance

Commercial purification processes typically require separating more than two components because product streams from chemical reactors are often complex mixtures, and reaction precursors and naturally occurring raw materials (i.e., natural gas) can contain a variety of impurities or undesired compounds. These minor components or impurities likely affect the separation performance, especially for zeolite membrane separators. Depending on their chemical nature, the trace contaminants can impede the flow of other gases through the internal pores by strongly adsorbing and blocking diffusion through channels inside the pore network. They can also competitively adsorb on internal surface sites and decrease loading and thus fluxes of the desired molecules, or they can inhibit access to the external membrane surface by blocking surface sites and thus access to the internal pore network.

The aim of this thesis is to further understand the effects of impurities on the performance of molecular sieve membranes so that process designs can include appropriate measures to remove these impurities or select membrane types that are the least susceptible to specific impurities. Changes in performance in the presence of minor components are in most cases not easy to predict, and experimental comparison between binary and multi-component feeds are required as a first step to determine possible mechanisms and remedies.

To date, few studies have focused on the effects of minor contaminants on separations with zeolite membranes. In many cases, impurities at sufficiently low concentrations may not interfere with separations, but most studies report lowered permeances in the presence of contaminants.

Interestingly, some studies report enhanced separation selectivities in the presence of impurities/contaminates. Kosinov et al. tested their high-silica SSZ-13 membranes to determine water stability and found that 2.2 kPa of $H_2O$ in the 600-kPa feed lowered the $CO_2$ permeance by 75%, but it increased $CO_2/CH_4$ selectivity by about 13% because water preferentially adsorbed in the more-hydrophilic, non-zeolite defect pores and blocked them [36]. Poshusta et al. studied the effect of humidity on gas permeation through SAPO-34 membranes [40] and found that membranes with $CO_2/CH_4$ selectivities >20 were stable, but water degraded the other membranes over months of exposure to the lab atmosphere and increased defect pore concentration, and the degradation appeared to accelerate with time. They found that 0.6 – 0.9 mol% $H_2O$ in the feed completely blocked the SAPO-34 pores so that flow through the membranes was primarily through defects. Li et al. measured the effects of $H_2O$, $N_2$, ethene, propane, and n-butane on $CO_2/CH_4$ separations in SAPO-34 membranes [41]. Water at 170 ppm in a 187-kPa feed decreased $CO_2$ permeance by about 15% over 12 days, and the $CO_2/CH_4$ selectivity decreased by about 8%. Adding 3% $N_2$ to the feed did not affect the separation significantly. A feed with 1% $C_2$ – $C_4$ hydrocarbons decreased the permeance and selectivity, and n-butane had the largest effect; 1% n-butane decreased $CO_2$ permeance by 59% and $CO_2/CH_4$ separation selectivity by 42% because it competitively adsorbed and reduced $CO_2$ loading more than $CH_4$ loading. The initial permeances and selectivities were restored by removing the impurity from the feed.

Wu et al. measured the effect of propane on $CO_2/CH_4$ separations in SAPO-34 and SSZ-13 membranes [42], and found that at 270 kPa, propane decreased $CO_2$ permeances and $CO_2/CH_4$ selectivities in both types of CHA membranes. At 1.73-MPa feed pressure, propane also decreased $CO_2$ permeances and $CO_2/CH_4$ selectivities in SAPO-34 membranes, but it *increased* $CO_2$ permeance and $CO_2/CH_4$ selectivity in SSZ-13 membranes. The interesting increase in $CO_2$

permeance could be attributed to deformation of the 8-member ring pore windows as propane adsorbed into the zeolite.

## 1.7 External surface structures of zeolite crystals and how they affect transport

Most transport models developed for membranes formed from microporous materials such as zeolites assume that the first step in the transport process is adsorption from the bulk fluid to the external surface (or directly from the fluid phase into the outer pore areas) [43,44]. The adsorbed species then move from their adsorption sites on the external surface to the pore openings, followed by diffusion through the bulk of the porous solid to the permeate side according to the gradient in chemical potential. The bulk diffusivity can also vary with concentration. The diffusing species then leave the internal pores to adsorb on the external area on the permeate side, followed by desorption from the permeate surface into another bulk phase. Each step in this transport process can have a different resistance to the overall movement of the permeating species [45–47]. The resistances assigned to adsorption and desorption was estimated to only be significant compared to the internal diffusion resistance for membranes thinner than 100 nm [46]. Because the membranes used in this thesis were all thicker than 3 μm, surface resistances due to adsorption/desorption process were assumed to be insignificant. However, diffusion barriers from layers on the membrane surface with different transport properties from the bulk material may alter selectivity, and thus the resistance of such layers was considered. Several studies suspected that zeolite crystals in some cases may be covered with layers of non-zeolitic material with different crystal structures and porosities than the bulk zeolite, and these regions could slow diffusion.

Diffusion barriers on the surface of zeolite crystals were reported in the literature by Karger and coworkers in the early 1980s when they used NMR to show that external diffusion resistances in NaCaA and ZSM-5 zeolites may form during zeolite manufacture or they could be introduced

by different pretreatment steps. Methane diffusion in ZSM-5 was reduced due to coking between crystals in a polycrystalline sample after catalytic cracking of n-hexane [48]. They also showed that Xe (0.4 nm) diffusion into NaX (0.57-nm pores) did not have a significant surface barrier, but Xe diffusion into NaCaA and ZSM-5 was slowed by surface resistances [49], and $CH_4$ (0.38 nm) diffusion was not hindered in any of the three zeolites. Thus, surface resistances may vary with the size of the probe molecule so that small molecules may not be affected but larger molecules could be hindered significantly.

Wloch showed that surface layers on ZSM-5 crystals hindered hexane uptake, but they could be removed by etching with HF so that after etching the rate of n-hexane diffusion into the zeolite increased by two orders of magnitude [50]. He postulated that the surface of the zeolite crystals had mechanical barriers of unordered crystal that probably formed during synthesis from a saturated reaction mixture. Similarly, Kortunov et al. used interference microscopy to measure adsorption and desorption of isobutane in ZSM-5 [51] with as-synthesized and etched crystals, and found surface regions that had different diffusivities than the bulk material. Defects in the form of cracks increased diffusion into the ZSM-5 crystals because the cracks allowed for better access to the interior of the crystals but defects in the crystal structure near the surface could block and significantly decrease diffusivities. This diffusion resistance disappeared after the crystals were etched in HF solution. They also discussed that the surface resistance increased with an increasing number of adsorption and desorption cycles, likely because immobilized adsorbate molecules (including impurities) accumulated on strong adsorption sites at the surface layer of the crystals. Teixeir et al. grew silicalite-1 crystals in different sizes from 80 nm to 3 μm and used zero length chromatography to measure cyclohexane transport [52]. They measured the same diffusion activation energy in all crystal sizes, but the apparent diffusivity of cyclohexane was lower for the

smaller crystals. Their results suggested that rate-limiting transport in the small crystals was likely due to either narrowing of surface pores or extended diffusion length near the surface because of blocked external pores.

Subtle changes in the surface chemistry may also affect uptake rates as shown by Kalantzopoulos et al., who measured $H_2$ diffusion in as-synthesized and silane-treated silicalite-1 and found that $H_2$ diffusion of the untreated sample was slower [53]. They attributed the lower $H_2$ diffusivity in the as-synthesized sample to hydrophilic surface silanol groups that bind $H_2O$, which increased the energy barriers for surface diffusion into the pores or physically restricted access to the pores. The silane treatment decreased the hydrophilicity and thus decreased the water loading on the surface. Computer simulations with both hard-sphere ballistic collision models (no surface adsorption [43]) and molecular dynamics simulations (diffusion into pores was from adsorbed species [44]) also showed that small changes in the pore size can change diffusivities by orders of magnitude if the sizes of the diffusing molecules are close to size of the pore openings.

Similarly, macroscopic methods to measure diffusivity in zeolites (including zero length chromatography, gravimetric, frequency response, and interference microscopy) tend to yield lower diffusivities than microscopic techniques (quasielastic neutron scattering and pulsed field gradient-NMR), and the measured diffusivities can vary by as much as 3 orders of magnitude [52]. Surface barriers that decrease diffusivities for uptake-based measurements would not affect intercrystalline diffusion and could thus qualitatively explain these discrepancies.

The presence of such non-zeolite barriers, which are not well understood, might also affect the behavior of the zeolite membranes studied in this thesis. For example, the pore size of SAPO-34 (0.38 nm) is larger than the kinetic diameter of propane (0.43 nm), but the smallest cross-section of a propane molecule is smaller than its kinetic diameter so that it can pass through the narrow

but short pore windows. If the surface structure effectively reduces the pore windows at the zeolite/non-zeolite interface to less than 0.38 nm, or if the aspect ratio (ratio of pore diameter to pore length) changes, propane may not be able to diffuse into the bulk zeolite structure (Figure 1.4).

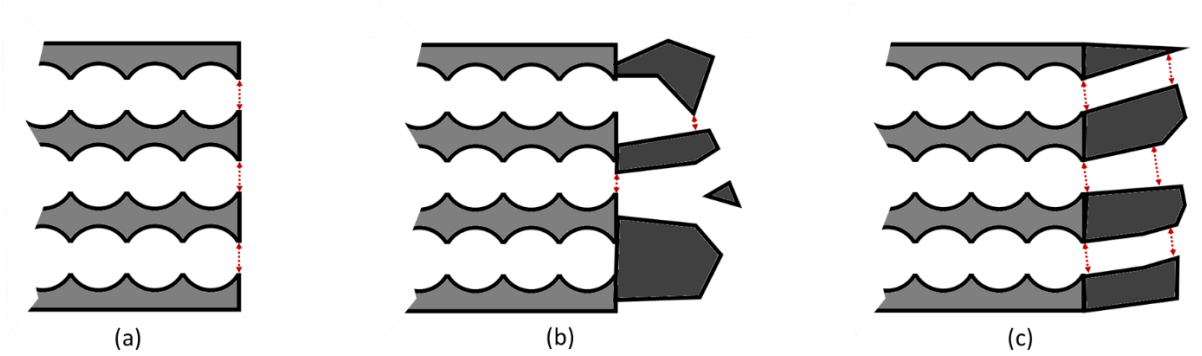


**Figure 1.4.** Schematic of CHA zeolite pores with a window-cage structure and external surface on the right with (a) regularly terminated zeolite unit cell, (b) external non-zeolite layer with reduced pore diameter for diffusion into the zeolite, and (c) external non-zeolite layer channels of similar pore size different geometry that prevent bent molecules like propane from entering the zeolite.

Thus, even though the selectivity of zeolite membranes is assumed to be the result of uniform pore sizes in the bulk crystals, diffusion through thin surface layers with different porosities that may form during operation or storage could irreversibly alter permeances and selectivities and thus affect reproducibility. These surface layers may be amorphous material that forms during synthesis when the hydrothermal growth in solution terminates [48]. Alternatively, coke deposits could form during removal of the structure-directing agent. They could also form from impurities that deposited on the zeolite surface during permeation measurements or storage and decomposed during subsequent storage or regeneration at high temperature. If the external surface of a zeolite does not have the same uniform pore structure as the bulk crystal, then the molecular sieving properties of the zeolite could be different.

# Chapter 2 Experimental Methods

## 2.1 Zeolite membrane synthesis

Zeolite membranes are typically synthesized as thin polycrystalline layers grown on porous inorganic supports under hydrothermal conditions (from aqueous solutions at elevated temperature and pressure). Most synthesis procedures require seeding of the support, and thus, zeolite crystals have to be synthesized as well. The crystal synthesis is often carried out under similar conditions, and with similar gel compositions, to those used for the membranes. After the growth of the zeolite layers, calcination in air or vacuum at temperatures exceeding 673 K may be necessary if organic templates are used for the synthesis, since these templates remain embedded in the zeolite pores and block access to the pore network. Thorough rinsing of the membranes with water before the calcination may also be necessary to remove residual synthesis gel from the support pores because impermeable regions can form on the zeolite/support interface as these residues are heated [31]. The susceptibility of many zeolites to adsorption of water and other small molecules suggests that they should be stored in a contamination-free environment or at elevated temperatures to minimize adsorption. Water has been shown to affect the zeolite backbone for some types of zeolites and thus can slowly degrade membranes over long time-periods.

### 2.1.1 Synthesis solutions

The first step in zeolite synthesis is the preparation of aqueous solutions (synthesis gels) that contain all the precursors required to form the zeolite framework. Recipes for a wide variety

of different zeolite framework types have been published over the last half-century, and these recipes included the concentrations and types of precursors, mixing conditions, aging times and other subtle details that often strongly affect the product properties [22,54]. Many sources of alumina, silica, and phosphorous (or other T-atoms) may be used. Often, the synthesis gels contain organic structure-directing agents (templates) that are necessary to form the correct pore structure as the framework components surround and incorporate the template molecules into zeolite lattice during the crystal growth. Only dense, often amorphous products are obtained for these recipes if the template is omitted. Small differences in the template structure, e.g., a methyl- instead of an ethyl-group, may result in completely different zeolite frameworks [21]. Since the template molecules occupy space in the zeolite crystals, but are not chemically bound to the framework, they can be removed, for example, by calcination in air at elevated temperate, to open the zeolite pores networks. Some synthesis procedures improve when more than one type of template molecule is used in the gel [38]. Changes in concentration of Al, Si, and P precursors also affect the zeolite structures, even when the same template is used [21]. The ratio of T-atoms in the solution is typically reflected in the chemical composition of the zeolite crystals, but in some cases, T-atoms are not incorporated completely and the gel composition may differ from that of the final product. Similar synthesis solutions are used for making both seed crystals and membranes.

The experimental sections of chapters 3 – 5 provide details of the specific chemistries and synthesis procedures used for preparing the membranes studied in this thesis. Two types of zeolite membranes were investigated, SSZ-13 and SAPO-34, and both have the same crystal structure (Chabazite – CHA with 0.38 nm pores) but different chemical compositions.

### 2.1.2 Membrane supports

Thin (few-μm thick) zeolite membranes are brittle and fragile, thus the selective layer must be grown on a macroporous substrate which provides structural support, especially for applications with a significant pressure drop across the membrane. The support has to be chemically and mechanically stable to resist both the synthesis conditions and, if necessary, the calcination procedures to remove templates. Typically, these supports are formed from porous stainless steel or mesoporous ceramic materials such as alumina, mullite, or silica. Early work was carried out on flat support discs, but tubular or even monolithic geometries are preferred for commercial applications to obtain larger surface-to-volume ratios for compact module geometries and for easier sealing. The support diffusion resistance should be low compared the zeolite layer to avoid interference with the separation process. Several studies addressed the effect of support interference and found that both selectivities and fluxes can be negatively affected if the support is not optimized. In the case of thin, high-flux membranes, a gutter layer can improve membrane performance [55], but the membranes used in this work were sufficiently thick that the supports did not limit fluxes.

If tubular geometries are used for the supports, the separation layer can be formed on either the inside or outside of the tubes. Layers grown on the inside of tubes are better protected from damage during handling and sealing may be easier, but the surface area is larger for layers on the outside. Since the cost of inorganic supports is often high and may to a large extent determine the overall membrane cost, higher surfaces areas for a given tube length are preferred.

Some details in the zeolite growth process could also dictate the best support geometries and morphologies. For example, SAPO-34 zeolites grow well on the inside of porous alumina tubes with a smooth internal surface (100-nm pores) because the zeolite layer attaches well to the

surface and is dimensionally stable during calcination. SSZ-13, in contrast, does not form dense layers on the inside of smooth tubes because it uses a larger template molecule than SAPO-34 and crystals shrink significantly when the template is removed, causing cracks to form. Thus, SSZ-13 membranes can only be grown on the outside of tubes with large pores where the zeolite film is incorporated into the support structure and thus better protected from shrinkage and cracking. However, zeolite layers intergrown with the support are in thicker, and fluxes of these SSZ-13 membranes are much lower than those of the SAPO-34 membranes grown on the inside of smooth supports [37].

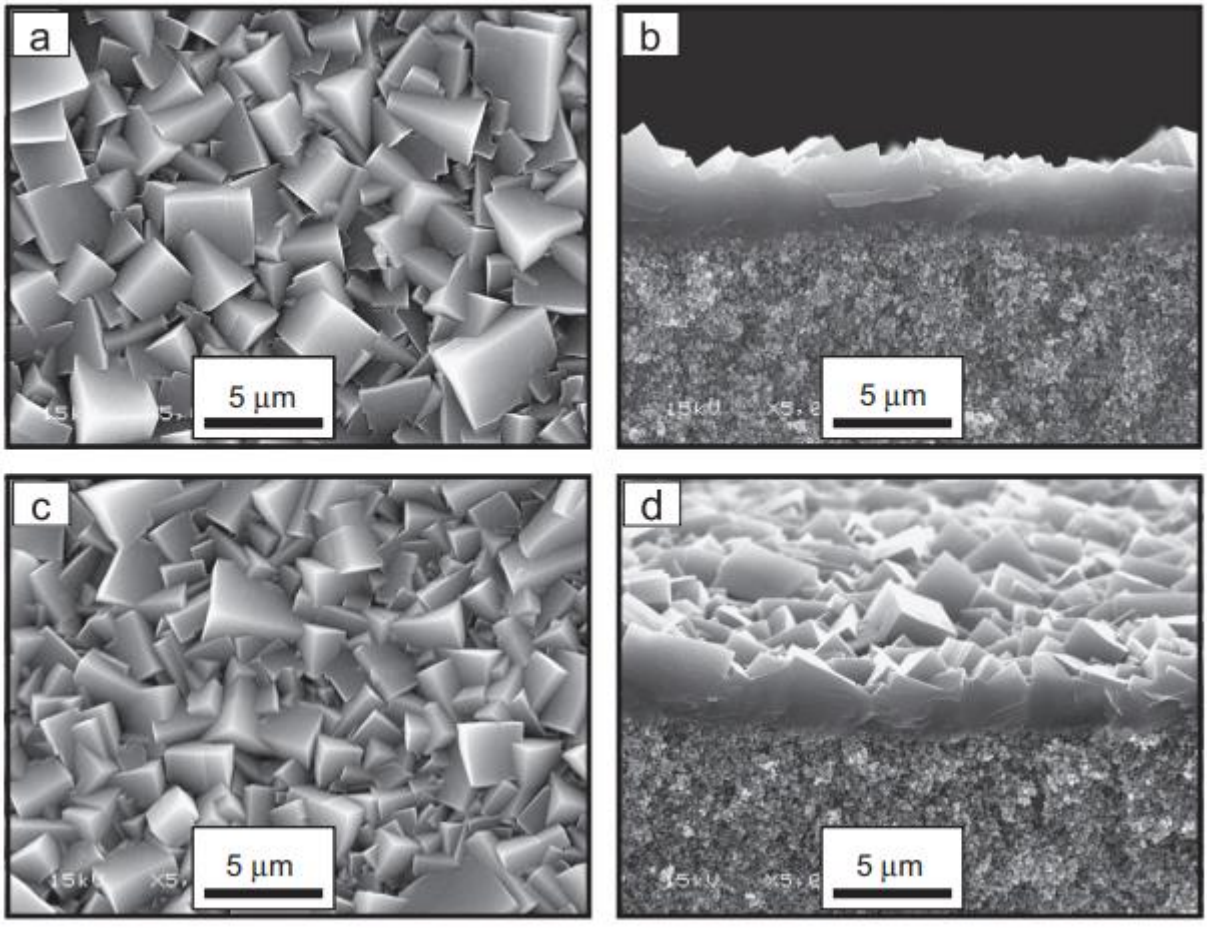


**Figure 2.1.** Surface and cross-sectional SEM images of SAPO-34 membranes. TEAOH/$P_2O_5$ ratio of 1.75 in a and b, ratio of 2.0 in c and d. Reproduced from Zhou et al. [31].

Figure 2.1 shows the surface of a SAPO-34 membrane grown on the inside of a porous alumina tube (100-nm pores). The selective layer is formed from inter-grown cubic crystals. Even though the layers appear dense in the SEM images, nm-sized gaps can exist between the crystals where intergrowth is not complete, or cracks formed during calcination as a result of thermal mismatch; both types of defects can limit the selectivity. The first SAPO-34 and SSZ-13 membranes reported in the literature required 3 to 6 growth cycles before an impermeable layer (before calcination) was obtained. The presence of the template in the pores of SAPO-34 and SSZ-13 prevents gas permeation, and thus any flux observed before calcination is due to incomplete coverage of the surface. The first-generation membranes were typically 10 – 40 μm thick and had low fluxes. However, state-of-the-art membranes such as the ones shown in Figure 2.1 (~ 3 μm thick) can be grown in one synthesis step with fluxes more than one order of magnitude higher than the earlier membranes as a result of thinner separation layers. Small, intercrystalline gaps or cracks formed during calcination may still affect membrane performance, and membrane-to-membrane variations could be the result of such defects. However, the best membranes to-date have shown selectivities for $CO_2$ (0.33-nm kinetic diameter) over i-butane (0.49-nm kinetic diameter, which is too large for the 0.38-nm zeolite pores) exceeding 500,000 and thus could be considered practically defect-free. Other subtleties of the synthesis procedures for SAPO-34 membranes include the need to thoroughly rinse the membrane after hydrothermal growth to remove all residual gel from the support before calcination, and calcining in vacuum instead of air. Residual gel in the support structure has been shown to cause impermeable regions after calcination [31], and fluxes are typically higher after calcination in vacuum because oxygen causes some coking in the pores.

Several studies showed that membrane defects can also be blocked post-synthesis by intentional coking, treatment with reactive molecules such as silanes, or by introducing large molecules that preferentially adsorb in crystal gaps [48], but most post-synthesis modifications decrease permeances and are often not permanent.

## 2.2 Gas permeation measurements

All permeation experiments were carried out in several custom-build flow systems. Figure 2.2 shows the schematics of such setup, and Figure 1.3a shows how the membrane was sealed in the module. Gases are fed with computerized (LabVIEW) flow controllers from pressurized cylinders, and toluene was stored in in-line bubblers (not shown). The pressure to the flow controllers was regulated with standard regulators and the system pressures were controlled with manual back-pressure regulators downstream on the retentate side of the membrane module and on the permeate side. Pressures were recorded with electronic pressure transducers. Gas mixtures were obtained either by feeding separate streams from different flow controllers and allowing mixing of the gases in the lines prior to entering the membrane module, or by using pre-mixed gas cylinders when the vapor pressure of one of the components (propane or butane) was too low to directly feed into the system at high pressures. The permeate and retentate compositions were analyzed with a gas chromatograph (GC), and the volumetric flow rates of the retentate and permeate were measured with soap-film flow meters because mixed gas flow rates cannot be measured accurately with electronic flow meters as their response changes with gas composition.

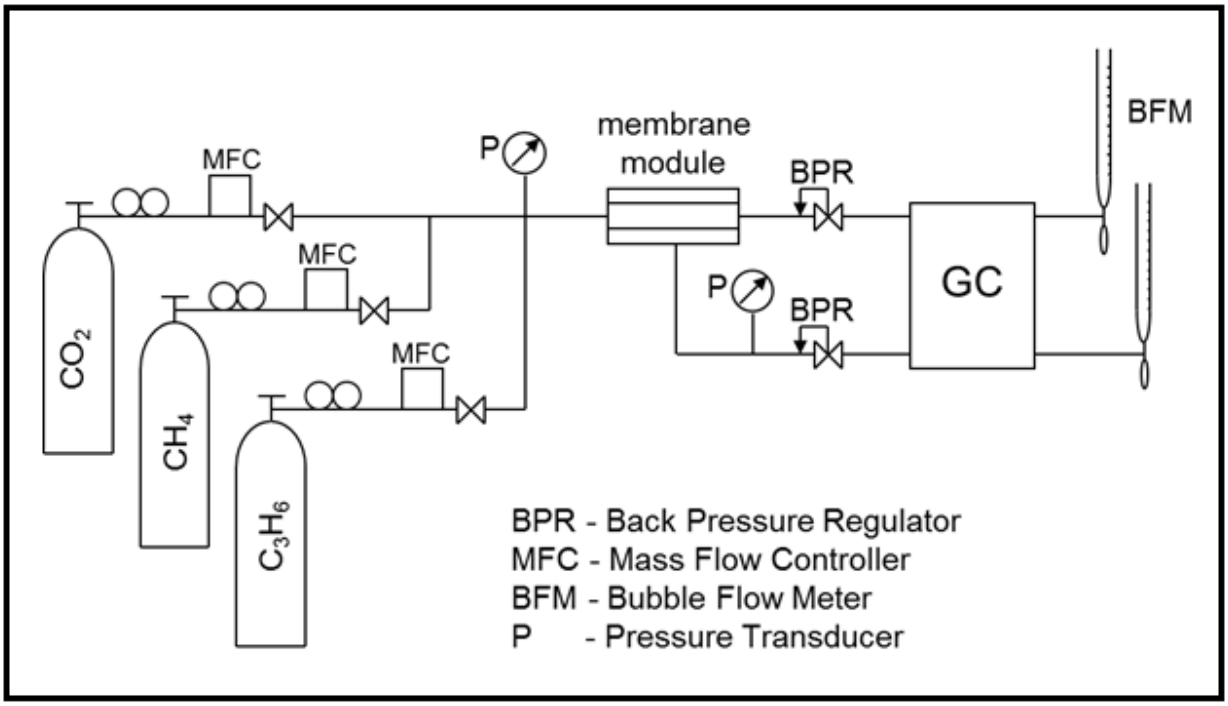


**Figure 2.2.** A multicomponent gas flow system for membrane testing.

Permeances and selectivities were calculated from the measured permeate and retentate composition and flow rates. A log-mean pressure difference (equation 11) was used as a driving force for permeation since the feed composition changes along the membrane axis as it is depleted of the faster permeating species. The flux through the membrane was calculated from a mass balance over the membrane module using the feed, retentate, and permeate compositions and flow rates. The area of the membrane was calculated from the support geometry and permeances and selectivities were then calculated using equations 10, and 12.

# Chapter 3 Increasing $H_2/N_2$ Separation Selectivity in CHA Zeolite Membranes by Adding a Third Gas

This chapter has been published in the Journal of Membrane Science as: N.O. Chisholm, G.C. Anderson, J.F. McNally, H.H. Funke, R.D. Noble, J.L. Falconer, Increasing $H_2/N_2$ separation selectivity in CHA zeolite membranes by adding a third gas, J. Memb. Sci. 496 (2015) 118–124.

## 3.1 Abstract

Adding propane or n-butane in low concentrations to a $H_2/N_2$ feed increases the $H_2/N_2$ separation selectivity in SAPO-34 membranes by decreasing the $N_2$ permeance more than the $H_2$ permeance. More than two days were required to reach steady state because propane and n-butane diffuse slowly into the zeolite pores, but they adsorb strongly and thus decrease $H_2$ and $N_2$ loadings. Although the loading of the more-weakly adsorbed $H_2$ is expected to decrease more, the $N_2$ permeance decreased more than the $H_2$ permeance apparently because the diffusivity of the larger $N_2$ molecule decreased more. Propane more than doubled the $H_2/N_2$ selectivity at 298 K, but its effect on selectivity decreased as the temperature increased because the propane loading in the SAPO-34 pores decreased. Ethane also decreased $H_2$ and $N_2$ permeances, but it did not change $H_2/N_2$ selectivity. As with propane, ethane decreased $H_2$ loadings more than $N_2$ loadings, and decreased $N_2$ diffusivity more than $H_2$ diffusivity. However, the smaller ethane had less effect on the $N_2$ diffusivity than did propane, so the net effect was that the selectivity did not change. The

effects of alkane adsorption in SAPO-34 membranes were reversed when the alkanes were removed from the feed.

## 3.2 Introduction

Zeolite membranes can separate molecules with high fluxes and selectivities based on differences in molecular size and adsorption properties. Diffusivities in zeolites decrease significantly as the kinetic diameters of molecules approach the diameter of the zeolite pores [1,2]. Thus, SAPO-34 membranes, which have 0.38-nm pores, are highly selective for separating binary $CO_2/CH_4$ mixtures, even at high pressures [3,4], because the kinetic diameter of $CH_4$ is approximately 0.38 nm, whereas the $CO_2$ kinetic diameter is 0.33 nm. Most mixtures contain more than two types of molecules, however, and even components in low concentrations can be detrimental to the separations of the main components in the mixture. The $CO_2/CH_4$ separation is of interest for natural gas purification because some natural gas fields have high $CO_2$ concentrations. Natural gas also contains higher hydrocarbons in low concentrations [5,6], and the presence of propane slowly decreased permeances and $CO_2/CH_4$ separation selectivities of SAPO-34 membranes at both low and high pressures, so that steady state was not obtained even after several days [7,8]. Similarly, at low pressures, propane decreased both permeances and $CO_2/CH_4$ selectivities of SSZ-13 membranes, which have the same CHA structure as SAPO-34 membranes but do not contain phosphorus. In contrast, at high pressures (1.73 MPa), 5% propane *increased* the $CO_2/CH_4$ selectivity by 30% and also increased the $CO_2$ permeance by 20% [8]. The kinetic diameter of propane (0.43 nm) is larger than the pore size of SAPO-34 and SSZ-13 zeolites, so that it might be expected to not adsorb in these zeolites. Kinetic diameter, however, is not a sufficient measure of molecular sieving, and propane adsorbs in CHA zeolite pores to relatively high loadings, although it diffuses much slower than $CO_2$ or $CH_4$ [8,9].

Few studies have measured permeation of ternary mixtures of light gases through zeolite membranes. Nicolas et al. [10] reported that fluxes decreased by 75% and $CO_2/N_2$ separation selectivities increased from 3 to 6 in a MFI membrane (0.55-nm pore size) when propane was added to the feed. Although they did not explain the selectivity increase, it may have been caused by swelling of the MFI crystals. Swelling of MFI crystals has been reported to decrease defect size and thus decrease fluxes through defects when linear hydrocarbons adsorb in MFI zeolites [11]. Increased $CO_2/N_2$ selectivity would result if a large fraction of the original $CO_2$ and $N_2$ fluxes was through non-selective defects. In another study of ternary mixtures, Himeno et al. [12] found that adding 1% propane to a $CO_2/CH_4$ mixture only slightly decreased $CO_2$ permeance through DDR membranes, and the $CO_2/CH_4$ selectivity did not change much. Since propane is too large to fit into DDR pores (0.36 nm x 0.44 nm) [13], however, any change in permeances may be due to adsorption on the external surfaces of the zeolite crystals. Baertsch et al. [14] studied permeation of ternary mixtures of aromatic hydrocarbons through MFI membranes, and all hydrocarbons slowed to the rate of the slowest species, apparently because the MFI channels are sufficiently narrow that the aromatics cannot pass each other.

In the current study, the effects of low concentrations of ethane, propane, and n-butane on $H_2/N_2$ separation through a SAPO-34 membrane were measured. The kinetic diameters of both $N_2$ (0.36 nm) and $H_2$ (0.29 nm) are smaller than SAPO-34 pores. The $H_2/N_2$ separation selectivities of 3.3 - 9.9 for SAPO-34 and other CHA membranes [15–18] are too low to be of commercial interest since other membrane types have higher selectivities, but this mixture serves as a model system to determine how adsorption of a larger molecule affects permeation of small molecules of different sizes and with different adsorption properties.

In the current study, when propane was added to an equimolar $H_2/N_2$ feed at low pressures, both $H_2$ and $N_2$ permeances decreased but the $H_2/N_2$ separation selectivity more than doubled because the $N_2$ permeance decreased more than that of $H_2$. The alkane permeances were low compared to $H_2$ and $N_2$ permeances because the alkanes diffuse slowly through SAPO-34 pores, and alkane permeances were primarily due to diffusion through defects. Results are presented here for one SAPO-34 membrane, but similar behavior was observed for a second membrane.

## 3.3 Experimental Methods

### 3.3.1 Preparation and characterization of SAPO-34 membranes

SAPO-34 membranes were hydrothermally synthesized after seeding the support with SAPO-34 crystals, as previously reported [4]. To synthesize the seed crystals, $Al(O\text{-}i\text{-}Pr)_3$, tetraethyl ammonium hydroxide (TEAOH), and deionized water were stirred for 2 h, then Ludox AS-40 colloidal silica was added, and the solution was stirred an additional 2 h. Finally, $H_3PO_4$ was added and the solution was stirred for 3 d. All chemicals were from Sigma-Aldrich. The resulting gel had molar ratios of 1.0 $Al_2O_3$: 2.0 $P_2O_5$: 0.6 $SiO_2$: 4.0 TEAOH: 75 $H_2O$. The gel was heated to 462 K in a microwave oven and held at that temperature for 7 h. The resulting SAPO-34 crystals were separated from the gel by centrifugation, and then cleaned by resuspension in deionized water and centrifugation.

The membranes were synthesized on the inner surface of 6-cm long, tubular alumina supports (Inopor, Germany, 100-nm pore size). Before membrane synthesis, nonporous layers were formed on the ends of the supports so the membranes could be sealed for separation measurements. This was done by glazing the ends of the tubes with Duncan ceramic glaze at 1225 K and then washing the glazed supports in boiling water four times. Next, Teflon tape was wrapped around the outside of the support, and SAPO-34 seeds were rubbed into the inner side of the

support with pipe cleaners. The membrane synthesis gel, which had a molar ratio of 0.85 $Al_2O_3$: 1.0 $P_2O_5$: 0.3 $SiO_2$: 2.0 TEAOH: 155 $H_2O$, was prepared by mixing water, $H_3PO_4$, and $Al(OH)_3$, stirring for 2 h at room temperature, then adding Ludox AS-40 colloidal silica. It was then stirred for 30 min before adding TEAOH. The gel was heated to 323 K and stirred overnight. The seeded supports were placed into a stainless steel autoclave, the synthesis gel was slowly added, and then the sealed autoclave was heated to 483 K for 6 h in a forced convection oven. After synthesis the Teflon tape was removed, the membranes were washed in flowing water for 15 min, and then soaked in a beaker of water for 48 h to remove unreacted gel. The TEAOH template was removed by heating the membranes under vacuum at 673 K for 4 h with heating and cooling rates of 1 K/min.

Adsorption isotherms of crystals collected from the bottom of the autoclaves after membrane synthesis were measured with a Quantachrome AS1-C volumetric adsorption system. The SAPO-34 crystal structure was confirmed by XRD with a Scintag PAD-V powder diffractometer, and the crystal morphology was determined by SEM (JEOL JSM-5910LV).

### 3.3.2 Gas permeation measurements

Single-component and mixed-gas permeations were measured in a flow system equipped with computer-controlled mass flow controllers. The membranes were sealed in stainless steel modules with Viton o-rings. No sweep gas was used. Teflon inserts were used to increase gas velocity at the membrane surface so as to minimize concentration polarization [19]. Retentate and permeate flow rates were measured with bubble flow meters. The compositions of the retentate and permeate were determined by an HP 5890 GC equipped with a TCD, a FID, and a HayeSep D column.

All separations measurements used an equimolar $H_2/N_2$ mixture, and up to 5% ethane, 10% propane, and 10% n-butane concentrations were used in the feed. Unless otherwise noted, the feed flow rate was 700 sccm, the feed pressure was 350 kPa, and the permeate pressure was 85 kPa. The membranes were heated with electric heat tapes, and a PID controller maintained the temperature constant at 298, 348, or 398 K.

## 3.4 Results and Discussion

### 3.4.1 Characterization of SAPO-34 crystals

Analysis by XRD indicated that the crystals formed during membrane synthesis had the SAPO-34 structure and no other structures were detected. Their BET surface area was 576 +/- 29 $m^2/g$, which is similar to values reported previously for SAPO-34 (483 – 677 $m^2/g$) [20,21]. The crystals had a cubic shape in SEM images, with sizes from ~0.4 - 3 μm. Cross section and surface SEM images of a membrane prepared using the same procedures were presented previously [4], and they showed 1-3 μm cubic crystals and a 3-μm thick SAPO-34 layer.

Adsorption isotherms at 293 K for $H_2$, $N_2$, $CH_4$, ethane, propane, and n-butane (Figure 3.1) show that $H_2$ and $H_2$ adsorb weakly compared to the alkanes. The $N_2$ loading is about twice the $H_2$ loading, and at 80 kPa the alkane loadings are about ten times the $N_2$ loading. The $H_2$ and $N_2$ isotherms are linear up to 80 kPa, but the ethane and propane isotherms approach saturation loadings. The n-butane isotherm is also not linear, but its loading continues to increase at higher pressures, possibly due to multilayer adsorption or capillary condensation between crystals since the measurements were closer to the saturation pressure of n-butane (~250 kPa). Because propane and n-butane diffuse slowly in SAPO-34 pores, these isotherms were measured over more than 24 h. The loadings only increased slightly for longer adsorption times, suggesting that the isotherms were close to equilibrium. In contrast, equilibration times for $N_2$, $H_2$, and ethane adsorption were

short because these molecules are smaller than the SAPO-34 pores and thus diffuse much faster than propane or n-butane.

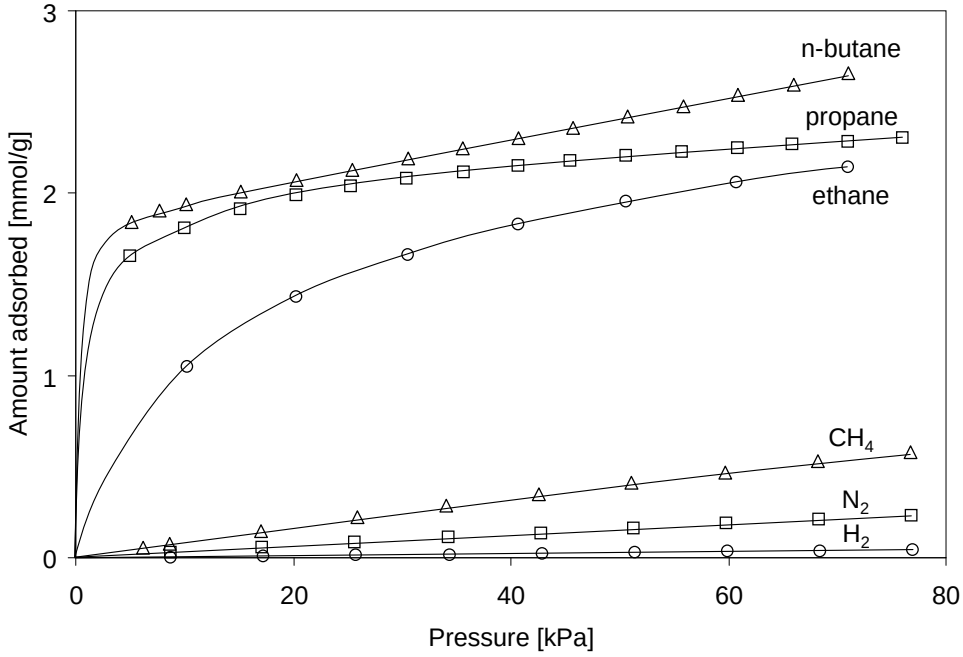


**Figure 3.1.** Adsorption isotherms for $H_2$, $N_2$, $CH_4$, ethane, propane, and n-butane in SAPO-34 crystals at 293 K.

### 3.4.2 Membrane characterization

The SAPO-34 membrane had a low defect permeance since its $CO_2$/i-butane separation selectivity was 310, with an i-butane permeance of $3.5 \times 10^{-9}$ mol/($m^2$ s Pa) for a 4.5% i-butane/95.5% $CO_2$ feed at a pressure of 265 kPa. The single-gas permeances at room temperature were $4.0 \times 10^{-7}$ mol/($m^2$ s Pa) for $N_2$ and $1.7 \times 10^{-6}$ mol/($m^2$ s Pa) for $H_2$. Even though higher $CO_2$/i-butane selectivities were reported previously for similar SAPO-34 membranes [8], the defect permeances for $N_2$ and $H_2$ are estimated to be less than 2% of the overall $N_2$ and $H_2$ permeances assuming Knudsen diffusion, and thus permeation through defects should not affect the separation selectivity significantly. The $CO_2/CH_4$ separation selectivity was 90 with a $CO_2$ permeance of

$3.2x10^{-6}$ mol/($m^2$ s Pa) at 350-kPa feed pressure, and the selectivity decreased as the feed pressure increased, as shown in Figure 3.2. Similar selectivity behavior has been reported previously for SAPO-34 membranes prepared using the same procedure [4].

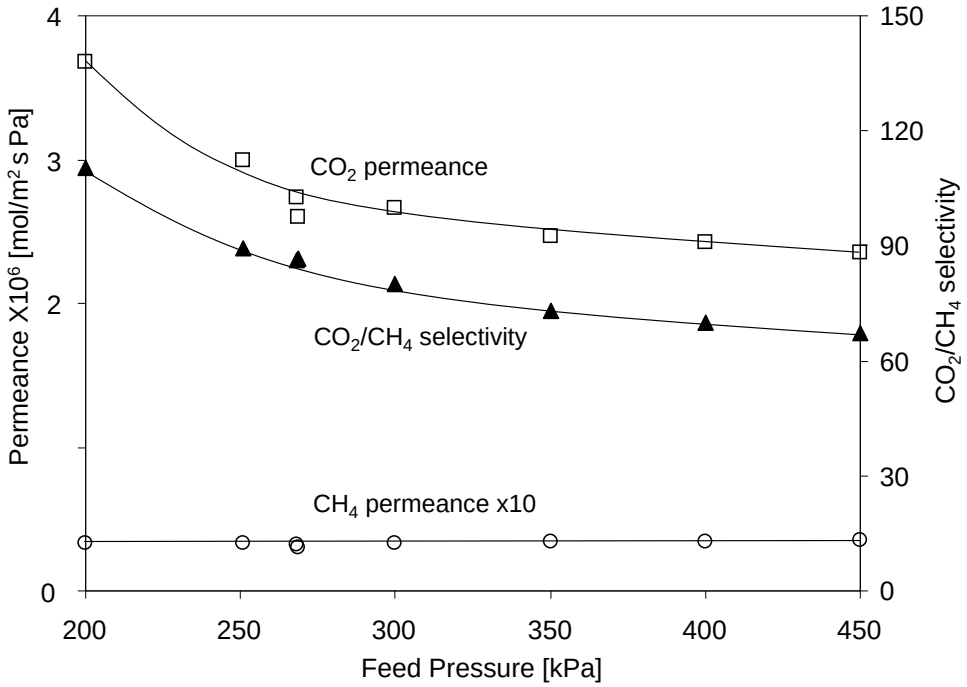


**Figure 3.2.** Carbon dioxide and $CH_4$ permeances and $CO_2/CH_4$ separation selectivity for the SAPO-34 membrane at 293 K as a function of feed pressure.

As shown in Figure 3.3, the $H_2$ and $N_2$ single-gas permeances decreased as the temperature increased, and the $H_2/N_2$ ideal selectivity (ratio of permeances) increased because the loading of the more strongly-adsorbed $N_2$ decreased more than the $H_2$ loading, so that the $N_2$ permeance decreased more than the $H_2$ permeance. The increase in ideal selectivity with increasing temperature is similar to previous observations with SAPO-34 membranes that had lower fluxes but similar $H_2/N_2$ ideal selectivities [15].

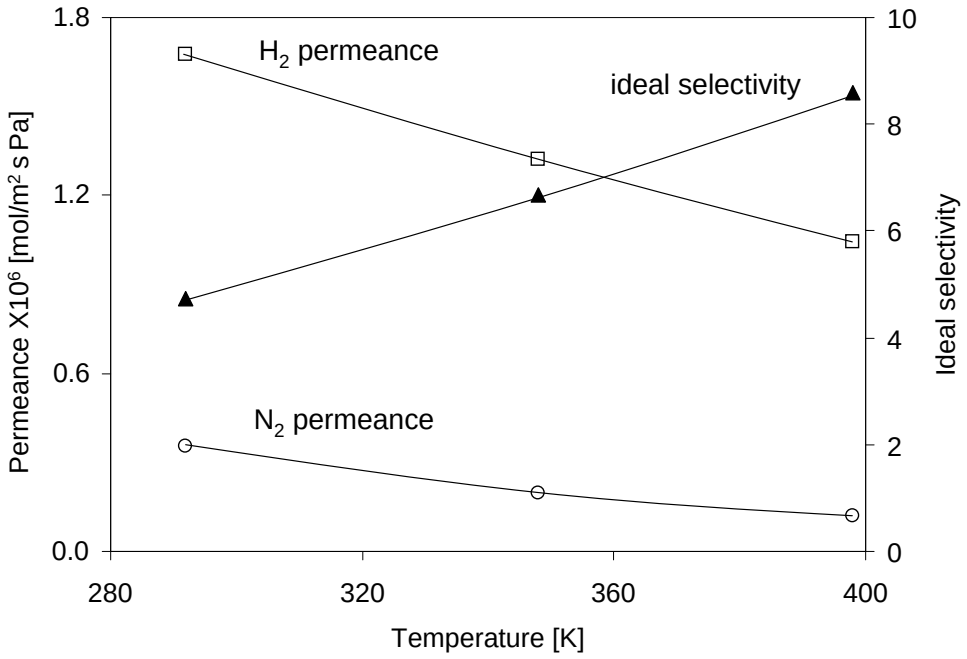


**Figure 3.3.** Single-gas $H_2$ and $N_2$ permeances and $H_2/N_2$ ideal selectivity for the SAPO-34 membrane as a function of temperature.

### 3.4.3 Effect of propane on $H_2$ and $N_2$ permeances

The $H_2/N_2$ separation selectivity for the SAPO-34 membrane for a 50/50 $H_2/N_2$ feed was approximately 4 at ambient temperature. The $H_2$ mixture permeance was about 10% lower than its single-gas permeance at the same total pressure because competitive adsorption of $N_2$ decreased $H_2$ loadings. Nitrogen has a higher heat of adsorption (14 kJ/mol [22]) than $H_2$ (6 kJ/mol [23]) and higher loadings than $H_2$ at room temperature (Figure 3.1). The $N_2$ mixture permeance was similar to its single-gas value because $H_2$ did not significantly affect the loading of the more strongly-adsorbed $N_2$. When 5% propane was added to the feed, both $H_2$ and $N_2$ permeances decreased, as shown in Figure 3.4, but the $N_2$ permeance decreased faster, so the $H_2/N_2$ selectivity increased from 3.9 to 8.3 over 5 h. The initial drop in the $H_2$ and $N_2$ permeances may be due to propane adsorption into the pores on the external surface of the SAPO-34 crystals. The permeances continued to decrease as more propane adsorbed into the SAPO-34 pores [24], and the selectivity

increased over two days. Similar behavior was observed for other SAPO-34 membranes synthesized using the same procedures.

The propane permeance reached steady state almost immediately, indicating that most of the propane diffuses through defects [8]. The low propane permeance (~1% of the $N_2$ permeance) indicates that only a small fraction of the $N_2$ and $H_2$ permeates through defects. The defect permeance was calculated for propane by assuming Knudsen diffusing and using the i-butane permeance of $3.5 \times 10^{-9}$ mol/(m$^2$ s Pa). The calculate propane permeance is about 40% higher than the measured propane permeance ($2.6 \times 10^{-9}$ mol/(m$^2$ s Pa), suggesting that i-butane adsorbs more strongly in the defects and thus a larger fraction of its permeance may be due to surface diffusion compared to the more weakly-adsorbed propane. The propane permeance through the SAPO-34 pores was much smaller than through defects, and thus any increase in permeance through SAPO-34 pores over time could not be detected.

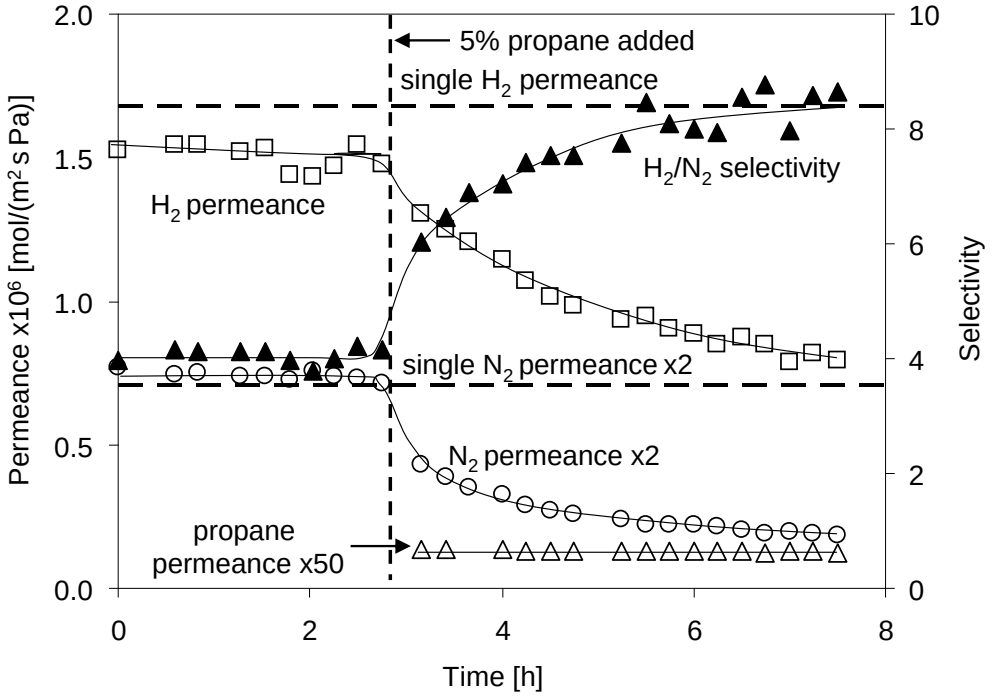


**Figure 3.4.** Hydrogen, $N_2$, and propane mixture permeances and $H_2/N_2$ separation selectivity at 293 K for the SAPO-34 membrane before and after 5% propane was added to the feed.

The $H_2$ and $N_2$ permeances decreased more for higher propane concentrations (Figures 3.5 and 3.6) because the propane loading was higher in the SAPO-34 pores. The $N_2$ permeance decreased faster than the $H_2$ permeance when the propane concentration increased, so the $H_2/N_2$ selectivity increased more at higher propane concentrations for the first 4 h of exposure to propane (Figure 3.7), although the selectivity change was not large when the propane concentration increased from 2.5 to 5%. Moreover, when steady-state was reached after 2 days, the $H_2/N_2$ selectivity was 9.8 with 10% propane in the feed; this is only 9% higher than when 2.5% propane was in the feed (Figure 3.8). Increasing the propane feed concentration from 2.5 to 10% only changed the propane loading by about 17% because the slope of the isotherm is small at the corresponding partial pressures, as shown in Figure 3.1 (9 kPa at 2.5% propane and 35 kPa at 10% propane). Thus, the similar increases in $H_2/N_2$ selectivity at 2.5 and 10% propane is likely due to similar propane loadings.

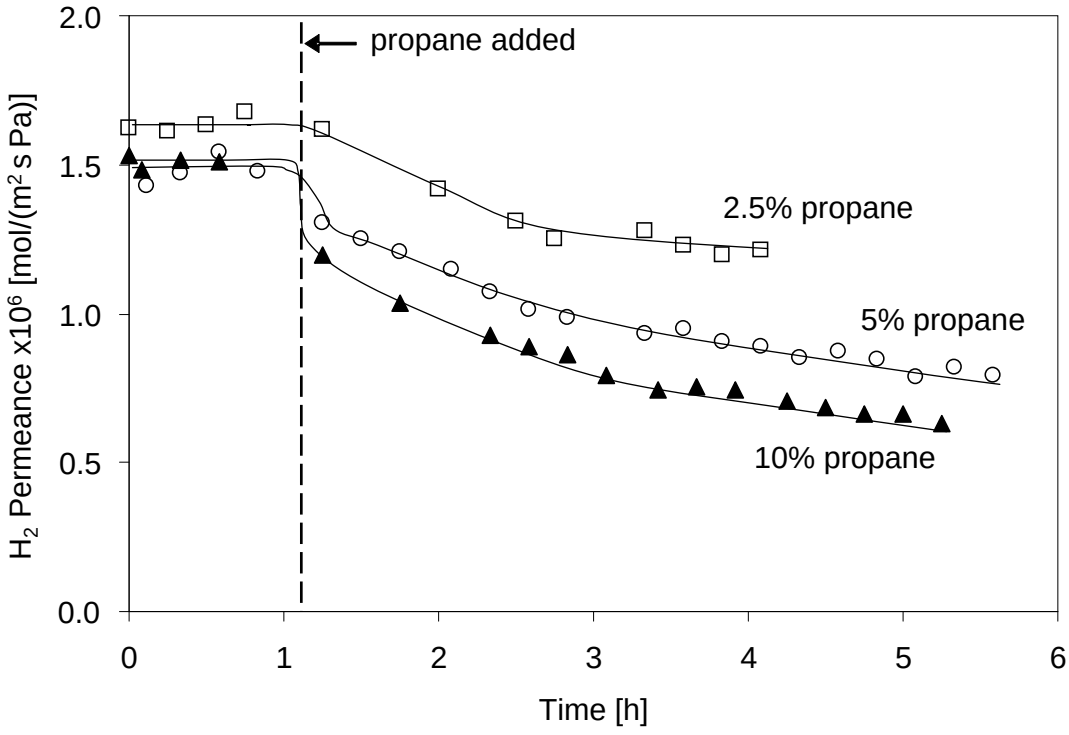


**Figure 3.5.** Hydrogen permeances at 293 K for a $H_2/N_2$ feed to the SAPO-34 membrane before and after propane was added to the feed at three propane concentrations.

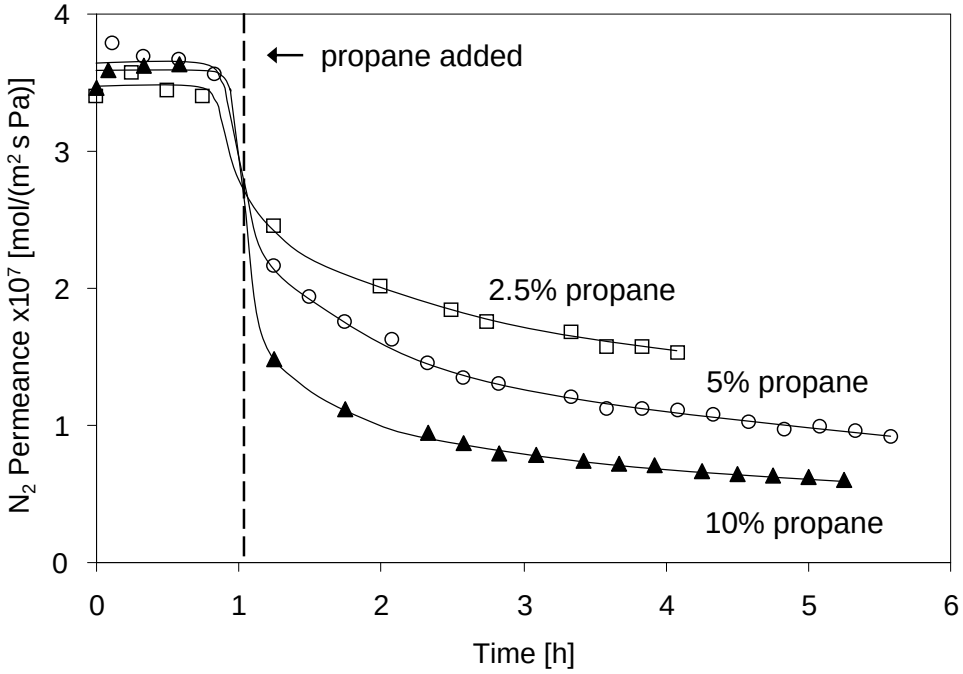


**Figure 3.6.** Nitrogen permeances at 293 K for a $H_2/N_2$ feed to the SAPO-34 membrane before and after propane was added to the feed at three propane concentrations.

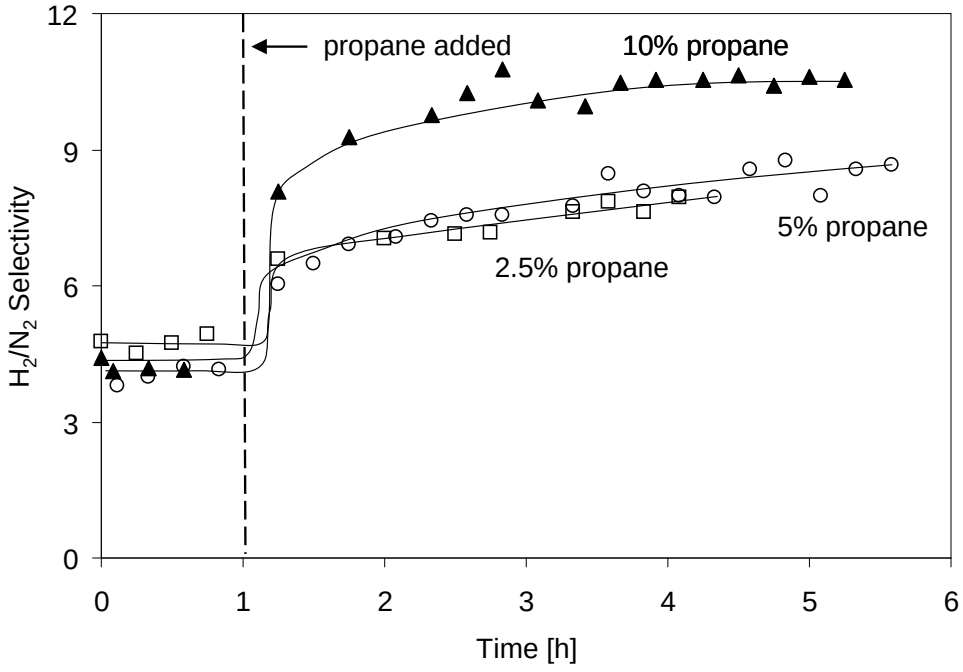


**Figure 3.7.** $H_2/N_2$ separation selectivity at 293 K for the SAPO-34 membrane before and after propane was added to the feed at three propane concentrations.

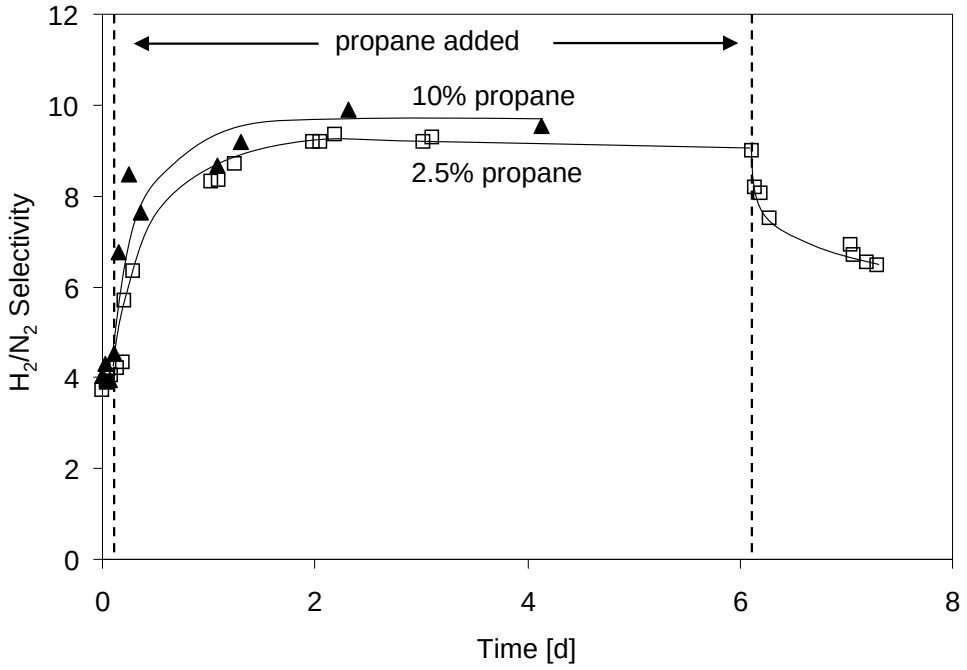


**Figure 3.8.** $H_2/N_2$ separation selectivity at 293 K for the SAPO-34 membrane in the presence of 2.5% and 10% propane for a feed flow rate of 400 sccm. Propane was removed from the feed for 2.5% propane after about 6 d.

After steady-state selectivities were obtained, propane was removed from the feed, and, as shown in Figure 3.8, the $H_2/N_2$ selectivity decreased by about 20% over a few hours. However, even after 1.5 days the selectivity was still higher than the initial selectivity. The propane remaining in the SAPO-34 pores was removed by heating the membrane to 398 K for one hour while maintaining the $H_2/N_2$ feed, and then the initial selectivity was recovered.

When the temperature increased, the $H_2$ permeance (Figure 3.9) decreased much less than the $N_2$ permeance (3.10) so that the $H_2/N_2$ selectivity increased significantly (Figure 3.11). The $H_2/N_2$ ideal selectivity (Figure 3.3) also increased with temperature. The heat of adsorption of $N_2$ is higher than that for $H_2$, so $N_2$ loadings decreased more as the temperature increased, and this caused the selectivity increased.

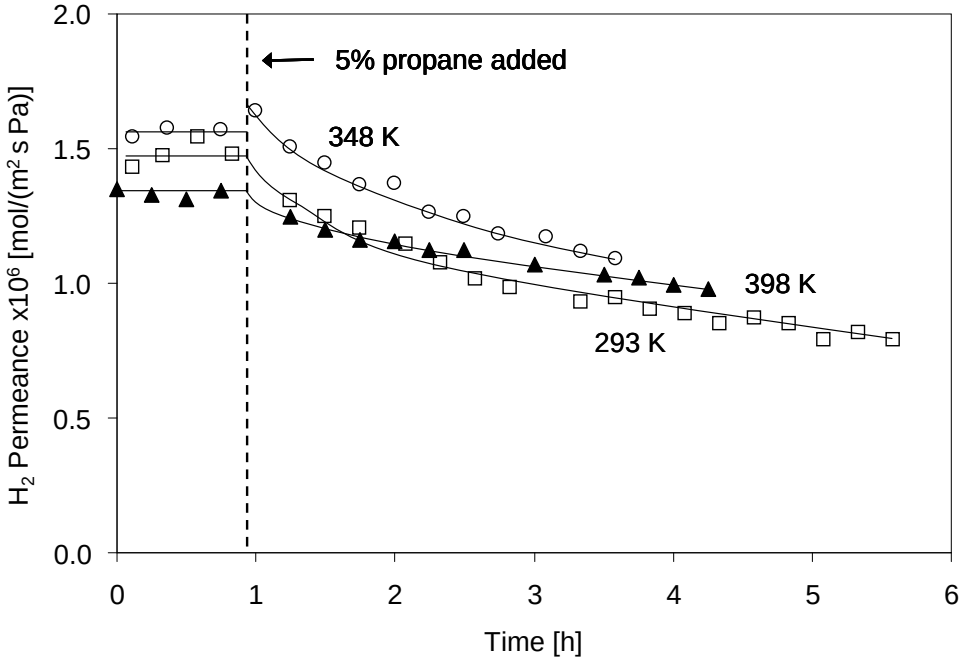


**Figure 3.9.** Hydrogen permeances for a $H_2/N_2$ feed to the SAPO-34 membrane at three temperatures before and after 5% propane was added to the feed.

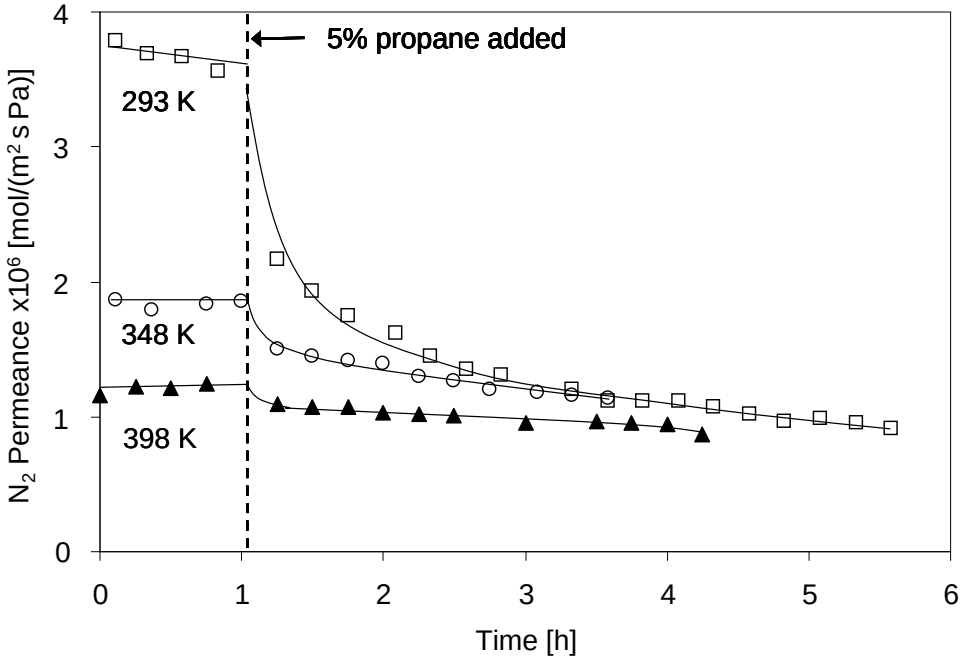


**Figure 3.10.** Nitrogen permeances for a $H_2/N_2$ feed to the SAPO-34 membrane at three temperatures before and after 5% propane was added to the feed.

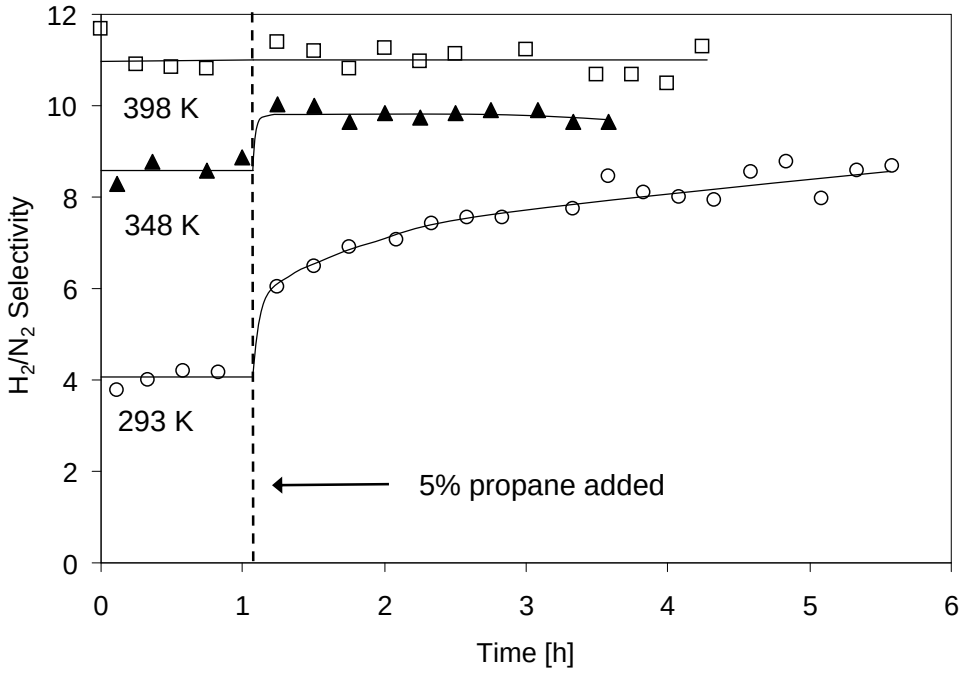


**Figure 3.11.** $H_2/N_2$ separation selectivity for the SAPO-34 membrane before and after 5% propane was added to the feed at three temperatures.

At all temperatures, the permeances decreased when propane was added to the feed, but, as shown in Figure 3.10, the largest decrease for the $N_2$ permeance was at the lowest temperature (293 K), resulting in the largest increase in $H_2/N_2$ selectivity. At 395 K, propane had almost no effect on the selectivity (3.11) because its loading was low in the SAPO-34 pores at 395 K. The propane loading at 395 K was estimated to be less than 20% of its room temperature loading, based on an extrapolation from the temperature dependence of adsorption isotherms [9,22].

Note that even though the selectivities stabilized after 1 h at 348 and 398 K, the $H_2$ and $N_2$ permeances continued to decrease slowly with time. In contrast, the propane permeances did not change with time at the three temperatures used because most of the propane permeated through defects and thus quickly reached steady state. The propane permeance decreased from ~$2.8 \times 10^{-9}$ mol/($m^2$ s Pa) to $1.9 \times 10^{-9}$ mol/($m^2$ s Pa) as the temperature increased from 293 to 398 K. Both

surface diffusion and Knudsen diffusion fluxes decrease as temperature increases, and both mechanisms may contribute to diffusion through the membrane defects.

Slower-diffusing molecules can slow faster-diffusing molecules by occupying adsorption sites in straight-channel zeolites such as MFI. Diffusional coupling is not as pronounced for CHA zeolites, at least for small molecules, which can pass each other in the cages [25]. Krishna et al. [26] found, using molecular dynamics, that the $H_2$ transport coefficient through SAPO-34 pores was not affected significantly by $CH_4$, but they did not look at larger molecules. Because $H_2$ has a lower heat of adsorption (6 kJ/mol) than $N_2$ (14 kJ/mol), propane (31 kJ/mol [22]) should decrease the $H_2$ loading more than the $N_2$ loading in the SAPO-34 pores. Since propane decreases the $N_2$ permeance more than the $H_2$ permeance, and since permeance is a product of loading and diffusivity, propane must decrease the $N_2$ diffusivity more than the $H_2$ diffusivity. The $H_2$/propane selectivity at 398 K was ~660 when 5% propane was added to a $H_2/N_2$ feed. The selectivity decreased to ~500 after 3 h as $H_2$ fluxes decreased but the propane permeance remained constant.

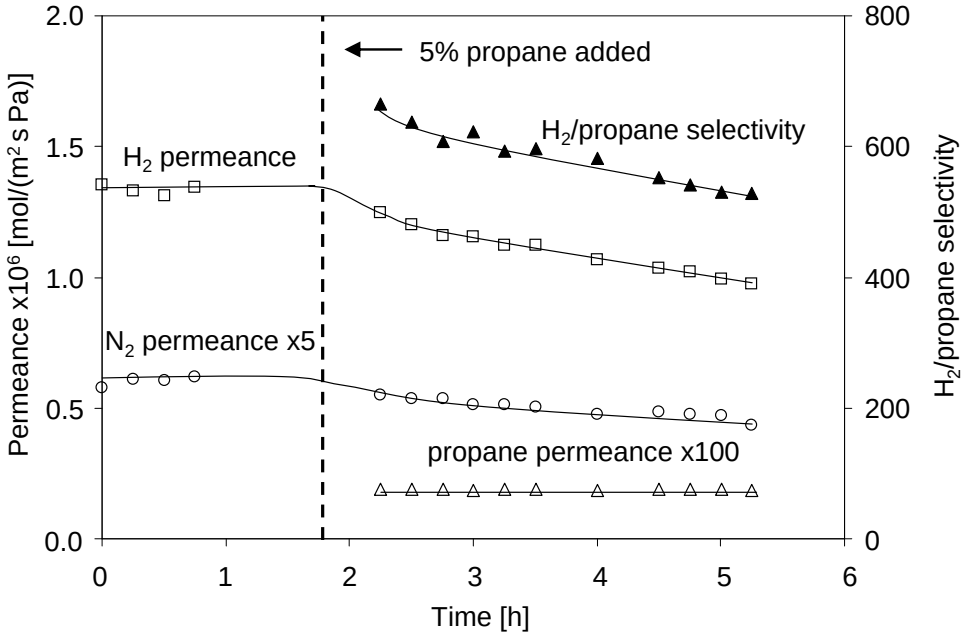


**Figure 3.12.** Hydrogen and $N_2$ permeances before, and $H_2$, $N_2$, and propane permeances and $H_2$/propane separation selectivity after 5% propane was added to the feed for the SAPO-34 membrane at 398 K.

### 3.4.4 The effects of n-butane and ethane

n-Butane, like propane, decreased the $N_2$ permeance more than the $H_2$ permeance (Figures 3.13 and 3.14), but the $H_2/N_2$ selectivity increased less than with propane (Figure 3.15). The $H_2$ and $N_2$ permeances decreased more at higher n-butane concentration, but the selectivity increase was essentially the same for 5 and 10% n-butane. The n-butane permeances of approximately $7 \times 10^{-9}$ mol/(m$^2$ s Pa) were relatively independent of the n-butane concentration and equilibrated quickly, similar to the propane permeances, because n-butane also permeated mostly through defects. The n-butane permeance ($8 \times 10^{-9}$ mol/(m$^2$ s Pa) is about 3 times the propane permeance and 1.8 times the i-butane permeance, suggesting a larger contribution of surface diffusion since the linear n-butane, which has more contact with the surface, likely adsorbs more strongly on the defect walls than either propane and i-butane. The n-butane isotherm (3.1) shows that the n-butane equilibrium

loading in the zeolite pores only increases by about 12% as the n-butane pressure increases from 10 to 18 kPa; these partial pressures correspond to 5 and 10% feed concentrations during the permeation measurements.

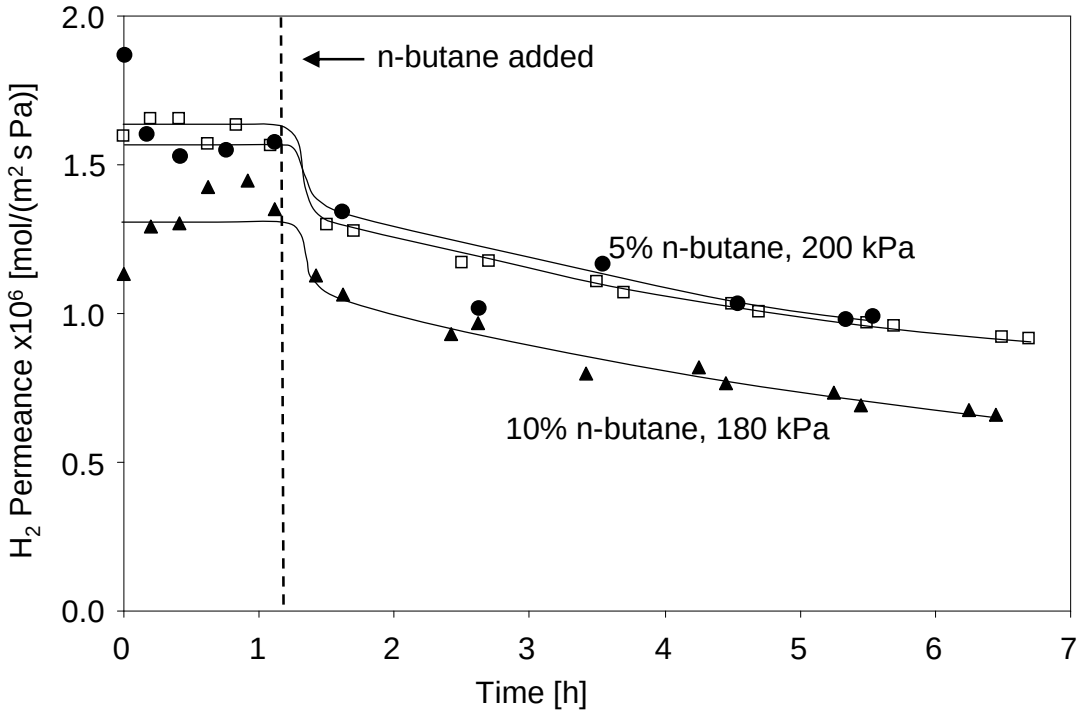


**Figure 3.13.** Hydrogen permeances at 293 K for a $H_2/N_2$ feed to the SAPO-34 membrane before and after 5% (repeat measurements) and 10% n-butane were added to the feed. The total feed pressure is indicated.

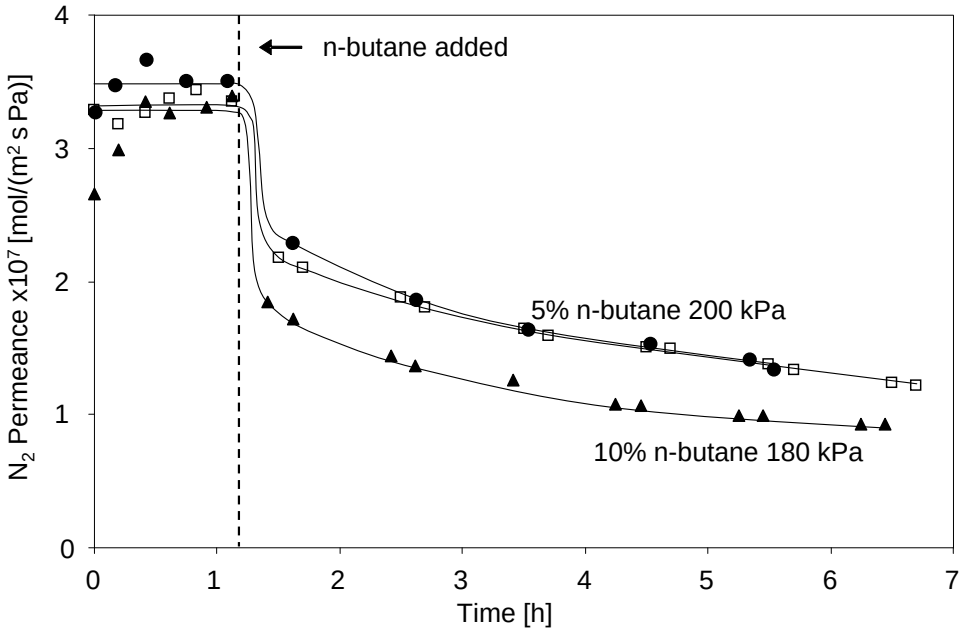


**Figure 3.14.** Nitrogen permeances at 293 K for a $H_2/N_2$ feed to the SAPO-34 membrane before and after 5% and 10% n-butane were added to the feed.

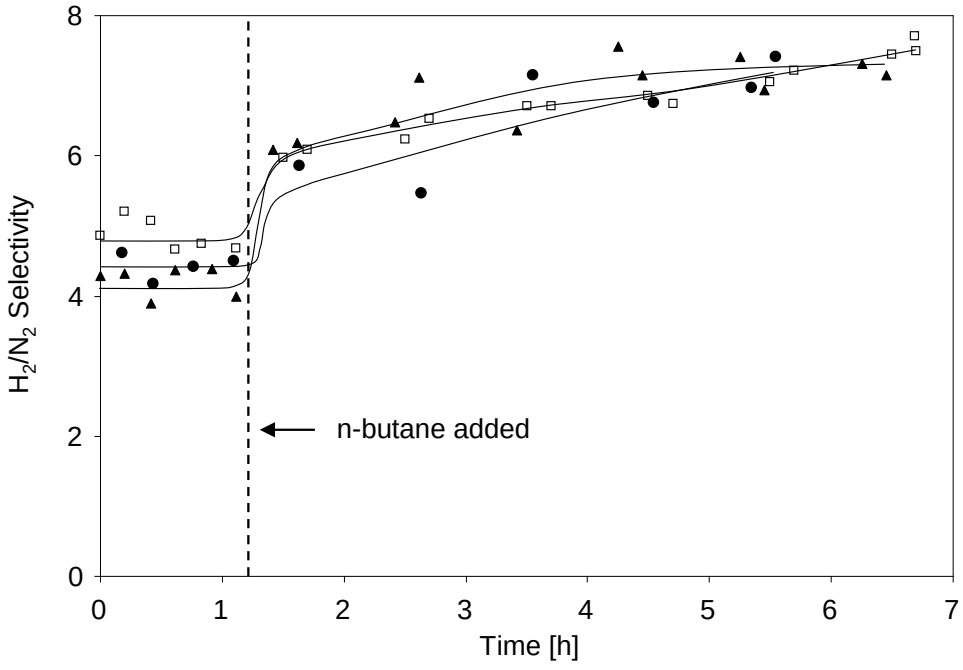


**Figure 3.15.** $H_2/N_2$ separation selectivity at 293 K for the SAPO-34 membrane before and after 5% (●,□ at 200 kPa) and 10% (▲ at 180 kPa) n-butane were added to the feed.

Adding ethane to the $H_2/N_2$ feed decreased both $H_2$ and $N_2$ permeances by about 50%. However, in contrast to the behavior observed with propane and n-butane, the $H_2$ and $N_2$ permeances reached steady state within 30 min, and the $H_2/N_2$ selectivity did not increase. Ethane has a smaller kinetic diameter than either propane or n-butane, and thus diffuses into the SAPO-34 pores faster and reaches its equilibrium loading sooner. Because ethane (heat of adsorption of 21 kJ/mol [22]) adsorbs more weakly in SAPO-34 pores than propane (31 kJ/mol), it decreases the $H_2$ and $N_2$ loadings less, but it should decrease the $H_2$ loading more than the $N_2$ loading. However, because $N_2$ is larger than $H_2$, ethane should decrease the $N_2$ diffusivity more than the $H_2$ diffusivity, and apparently these two effects are about equal so that the permeances decrease, but the $H_2/H_2$ selectivity does not change in the presence of ethane.

### 3.4.5 Effect of propane on $N_2/CH_4$ selectivity

In contrast to the $H_2/N_2$ selectivity, propane decreased the $N_2/CH_4$ selectivity (3.16) by decreasing the $N_2$ permeance more than the $CH_4$ permeance. The change in $N_2$ permeance with time was similar to that observed for $H_2/N_2$ mixtures; the permeance initially dropped and then continued to decrease more slowly. The heat of adsorption is only slightly larger for $CH_4$ (16.3 kJ/mol [22]) than $N_2$ (14 kJ/mol), so propane might preferentially decrease the $N_2$ loading. As $N_2$ and $CH_4$ permeances through SAPO-34 pores decreased, a larger fraction of the $CH_4$ permeance was due to diffusion through defects, and this may also be partially responsible for the selectivity decrease. If the i-butane permeance of $4 \times 10^{-9}$ mol/($m^2$ s Pa) is used to estimate $CH_4$ permeance through defects, assuming Knudsen diffusion, then 15% of the $CH_4$ permeance could be due to diffusion through defects. This may overestimate the $CH_4$ defect permeance since some of the i-butane permeance is likely due to surface diffusion.

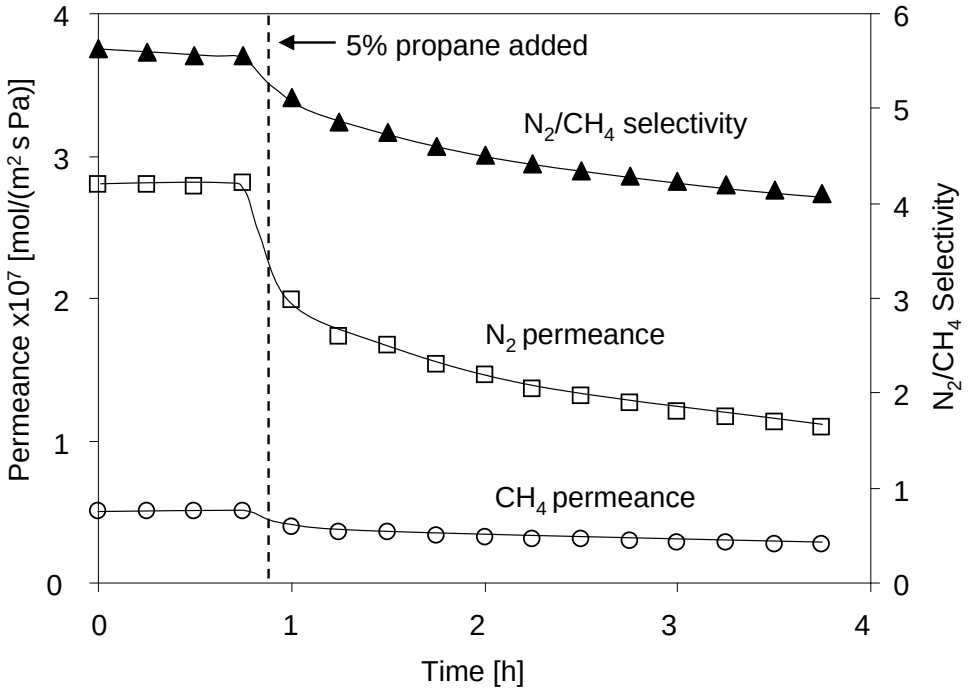


**Figure 3.16.** $N_2$ and $CH_4$ permeances and $N_2/CH_4$ separation selectivity at 293 K for the SAPO-34 membrane before and after 5% propane was added to the feed.

## 3.5 Conclusions

The $N_2/H_2$ separation selectivity in SAPO-34 membranes more than doubled in the presence of propane and n-butane because the $N_2$ permeance decreased more than the $H_2$ permeance. Because $H_2$ adsorbs more weakly than $N_2$, competitive adsorption of propane should decrease the $H_2$ loading more. Thus, the $N_2/H_2$ selectivity likely increased because propane inhibited diffusion of $N_2$ more than the smaller $H_2$. When propane or n-butane was in the feed, steady state was only reached after two days at 293 K because these alkanes slowly diffuse into SAPO-34 pores. At higher temperature (348 K, 398 K), steady state was reached quickly after propane was added to the feed, but propane had less effect on $H_2/N_2$ selectivity because the propane loading was lower. Ethane also decreased $N_2$ and $H_2$ permeances, and steady state was reached within 30 min at 293 K, but the $H_2/N_2$ selectivity did not increase. Apparently the lower $H_2$ loading

(relative to the $N_2$ loading) was compensated by the lower $N_2$ diffusivity so the net effect was no change in selectivity. The effects of the adsorbed alkanes were reversible, but significant time was required to remove the alkanes from SAPO-34 pores at room temperature. Propane decreased the $N_2/CH_4$ separation selectivity.

## 3.6 Acknowledgements

We gratefully acknowledge support from the National Science Foundation, Grant CBET 1263130 and G.C.A. We gratefully acknowledge support by the Academy of Applied Sciences.

## 3.7 References

[1] D.W. Breck, Zeolite molecular sieves : structure, chemistry, and use, 1974, pp. 633–641.

[2] J. Karger, D.M. Ruthven, Diffusion in Zeolites and Other Microporous Solids, John Wiley, New York, NY, 1992.

[3] E.W. Ping, R. Zhou, H.H. Funke, J.L. Falconer, R.D. Noble, Seeded-gel synthesis of SAPO-34 single channel and monolith membranes, for $CO_2/CH_4$ separations, J. Membr. Sci. 415-416 (2012) 770–775.

[4] R. Zhou, E.W. Ping, H.H. Funke, J.L. Falconer, R.D. Noble, Improving SAPO-34 membrane synthesis, J. Memb. Sci. 444 (2013) 384–393.

[5] A.J. Kidney, W.R. Parrish, Fundamentals of Natural Gas Processing, Taylor & Francis Group, Boca Raton, FL, 2006.

[6] E.J. Dung, L.S. Bombom, T.D. Agusomu, The effects of gas flaring on crops in the Niger Delta, Nigeria, GeoJournal. 73 (2008) 297–305.

[7] S. Li, G. Alvarado, R.D. Noble, J.L. Falconer, Effects of impurities on $CO_2/CH_4$ separations through SAPO-34 membranes, J. Membr. Sci. 251 (2005) 59–66.

[8] T. Wu, M.C. Diaz, Y. Zheng, R. Zhou, H.H. Funke, J.L. Falconer, R.D. Noble, Influence of propane on $CO_2/CH_4$ and $N_2/CH_4$ separations in CHA zeolite membranes, J. Membr. Sci. 473 (2015) 201–209.

[9] J.F.M. Denayer, L.I. Devriese, S. Couck, J. Martens, R. Singh, P.A. Webley, G.V. Baron, Cage and window effects in the adsorption of n-alkanes on chabazite and SAPO-34, J. Phys. Chem. C. 112 (2008) 16593–16599.

[10] C. Nicolas, M. Pera-Titus, Nanocomposite MFI-alumina hollow fiber membranes: Influence of $NO_x$ and propane on $CO_2/N_2$ separation properties, Ind. Eng. Chem. Res. 51 (2012) 10451–10461.

[11] J.B. Lee, H.H. Funke, R.D. Noble, J.L. Falconer, High selectivities in defective MFI membranes, J. Memb. Sci. 321 (2008) 309–315.

[12] S. Himeno, T. Tomita, K. Suzuki, K. Nakayama, K. Yajima, S. Yoshida, Synthesis and permeation properties of a DDR-type zeolite membrane for separation of $CO_2/CH_4$ gaseous mixtures, Ind. Eng. Chem. Res. 46 (2007) 6989–6997.

[13] W. Zhu, F. Kapteijn, J.A. Moulijn, Shape selectivity in the adsorption of propane/propene on the all-silica DD3R, Chem. Commun. (1999) 2453–2454.

[14] C.D. Baertsch, H.H. Funke, J.L. Falconer, R.D. Noble, Permeation of aromatic hydrocarbon vapors through silicalite−zeolite membranes, J. Phys. Chem. 100 (1996) 7676–7679.

[15] J.C. Poshusta, V.A. Tuan, E.A. Pape, R.D. Noble, J.L. Falconer, Separation of light gas mixtures using SAPO-34 membranes, AIChE J. 46 (2000) 779–789.

[16] G. Guan, K. Kusakabe, S. Morooka, Synthesis and permeation properties of ion-exchanged ETS-4 tubular membranes, Microporous Mesoporous Mater. 50 (2001) 109–120.

[17] M. Hong, J.L. Falconer, R.D. Noble, Modification of zeolite membranes for $H_2$ separation by catalytic cracking of methyldiethoxysilane, Ind. Eng. Chem. Res. 44 (2005) 4035–4041.

[18] G. Guan, T. Tanaka, K. Kusakabe, K.-I. Sotowa, S. Morooka, Characterization of AlPO4-type molecular sieving membranes formed on a porous a-alumina tube, J. Membr. Sci. 214 (2003) 191–198.

[19] A.M. Avila, H.H. Funke, Y. Zhang, J.L. Falconer, R.D. Noble, Concentration polarization in SAPO-34 membranes at high pressures, J. Membr. Sci. 335 (2009) 32–36.

[20] S. Li, J.L. Falconer, R.D. Noble, SAPO-34 membranes for $CO_2/CH_4$ separations: Effect of Si/Al ratio, Micropor. Mesopor. Mater. 110 (2008) 310–317.

[21] M. Salmasi, S. Fatemi, S.J. Hashemi, MTO reaction over SAPO-34 catalysts synthesized by combination of TEAOH and morpholine templates and different silica sources, Sci. Iran. 19 (2012) 1632–1637.

[22] Y. Luo, N.O. Chisholm, H.H. Funke, M.Z. Chen, J.L. Falconer, R.D. Noble, Adsorption of gases in SAPO-34 and SSZ-13 zeolites, I&ECR Prep. (2014).

[23] M. Hong, S. Li, J.L. Falconer, R.D. Noble, Hydrogen purification using a SAPO-34 membrane, J. Memb. Sci. 307 (2008) 277–283.

[24] H.H. Funke, Y. Luo, M.Z. Chen, G.C. Anderson, J.L. Falconer, R.D. Noble, Measuring mixture adsorption by temperature-programmed desorption, Ind. Eng. Chem. Res. (2015).

[25] R. Krishna, J.M. van Baten, Investigating the influence of diffusional coupling on mixture permeation across porous membranes, J. Memb. Sci. 430 (2013) 113–128.

[26] R. Krishna, S. Li, J.M. van Baten, J.L. Falconer, R.D. Noble, Investigation of slowing-down and speeding-up effects in binary mixture permeation across SAPO-34 and MFI membranes, Sep. Purif. Technol. 60 (2008) 230–236.

# Chapter 4 Effect of Toluene Adsorption on Permeation Through SAPO-34 Membranes

This chapter will be submitted to the Journal of Membrane Science as: N.O. Chisholm, H.H. Funke, R.D. Noble, J.L. Falconer, Effect of Toluene Adsorption on Permeation Through SAPO-34 membranes.

## 4.1 Abstract

When 0.65 mol% toluene was added to feeds of $CO_2$ and $N_2$, permeances through SAPO-34 membranes decreased by 45% and 50%, respectively, even though toluene is too large to diffuse into the zeolite pores. Single-component adsorption isotherms for $CO_2$ and toluene were used to fit a dual-site Langmuir model to estimate surface coverages. The lower $CO_2$ permeance qualitatively correlated with the reduced $CO_2$ surface coverage. Experiments were performed at sub-atmospheric pressures so that ideal adsorbed solution theory could be used to estimate surface coverages. The estimated decrease in $CO_2$ coverage on the membrane surface due to competitively adsorbed toluene was sufficient to reduce the trans-membrane $CO_2$ driving force and account for the observed decrease in permeance.

## 4.2 Introduction

Zeolite membranes selectively permeate gases based on differences in molecular size, diffusivity, and loading. Because $CO_2$ has both higher loading and a higher diffusivity than $CH_4$ in SAPO-34 pores (0.38-nm pores), SAPO-34 membranes have high selectivities for separating

mixtures of $CO_2$ (0.33-nm kinetic diameter) and $CH_4$ (0.38 nm). The membranes are also selective for $N_2$ (0.36 nm) over $CH_4$, but the selectivity is lower because $N_2$ adsorbs more weakly than $CO_2$. Separating $CO_2$ or $N_2$ from $CH_4$ is important for purification of commercial natural gas streams. Both gases can be present at high concentrations in raw natural gas, and they decrease the gas heating value. In addtion, $CO_2$ can cause corrosion of pipelines. Both $CO_2/CH_4$ and $N_2/CH_4$ separation selectivities are affected by other impurities in natural gas, such as water and higher hydrocarbons. Even low concentrations of impurities can lower $CO_2$ and $N_2$ permeation by competing for adsorption sites and/or by changing the diffusivities. Propane (5 mol%) decreased $CO_2$ and $CH_4$ permeances in both SAPO-34 and SSZ-13 membranes at 270-kPa feed pressure. Propane also decreased separation selectivities, but it *increased* both $CO_2$ permeance and $CO_2/CH_4$ separation selectivity at 1.73-MPa feed pressure in SSZ-13 membranes [1]. Propane also decreased $H_2$ and $N_2$ permeances in SAPO-34 membranes at 350-kPa feed pressure, but increased $H_2/N_2$ separation selectivity [2]. Heating the membranes to 473 K overnight desorbed the propane and restored the original permeances. Water decreased permeances through SAPO-34 membranes even at ppm levels, but heating to 573 K desorbed the water and recovered the initial permeances [3,4]. Propane and water are small enough to enter SAPO-34 or SSZ-13 pores and compete for adsorption sites, and their presence inside the pores inhibits permeation of other gases. Natural gas also contains impurity molecules that are too large to enter the SAPO-34 pores, but these molecules may affect $CO_2/CH_4$ separations by adsorbing on the external surface of the SAPO-34 crystals. Keizer et al. showed that $CH_4$ flux through a silicalite-1 membrane at 298 K decreased by two orders of magnitude when 0.6% p-xylene, which is too large to enter the zeolite pores, was added to the feed whose pressure was 100 kPa [5]. Large molecules can also decrease $CO_2$ permeation due to concentration polarization; i.e., the large molecules can have higher concentrations near the

membrane surface and decrease the $CO_2$ partial pressure on the feed side, and thus the $CO_2$ driving force.

In this study, $CO_2$ and $N_2$ permeances were measured in the presence of toluene, which can be found at trace levels in some natural gas streams [6]. Even though toluene has a kinetic diameter of ~ 0.59 nm and is too large to enter SAPO-34 pores, it decreases $CO_2$ and $N_2$ permeances through SAPO-34 membranes by as much as 50%, even at concentrations of 0.65 mol% at a feed pressure of 172 kPa. This decrease in permeances was not due to concentration polarization [7] since $CO_2$ and $N_2$ permeances decreased only slightly in the presence of $SF_6$ (0.58-nm kinetic diameter). Although $SF_6$ is similar in size to toluene, it adsorbs more weakly on zeolite surfaces ($\Delta H_{ads}$ for $SF_6$ on NaX zeolite ~28 kJ/mol; $\Delta H_{ads}$ for toluene on Na-faujasite ~90 kJ/mol [8,9]), but their gas-phase diffusivities are similar. This suggest that toluene decreases permeances by competitively adsorbing on the external surface of SAPO-34 crystals and decreasing the driving force for the $CO_2$ and $N_2$ permeation.

The amounts of $CO_2$ and toluene adsorbed on the external membrane surface was estimated with a dual-mode Langmuir isotherm. However, the binary adsorption model required extrapolation to pressures exceeding available isotherm data. Moreover, the binary Langmuir isotherm model is thermodynamically inconsistent with the Gibbs adsorption isotherm for an ideal adsorbed solution [10]. Thus, permeation rates were also measured at feed pressures below 10 kPa, because toluene adsorption isotherms are available at these pressures, and the thermodynamically consistent ideal adsorbed solution theory (IAST) model can be used.

Crittenden et al. showed that IAST reliably predicted adsorbed amounts in mixtures of up to six volatile organic chemicals in aqueous solution [11]. Sakuth et al. measured toluene and 1-propanol adsorption on Y-zeolites and reported that the IAST adequately predicted binary

adsorption for a zeolite with Si/Al ratio of 100, but that a predictive real adsorbed solution theory (PRAST) model was necessary to describe the non-ideal adsorption behavior on Y-zeolites with lower Si/Al ratios [12]. Furmaniak et al. simulated adsorption of $CO_2$, $CH_4$, and $N_2$ on porous carbon and reported that the IAST model predicted surface coverages reasonably well. Simulated adsorbed amounts deviated from ideal behavior as the total pressure increased from 0.1 to 1.0 MPa, and deviation from ideal behavior was greater for more microporous systems [13]. In the current study, about 1% toluene decreased $CO_2$ permeances by about 20% at 10-kPa feed pressure. The decreased surface coverage of $CO_2$ in the presence of toluene predicted by the IAST model accounted for the decrease in $CO_2$ permeance, assuming that the driving force for permeation was proportional to the $CO_2$ loading on the external membrane surface.

## 4.3 Experimental Methods

### 4.3.1 Preparation and characterization of SAPO-34 membranes

SAPO-34 SAPO-34 membranes were prepared using hydrothermal synthesis, as reported previously [14]. Briefly, tubular alumina supports (Inopor) with 100-nm pores were cleaned in boiling DI water, and then seeded by rubbing SAPO-34 crystals onto the inner surface. The seed crystals were prepared in a Teflon autoclave by microwave heating a gel that contained Al(O-i-Pr)$_3$, tetraethyl ammonium hydroxide (TEAOH), deionized water, Ludox AS-40 colloidal silica, and $H_3PO_4$ (all chemicals from Sigma-Aldrich) with a composition of 1.0 $Al_2O_3$: 2.0 $P_2O_5$: 0.6 $SiO_2$: 4.0 TEAOH: 75 $H_2O$. The membrane layer was grown by placing the seeded supports into an autoclave with a synthesis gel containing the same precursors as the seed gel, but with a composition of 0.85 $Al_2O_3$: 1.0 $P_2O_5$: 0.3 $SiO_2$: 2 TEAOH: 155 $H_2O$. The autoclave was then held at 483 K for 6 h. After synthesis, the membranes were cooled, rinsed for 24 h in DI water to remove synthesis gel residue, calcined at 823 K for 8 h with heating and cooling rates of 1 K/min, and then

stored in an oven at 473 K in air. Cross-sectional SEM images of a membrane prepared previously using the same procedures [14] showed a 3-μm thick SAPO-34 layer, and SEM images of the membrane surface showed 1-3 μm cubic crystals.

The flux through defects in the SAPO-34 membrane was estimated from the $CO_2$/isobutane ideal selectivity. Isobutane (0.50-nm kinetic diameter) is too large to enter the SAPO-34 pores and thus only permeates through defects. The membrane used for measurements at 172-kPa feed pressure had a $CO_2$/isobutane ideal separation selectivity of about 80 at room temperature and 140-kPa feed pressure. The percentage of $CO_2$ flux through defects for this membrane was estimated to be less than 1.5%, but as much as 30% of the $N_2$ flux was through defects if Knudsen diffusion dominated the defect permeation. SAPO-34 membranes with much higher $CO_2$/isobutane selectivities have been reported previously [1], but the small defect contribution to the overall $CO_2$ flux of this membrane does not affect the conclusions. The single-gas permeances at room temperature were $2.0 \times 10^{-6}$ mol/($m^2$ s Pa) for $CO_2$ and $1.6 \times 10^{-7}$ mol/($m^2$ s Pa) for $N_2$ at 172-kPa feed pressure.

A second SAPO-34 membrane was used for permeation measurements at 10-kPa feed pressure. This membrane had a $CO_2$/isobutane ideal separation selectivity of 2,200 at room temperature and 125-kPa feed pressure. Carbon dioxide flux through defects was estimated to be 0.05% of the total $CO_2$ flux for this membrane. The single-gas $CO_2$ permeance was $4 \times 10^{-6}$ mol/($m^2$ s Pa) at 10-kPa feed pressure and 2.1-kPa permeate pressure.

### 4.3.2 Characterization of SAPO-34 crystals

The same hydrothermal synthesis used to prepare the membranes was also used to prepare SAPO-34 crystals for adsorption measurements. These crystals were cubic with sizes ranging from 0.4 - 3 μm, as determined by SEM. The XRD peaks were consistent with the SAPO-34 structure,

and no other peaks were detected. Their BET surface area was 580 $m^2/g$, which is in the range of values reported in the literature (483 – 677 $m^2/g$) [15,16]. Toluene adsorption isotherms were measured with a Quantachrome AS1-C volumetric adsorption system.

### 4.3.3 Gas permeation measurements at 172 kPa

Single-component and mixed-gas permeances were measured in a flow system equipped with computer-controlled mass flow controllers. The membranes were sealed in stainless steel modules with Viton o-rings, and toluene was added to the feed by bubbling $CO_2$ or $N_2$ through glass bubblers filled with liquid toluene. A thermostat maintained the bubbler temperature slightly below ambient (290 K) to prevent toluene condensation in the lines. The toluene-saturated streams were then mixed with $CO_2$ or $N_2$ streams to obtain the desired toluene feed concentration. Retentate and permeate flow rates were measured with soap film flow meters. No sweep gas was used. The toluene feed compositions were calculated from the toluene vapor pressure and the gas flow rates, and these calculated compositions were consistent with GC analysis.

To determine the effect of toluene or $SF_6$ on permeation through the membrane, initially single-component $CO_2$ or $N_2$ (both AirGas UHP) permeances were measured, and then up to 0.65% toluene (Sigma Aldrich) or up to 1.5% $SF_6$ (AirGas) was added to the feed. The total feed flow rate was 300 sccm, the feed pressure was 172 kPa, and the permeate pressure was 85 kPa. An adsorption trap filled with 3A zeolite was placed at the inlet of the membrane module to remove water or other impurities from the feed. This trap only slightly affected equilibration times after addition of toluene to the feed because toluene is too large to enter the 3A pores.

### 4.3.4 Gas permeation measurements at 10 kPa

Feed and permeate pressures of 10 and 2.1 kPa, respectively, were obtained with mechanical vacuum pumps and controlled with backpressure regulators. The toluene feed

compositions were calculated from the toluene vapor pressure and the gas flow rates. The toluene concentrations were confirmed by adsorbing toluene onto a packed bed of activated carbon from a flowing helium stream at the $CO_2$/toluene experimental pressures, and measuring the weight gain of the carbon bed. Helium was used as the carrier gas because it did not adsorb significantly on the activated carbon.

## 4.4 Results and discussion

### 4.4.1 Effect of toluene on $CO_2$ and $N_2$ permeances at 172 kPa

The SAPO-34 membrane had a single-gas $CO_2$ permeance of $2.0 \times 10^{-6}$ mol/($m^2$ Pa s) at 293 K and a feed pressure of 172 kPa (82-kPa permeate pressure). As shown in Figure 4.1, when 1.1 kPa (0.65%) toluene was added to the feed, the $CO_2$ permeance decreased by 45% within a few minutes; it reached steady state after about 30 min because toluene only adsorbs on the external surface of the SAPO-34 crystals. At lower toluene concentrations, permeances reached steady state faster (not shown). In contrast, as previously shown, $CO_2$ permeances reached steady state slowly (2 d) after the addition of propane to a $CO_2$ feed because propane slowly diffuses into SAPO-34 pores [2]. When toluene was removed from the feed, the $CO_2$ permeance increased to within 10% of its initial permeance. The $CO_2$ permeance fully recovered after heating the membrane to 473 K overnight in air. Some toluene may have strongly adsorbed on SAPO-34; Nagao et al. found that toluene was not completely removed from dehydroxylated $TiO_2$ by evacuation for 4 h at 298 K [17]. They concluded from IR measurements that surface Ti atoms interact strongly with the π-electrons of the aromatic ring to prevent complete desorption, and toluene may have similar strong π-bonding at sites on the SAPO-34 surface.

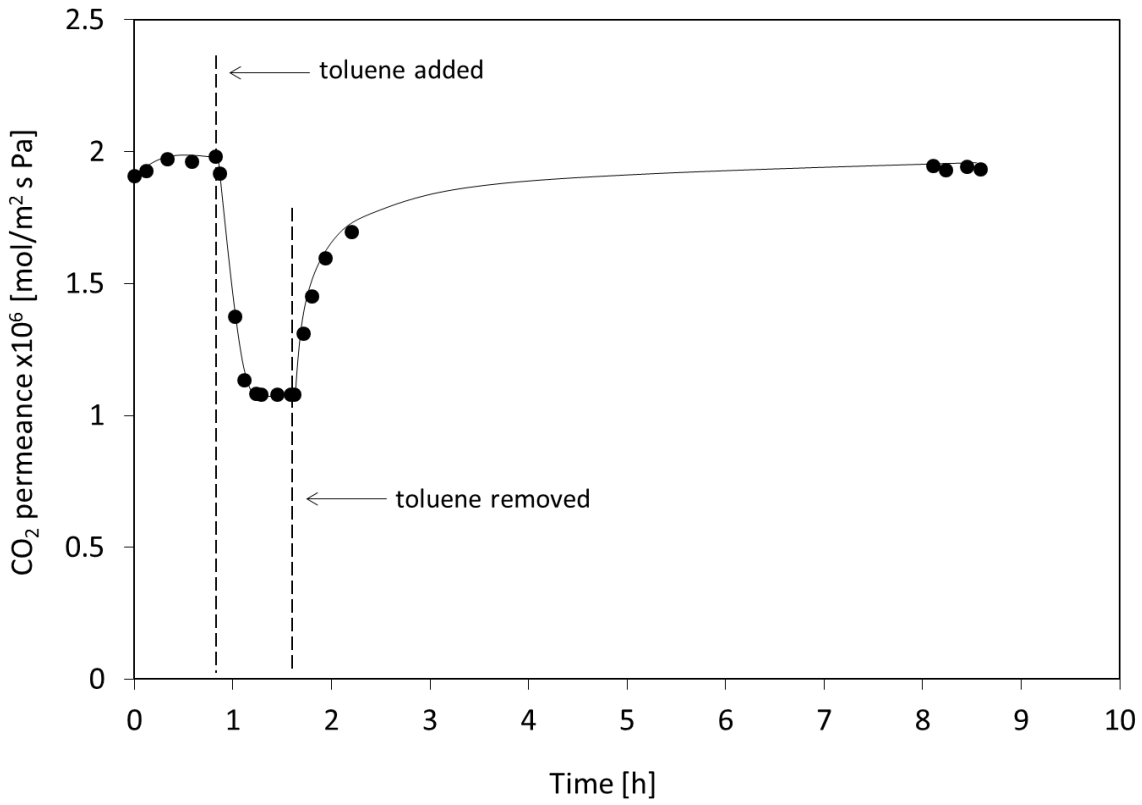


**Figure 4.1.** Carbon dioxide permeance through a SAPO-34 membrane at 298 K and a total feed pressure of 172 kPa. The permeance was measured initially, after 1.1 kPa (0.65 mol%) toluene was added to the feed, and after toluene was removed from the feed.

Figure 4.2 shows that the steady-state $CO_2$ permeances decreased as the toluene partial pressure increased. After each measurement at a given toluene partial pressure, the membrane was heated overnight to remove toluene. Pure-component $CO_2$ permeance measured at the start of each experiment shows that the $CO_2$ permeance in the absence of toluene did not change over the course of the experiments (Figure 4.2). Toluene had a similar effect on $N_2$ permeance, as shown in Figure 4.3. When 1.1-kPa toluene was added to the feed, the $N_2$ permeance decreased by 50%.

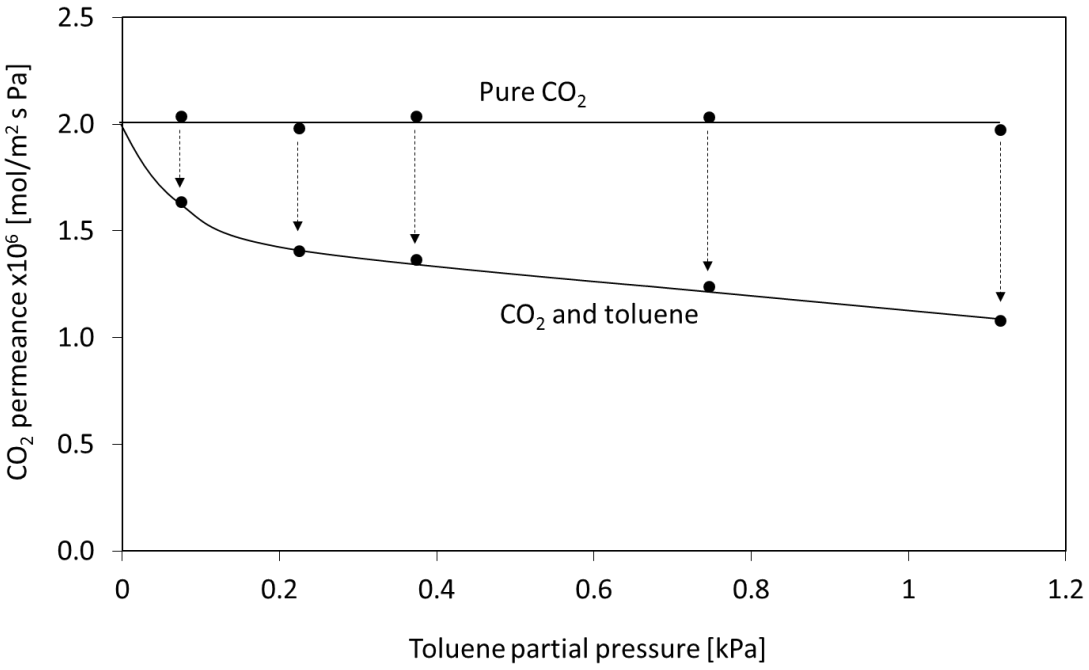


**Figure 4.2.** Carbon dioxide permeance through a SAPO-34 membrane at 298 K and a total feed pressure of 172 kPa. The upper line shows single-gas $CO_2$ permeance, and the arrows indicate the change in steady-state permeance after toluene was added.

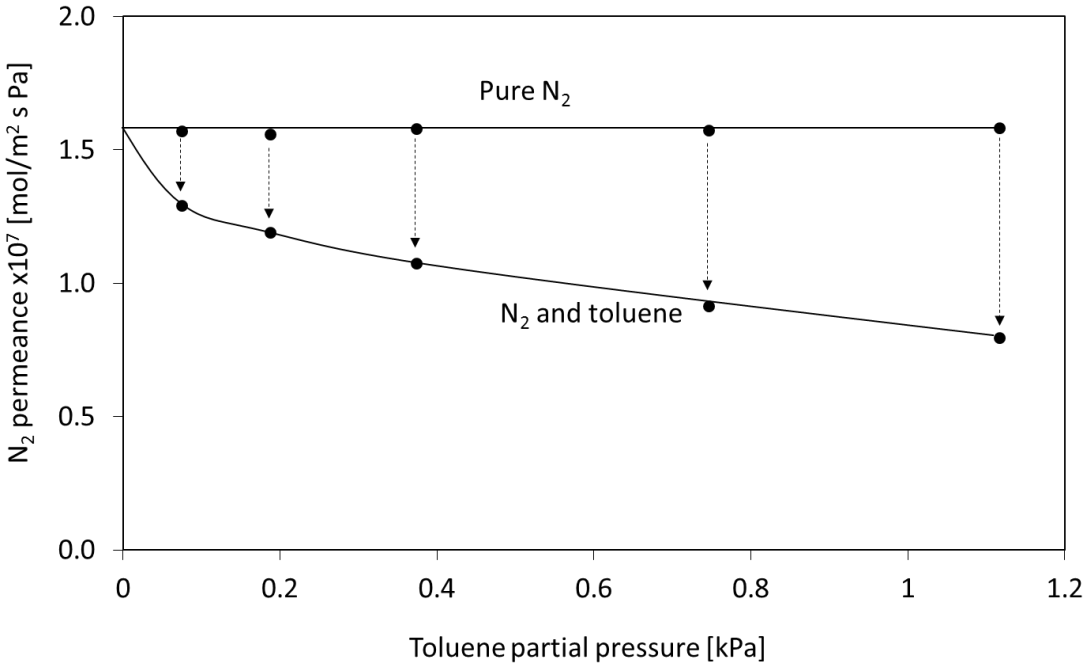


**Figure 4.3.** Nitrogen permeance through a SAPO-34 membrane at 298 K and a total feed pressure of 172 kPa. The upper line shows single-gas $N_2$ permeance, and the arrows indicate the change in steady-state permeance after toluene was added.

### 4.4.2 Effect of toluene on $CO_2$ membrane permeance at 10 kPa

The $CO_2$ permeance of a second SAPO-34 membrane was measured in the presence of toluene at a feed pressure of 10 kPa. The low pressure experiments allowed for analysis with the IAST in the range that the toluene adsorption isotherm was measured. This membrane had a $CO_2$ permeance of about $4x10^{-6}$ mol/($m^2$ Pa s) at 125-kPa feed pressure. As shown in Figure 4.4, when when toluene was added to the feed, the $CO_2$ permeance decreased. Steady-state was reached after 30 min following each increase in toluene concentration. At the highest toluene concentration (0.87-kPa toluene, 8.5 mol% toluene), the $CO_2$ permeance decreased by 19%. When toluene was removed from the feed, the single-gas $CO_2$ permeance recovered within 60 min. The relatively short time to recover the initial $CO_2$ permeance supports that toluene only adsorbed to the external surface.

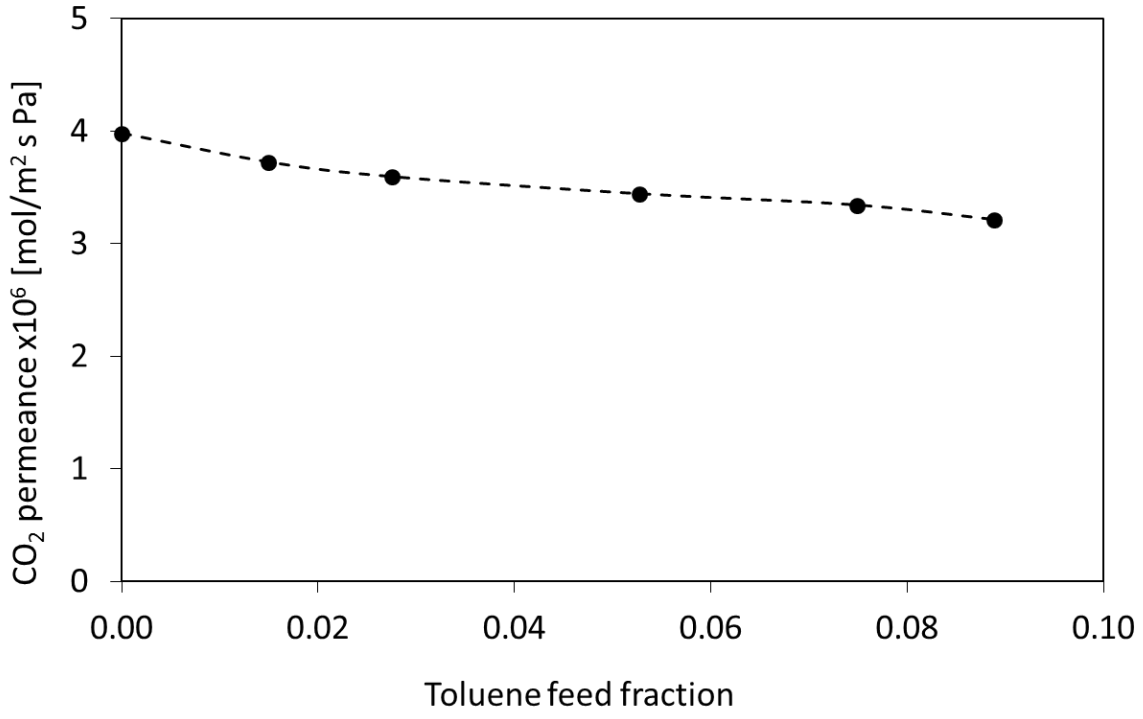


**Figure 4.4.** Steady-state $CO_2$ permeances as a function of toluene feed fraction at a feed pressure of 10 kPa and a permeate pressure of 2 kPa.

### 4.4.3 Toluene adsorption on SAPO-34 crystals

The decrease in $CO_2$ and $N_2$ permeances in the presence of toluene suggests that toluene either blocks access to external-surface zeolite pores or decreases coverage of the permeating species by competitive adsorption. Multicomponent adsorption models can estimate binary adsorption equilibria based on single-component adsorption isotherms, and thus toluene isotherms on SAPO-34 crystals were measured.

The external surface area of SAPO-34 crystals was approximated by the surface area of uncalcined crystals, which was measured by $N_2$ BET as 37 $m^2/g$. Nitrogen only adsorbed on the external surface of uncalcined crystals because the SAPO-34 pores were filled with the structure-directing template, tetraethylammoniumhydroxide. Toluene adsorption isotherms were also measured on the uncalcined crystals, as shown in 4.5 at three temperatures. Isotherms on calcined crystals were similar because toluene cannot enter the SAPO-34 pores, but toluene adsorption on uncalcined crystals was used for modeling so that $CO_2$ adsorption on the external surface could be compared for the same sample. The toluene isotherms at 296 K show type-II multilayer adsorption well below saturation pressure (3.4 kPa at 296 K). The desorption isotherm exhibits hysteresis, which may be due to capillary condensation between the crystals or stronger π-bonding with the surface after toluene reorganized at higher loading than when it initially adsorbed. Similarly, Nagao et al. observed type-II isotherms for toluene adsorption at 298 K on $TiO_2$ rutile particles [17]. They observed multilayer adsorption above $p/p_0 = 0.05$ and concluded, based on BET analysis, that a toluene molecule occupied 0.602 $nm^2$ on rutile $TiO_2$. Molecular models predict that a toluene molecule adsorbed flat on a surface occupies about 0.47 $nm^2$ [18], and thus, Nagao et al. suggested that toluene packs relatively loosely on the rutile surface.

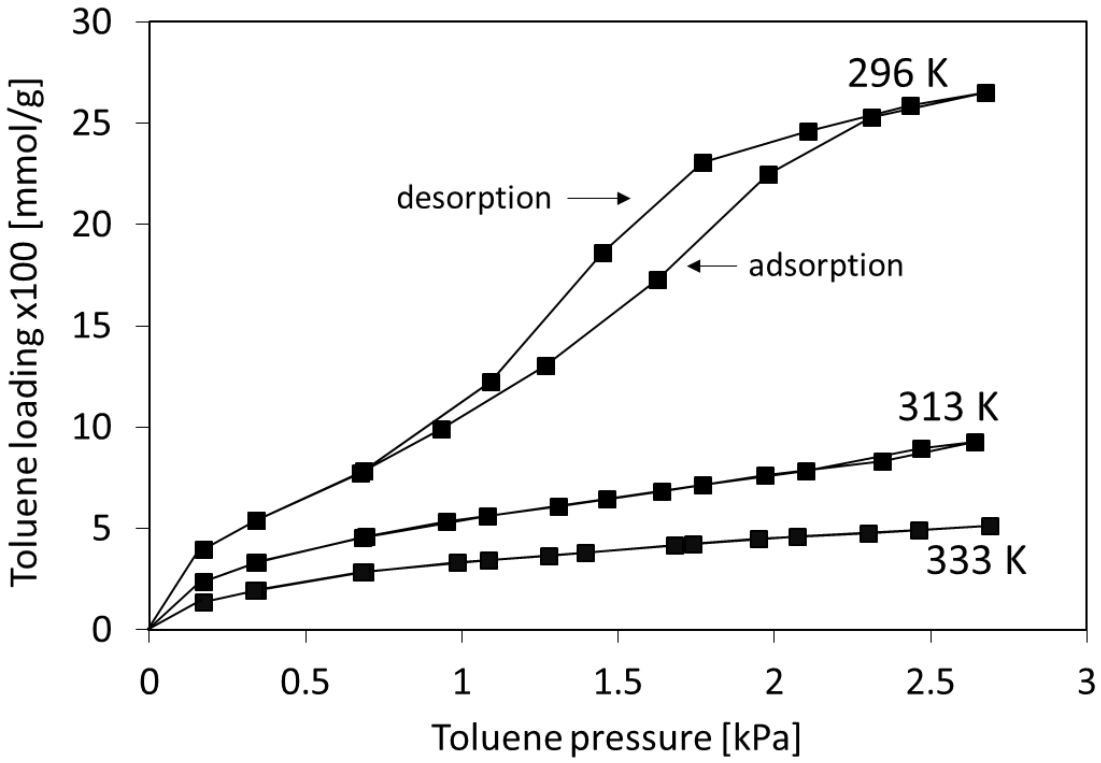


**Figure 4.5.** Toluene adsorption isotherms on uncalcined SAPO-34 crystals at temperatures of 296, 313, and 333 K.

The toluene adsorption isotherm at 296 K, when fit to the BET model, yielded a monolayer coverage of 80 μmol/g. The calculations indicate that monolayer coverage was obtained at about 0.8 kPa, which is less than 20% of the toluene saturation pressure at 296 K. This coverage corresponds to an area of 0.77 $nm^2$ per toluene molecule. Even though SAPO-34 is crystalline, its external surface may be irregular because of its porosity and non-ideal termination of the crystal planes. This irregular surface could prevent dense packing of adsorbed molecules [19]. Thus, toluene may occupy more area on the SAPO-34 surface than the 0.602 $nm^2$ per molecule coverage reported for dense $TiO_2$ crystals by Nagao et al. [17]. Nitrogen, which was used to determine external surface area, is much smaller than toluene and thus can pack more densely on a rough surface.

### 4.4.4 Modeling competitive external surface adsorption

Competitive adsorption between toluene and $CO_2$ or $N_2$ on the membrane surface qualitatively explains the observed decreases in $CO_2$ and $N_2$ permeances after adding toluene to the feed. The Maxwell-Stefan model predicts transport through zeolite membranes by assuming gas molecules adsorb on the zeolite external surface before entering the membrane pores [20,21], and thus a lower $CO_2$ external surface concentration due to competition with adsorbed toluene should reduce the driving force for $CO_2$ permeation.

Because adsorption data are not available at sufficiently high pressures to use the IAST, the surface coverages of $CO_2$ and toluene for a feed pressure of 172 kPa was estimated with a binary Langmuir model:

$$\frac{n_i}{Q_i} = \frac{K_i P_i}{1 + K_i P_i + K_j P_j}$$

The total coverage, $Q_i$, and equilibrium constant, $K_i$, for the Langmuir isotherm were estimated from single-component toluene and $CO_2$ adsorption isotherms (Figures 4.6 and 4.7). The loading for component $i$ is $n_i$. The Langmuir parameters for toluene were determined from a fit between 0 and 1 kPa, and the parameters for $CO_2$ were calculated from the isotherms measured between 0 and 100 kPa (Table 4.1). The model qualitatively accounts for the difference in surface areas of the different sized molecules.

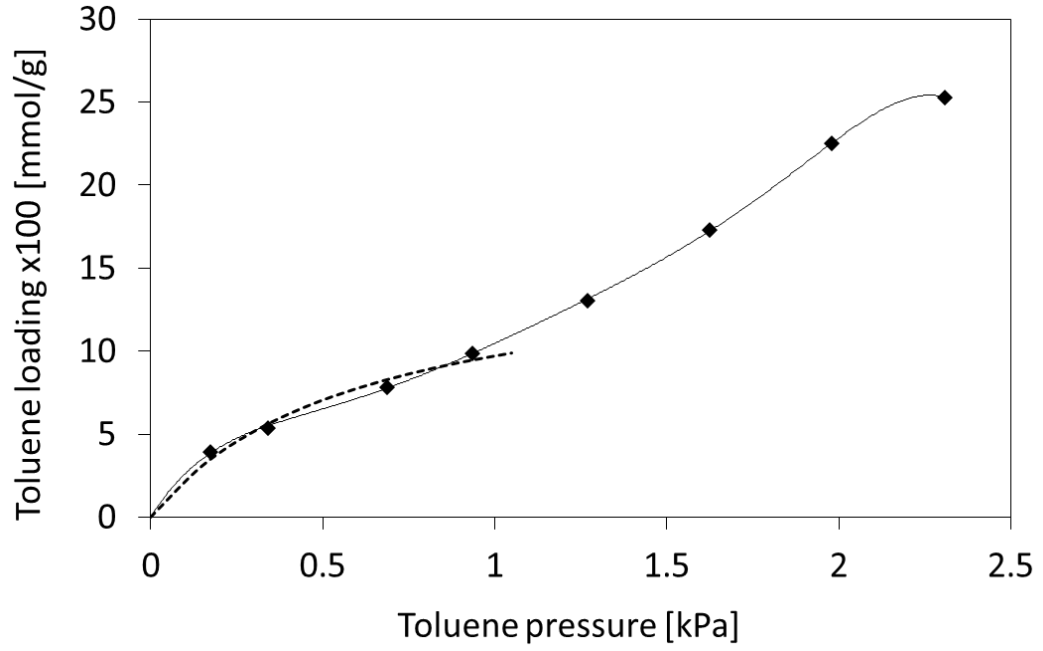


**Figure 4.6.** Toluene adsorption isotherm on uncalcined SAPO-34 crystals (diamonds) at 296 K: dashed line - Langmuir fit; solid line - polynomial fit.

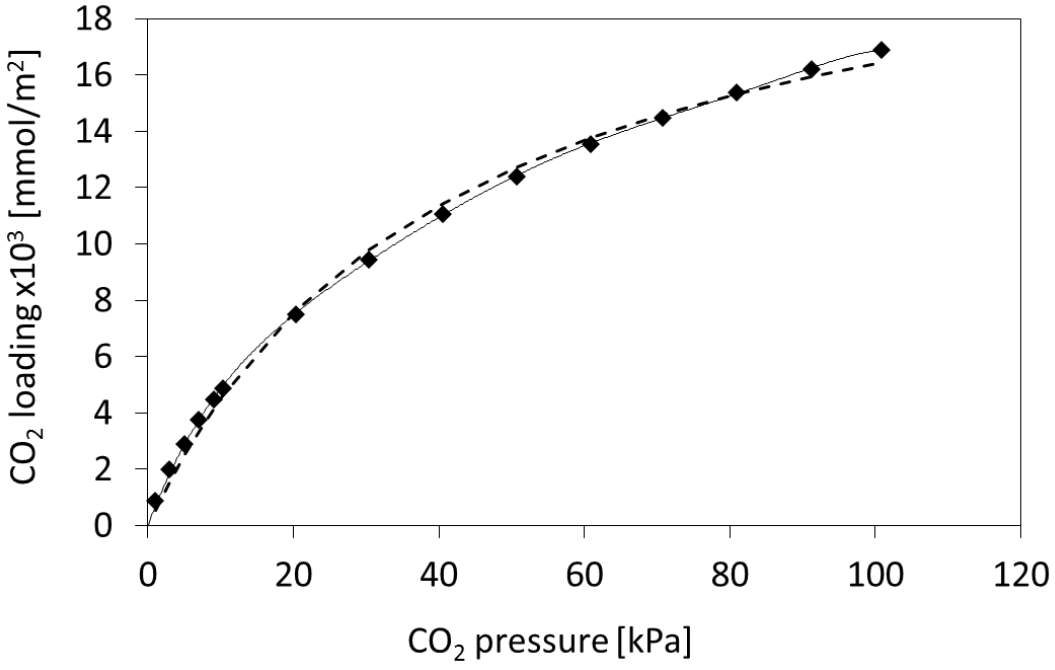


**Figure 4.7.** Carbon dioxide adsorption isotherm on uncalcined SAPO-34 crystals (diamonds) at 296 K: dashed line – Langmuir fit; solid line – polynomial fit.

**Table 4.1.** Binary Langmuir isotherm parameters

| | $K_{eq}$ [$Pa^{-1}$] | Q [mol/g] |
|---|---|---|
| $CO_2$ | $2.4 \times 10^{-5}$ | $6.8 \times 10^{-4}$ |
| Toluene | $1.6 \times 10^{-3}$ | $1.6 \times 10^{-4}$ |

The binary Langmuir isotherm model predicts that toluene reduces $CO_2$ coverage, and the decrease qualitatively correlates with the lower permeances (Figure 4.8). The $CO_2$ concentration in the membrane was calculated from fluxes using Fick's law and assuming the $CO_2$ diffusion coefficient in the membrane was independent of $CO_2$ loading because loading was low at low pressure.

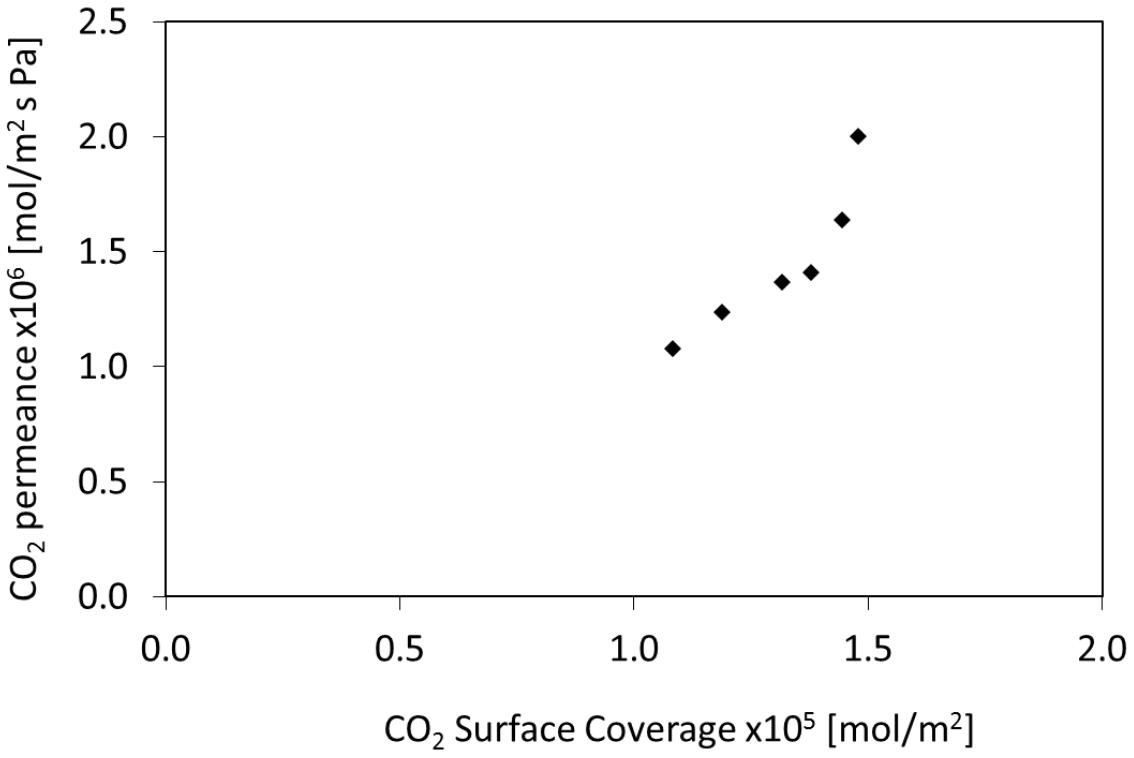


**Figure 4.8.** Carbon dioxide permeance at 172k Pa feed pressure vs $CO_2$ surface coverage (from Langmuir isotherm).

The accuracy of the predictions at 172-kPa feed pressure is limited because $CO_2$ isotherms were only measured up to 100 kPa (Figure 4.7), and the Langmuir model described the toluene adsorption isotherms only to about 1 kPa, and without convincing accuracy (Figure 4.6). The The toluene and $CO_2$ coverages at the pressures of the permeation experiments were thus extrapolated using the Langmuir isotherm model. The multicomponent Langmuir isotherm has also been criticized because it does not account for the spreading pressure [22].

Co-adsorption of $CO_2$ and toluene on the SAPO-34 external surface at pressures below 10 kPa was modeled with ideal adsorbed solution theory (IAST), which is generally more accurate than the Langmuir model and also thermodynamically consistent. The IAST defines a spreading pressure as the two-dimensional equivalent of the partial pressure in the gas phase to calculate equilibrium coverages of adsorbed species on a surface. However, the model is only applicable in the spreading-pressure range calculated from available single-component adsorption data. Toluene adsorption was measured up to 2.3 kPa, so $CO_2$/toluene membrane experiments were performed with toluene partial pressures below 1 kPa. Following the direction of Myers and Prausnitz [22], $CO_2$ and toluene single-component adsorption data were fit with a polynomial function as shown in Figures 4.6 and 4.7,

$$n_i^\circ = F_i(P_i^\circ)$$

and then the spreading pressure, $\pi_i^\circ$, on the SAPO-34 surface (Figure 4.9) was determined by numerical integration according to the following thermodynamic relation:

$$\pi\left(P_i^\circ\right) = \frac{RT}{A}\int_{P=0}^{P=P'} \frac{n_i^\circ(P)}{P}\, dP = \psi_i\left(P_i^\circ\right)$$

Finally the following equations were solved simultaneously by specifying the log-mean vapor phase composition going from feed to retentate, and the total feed pressure:

$$\pi^{\circ}_{tol} = \psi_{tol}\left(P^{\circ}_{tol}\right)$$

$$\pi^{\circ}_{CO_2} = \psi_{CO_2}(P^{\circ}_{CO_2})$$

$$P\, y_{tol} = P^{\circ}_{tol}\, x_{tol}$$

$$P\, y_{CO_2} = P^{\circ}_{CO_2}\, x_{CO_2}$$

$$\pi^{\circ}_{tol} = \pi^{\circ}_{CO_2}$$

$$x_{tol} + x_{CO_2} = 1$$

$$y_{tol} + y_{CO_2} = 1$$

where $n_i°$ is the adsorption isotherm of pure component $i$, $F_i(P_i^{\circ})$ is the numeric function for loading (polynomial fit with intercept at 0), $P_i^{\circ}$ is the pressure of pure component $i$, $\pi_i^{\circ}$ is the spreading pressure of pure component $i$, $\psi_i(P_i^{\circ})$ is the numeric function for spreading pressure (polynomial fit with intercept at 0), $x_i$ is the surface composition of component $i$, $y_i$ is the vapor composition of component $i$, and $P$ is the total pressure. Figure 4.9 shows the IAST solutions for each experimental composition from Figure 4.4, where the spreading pressures of toluene and $CO_2$ must be equal, and the surface composition is determined by a lever rule calculation around the total pressure, 10 kPa [22]. At the constant feed pressure of 10 kPa, increasing the toluene vapor concentration increased toluene surface coverage, increased spreading pressure (and total surface coverage), and decreased external $CO_2$ surface coverage.

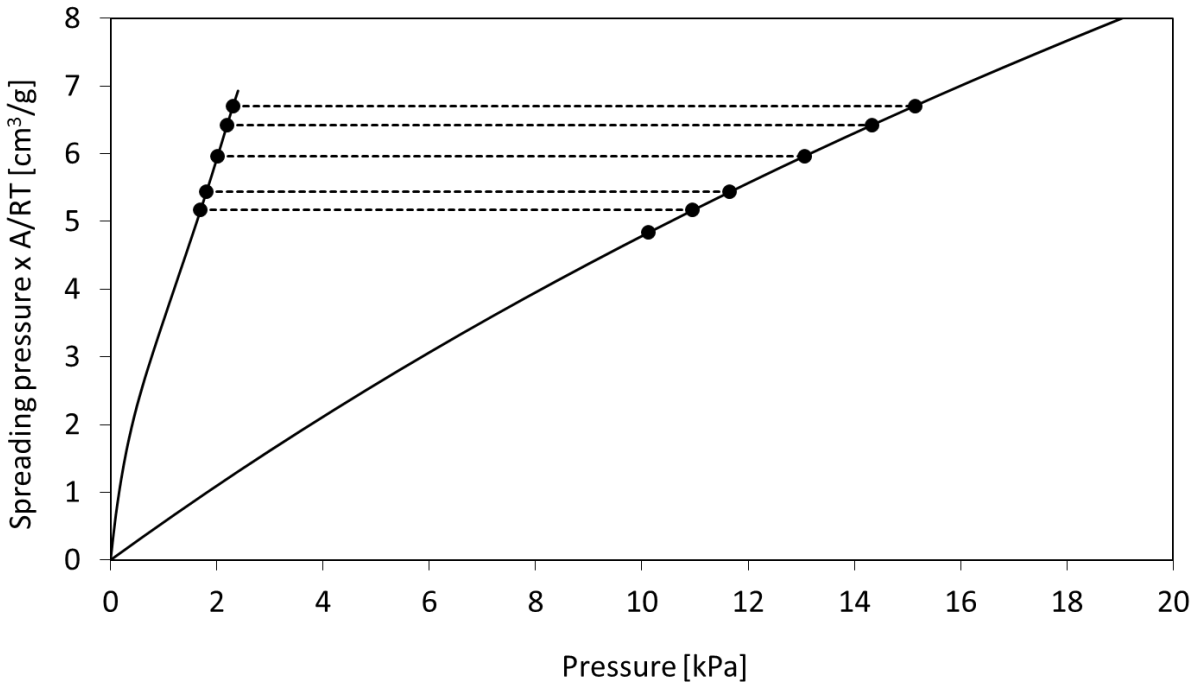


**Figure 4.9.** Single-component spreading pressure of toluene and $CO_2$ as a function of pressure. Each set of points with the same spreading pressure is a solution for specific experimental parameters, and the single point represents pure $CO_2$.

The decrease in $CO_2$ coverages estimated by the IAST as a result of competitive adsorption with toluene are sufficient to explain the reduced $CO_2$ permeances. The analysis assumes that the surface coverage of $CO_2$ is directly proportional to the $CO_2$ concentration in the pores near the membrane surface. Adding toluene lowers the $CO_2$ surface coverage, which lowers the $CO_2$ concentration in the membrane, and thus the driving force for permeation. Figure 4.10 shows the decrease in $CO_2$ external surface coverage as a function of toluene feed concentration. For a feed with 8.5 mol% toluene, the $CO_2$ surface coverage was reduced by about 20%.

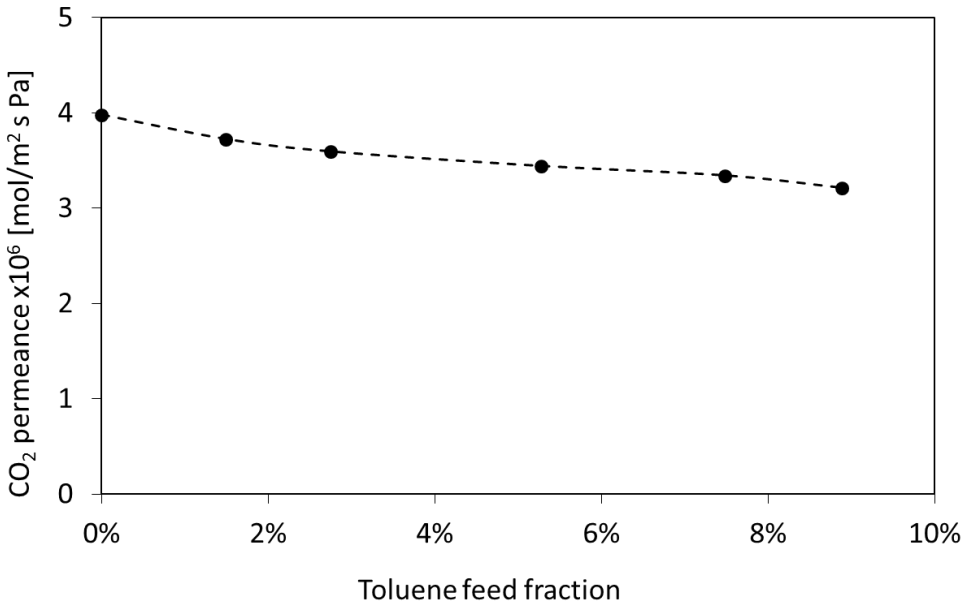


**Figure 4.10.** Log-mean feed/retentate $CO_2$ coverage of external membrane surface as a function of toluene feed fraction.

Figure 4.11 shows the correlation between $CO_2$ permeance and the driving force for $CO_2$ transport (log-mean difference between the calculated $CO_2$ external surface coverage on the feed/retentate and permeate side). At the highest toluene concentrations (lower $CO_2$ loadings and thus lower $CO_2$ driving force), the decrease in $CO_2$ permeance was about 10% less than the predicted drop of 30% (20.% measured vs 30.% calculated at 8.5% toluene in the feed). This discrepancy may be due to non-ideal adsorption on the external surface.

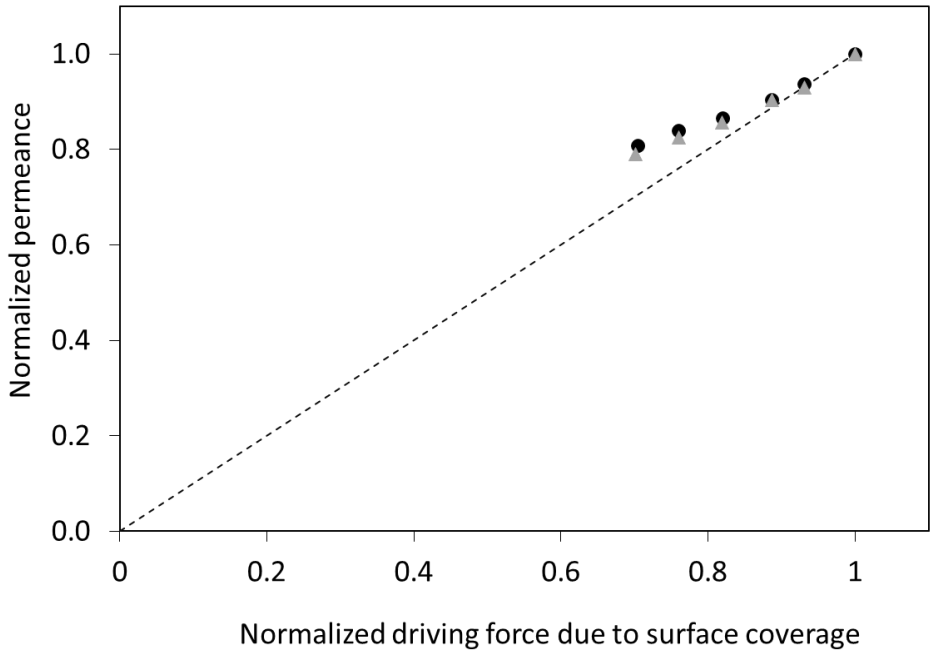


**Figure 4.11.** Normalized $CO_2$ permeance versus normalized effective driving force for two measurements. Carbon dioxide permeance was normalized to the pure-$CO_2$ permeance, and effective driving force was normalized to the pure-$CO_2$ trans-membrane driving force. The line indicates a 1-to-1 correlation.

Since the measured decrease in permeance was less than calculated, interference by other processes such as concentration polarization, blocking of the external zeolite pores by adsorbed toluene, or condensation of liquid toluene on the membrane surface is likely small because all these processes would further decrease permeances.

### 4.4.5 Effect of concentration polarization

The negligible contribution of concentration polarization to the decrease in $CO_2$ permeance when toluene was added to the feed at 172-kPa feed pressure was confirmed by adding $SF_6$ instead of toluene to the feed at similar concentrations to those used for toluene. Concentration polarization is observed when the diffusion of the slower-permeating (rejected) species in the gas phase is slower than the convective flux to the membrane surface due to permeation. The slower-

permeating or rejected molecules then accumulate near the membrane surface and decrease the concentration and thus the driving force of the permeating compounds [7].

Adsorbed $SF_6$ ($P_{sat}$ = 1.2 MPa) decreases $CO_2$ surface loadings much less than toluene ($P_{sat}$=2.9 Pa) does because $SF_6$ adsorbs much less strongly than toluene [8,9]. Therefore, any decrease in $CO_2$ permeance after adding $SF_6$ to the $CO_2$ feed should indicate an upper boundary that could be expected for the effect of concentration polarization because $SF_6$ (0.5 nm) is too large to permeate through the zeolite pores. Figure 4.12 shows that 1.2-kPa toluene decreased the $CO_2$ permeance 10 times as much as $SF_6$ at the same partial pressure (interpolated). The $CO_2$ permeance decreased by the same amount, 18%, for an $SF_6$ pressure of 4 kPa and a toluene pressure of 0.1-kPa toluene. Since $SF_6$ (MW = 146) is heavier than toluene (MW= 96), the $SF_6$ has a bulk diffusivity that is about 20% lower than that of toluene [23], and thus concentration polarization for $CO_2$/$SF_6$ mixtures should be only slightly larger than for $CO_2$/toluene mixtures. Based on these estimates, concentration polarization should account for less than 10% of the decrease in $CO_2$ permeance at 1.2-kPa toluene pressure. The 20% decrease in $CO_2$ or $N_2$ permeation observed would require a toluene partial pressure of ~34 kPa, which is well above its saturation pressure of 2.9 kPa.

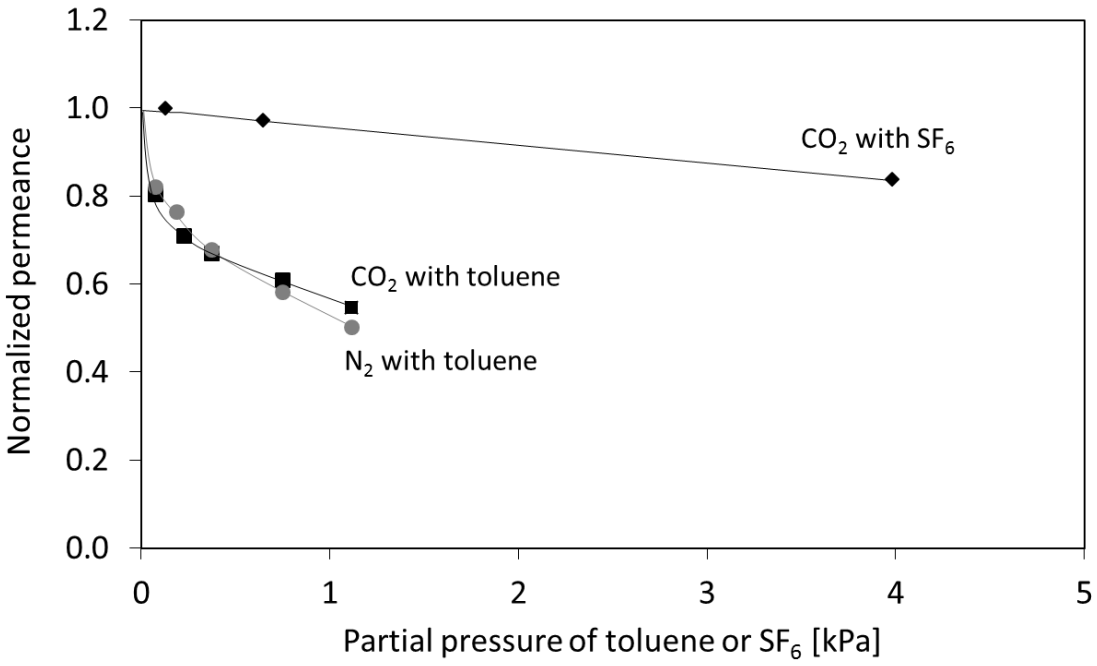


**Figure 4.12.** Normalized $CO_2$ and $N_2$ permeances through SAPO-34 membrane as a function of toluene partial pressure, and normalized $CO_2$ permeance as a function of $SF_6$ partial pressure. All measurements were at 298 K and a total feed pressure of 172 kPa.

The increase in toluene partial pressure near the membrane surface due to concentration polarization was also estimated using a transport model to more-accurately determine surface coverage. With a Reynolds number of about 100 (laminar-flow), the boundary layer thickness, δ, at the membrane surface was determined from the membrane dimensions, the gas velocity ($v$ = 0.15 m/s), and the gas diffusivity of toluene ($D$ = 8.7x10$^{-6}$ m$^2$/s) [24]:

$$\delta = \frac{1}{A}\left(\frac{v\,d}{D}\right)^{-1/3} L^{1/3} d^{2/3}$$

where $d$ is the membrane inner diameter (6 mm), L is the membrane length (30 mm), and $A$ is determined from the Graetz Number (Gz = $(v/D)d^2/L$), which is greater than 10, so $A = 2.43$ [25]. The boundary layer thickness was about 1.2 mm.

The Peclet number (Pe = v δ/D) was used to determine the polarization index, *I*, which is the ratio of the concentration near the membrane surface to the bulk concentration. The polarization index is [7,25]:

$$I = e^{Pe} + \beta(1 - e^{Pe})$$

where $\beta$ is the enrichment factor, which is the ratio of the permeate concentration to the retentate concentration. With I = 0.9996 for $CO_2$ and I = 0.99999 for $N_2$, the effect of concentration polarization on the $CO_2$ and $N_2$ surface concentrations in the presence of toluene is negligible. For the $CO_2$/toluene feed, the toluene concentration near the surface increased by about 6% over the bulk concentration, but for the $N_2$/toluene feed, the toluene concentration near the surface only increased by about 0.2% over the bulk concentration for all toluene concentrations used because $N_2$ fluxes are lower.

### 4.4.6 Transport resistance of condensed toluene

Even though the $SF_6$ measurements and transport calculations suggest that concentration polarization is not significant for toluene, an increase in toluene partial pressure near the membrane surface close to its saturation pressure may condense toluene, and the resulting liquid film could decrease $CO_2$ and $N_2$ permeances. The adsorption isotherms in Figure 4.5 indicate that multilayers form well below the toluene saturation pressure, and thus, even a small increase in toluene concentration could cause a large increase in surface coverage and formation of a liquid film. The thickness of a liquid layer that would cause the observed decreases in $CO_2$ permeances, neglecting any changes in $CO_2$ surface coverage due to competitive adsorption, was estimated using a resistance in series model [26]:

$$R_{tot} = R_1 + R_2$$

where $R$ is the resistance to flow and $R = P/(l\ \Delta C)$, $P$ is the membrane permeance, $l$ is the membrane thickness (3 μm for the zeolite layer), and $\Delta C$ is the concentration change across the membrane.

Fick's Law was used to estimate the film thickness. The interfacial resistance between the liquid film and the zeolite surface was assumed to be zero, and the added resistance was assumed to be due solely to $CO_2$ diffusion through a condensed toluene film. The diffusion coefficient of $CO_2$ in toluene is $4.9 \times 10^{-9}$ $m^2/s$ [27], and the Henry's Law constant for $CO_2$ in toluene is 965 (Pa $m^3$)/mol [28]. For the observed changes in permeance, the toluene film would be about 0.5 μm thick for the lowest toluene concentration and 2.1 μm for the highest toluene concentration and thus could form within few minutes at the toluene flowrates used for the experiments. However, a continuous liquid film on the surface should decrease $CO_2$ surface coverage even more than the amount calculated with the competitive adsorption models that assume a gas/solid equilibrium. Since the observed decreases in permeance are less than those calculated, additional resistance of a liquid film and consequently, a high toluene surface coverage is unlikely.

The $CO_2$ permeance could also decrease if toluene condensed in small gaps between crystals. Those gaps are unlikely to penetrate the entire zeolite layer because high $CO_2$/isobutane selectivities were observed with these membranes. Capillary condensation in those gaps would increase the effective membrane thickness because permeating gases would have to diffuse longer distances. The average gap size that could be blocked by condensed toluene was estimated from the Kelvin equation as 1.3 nm at the lowest toluene concentrations and 5.2 nm at the highest. However, if the surface area of those gaps is a large fraction of the overall membrane area, a large decrease in $CO_2$ surface coverage in these gaps due to complete coverage by a liquid toluene film would also result is larger-than-observed decreases in $CO_2$ permeances. Thus, similar to the

conclusions drawn from the assumptions of a liquid film as a result of concentration polarization, capillary condensation of toluene is not likely to affect $CO_2$ permeances.

## 4.5 Conclusions

Addition of small amounts of toluene significantly decreased $CO_2$ and $N_2$ permeances through SAPO-34 membranes, even though toluene is too large to enter the SAPO-34 pores. Steady state was reached within 30 min after toluene addition. Through extrapolation to the experimental pressure of 172 kPa, a Langmuir binary adsorption model gave a qualitative correlation between reduced surface coverage and reduced permeances. Experiments at lower pressures allowed for analysis with an IAST model that supported the hypothesis that the decrease in $CO_2$ permeances was due to reduced concentration of $CO_2$ on the external surface of the membrane as a result of competitive adsorption with toluene. Experiments with $SF_6$ demonstrted that concentration polarization did not account for the decreased permeances in the presence of toluene.

## 4.6 Acknowledgements

We gratefully acknowledge support by the National Science Foundation, Grant CBET 1263130.

## 4.7 References

[1] T. Wu, M.C. Diaz, Y. Zheng, R. Zhou, H.H. Funke, J.L. Falconer, et al., Influence of propane on $CO_2/CH_4$ and $N_2/CH_4$ separations in CHA zeolite membranes, J. Membr. Sci. 473 (2015) 201–209.

[2] N.O. Chisholm, G.C. Anderson, J.F. McNally, H.H. Funke, R.D. Noble, J.L. Falconer, Increasing $H_2/N_2$ separation selectivity in CHA zeolite membranes by adding a third gas, J. Memb. Sci. 496 (2015) 118–124.

[3] J.C. Poshusta, R.D. Noble, J.L. Falconer, Characterization of SAPO-34 membranes by water adsorption, J. Memb. Sci. 186 (2001) 25–40.

[4] S. Li, G. Alvarado, R.D. Noble, J.L. Falconer, Effects of impurities on $CO_2/CH_4$ separations through SAPO-34 membranes, J. Membr. Sci. 251 (2005) 59–66.

[5] K. Keizer, A.J. Burggraafa, Z.A.E.P. Vroon, H. Verweij, Two component permeation through thin zeolite MFI membranes, J. Memb. Sci. 147 (1998) 159–172.

[6] S. Mokhatab, W.A. Poe, J.Y. Mak, Handbook of Natural Gas Transmission and Processing, 3rd editio, Elsevier, Amsterdam, 2015.

[7] A.M. Avila, H.H. Funke, Y. Zhang, J.L. Falconer, R.D. Noble, Concentration polarization in SAPO-34 membranes at high pressures, J. Membr. Sci. 335 (2009) 32–36.

[8] D.V. Cao, S. Sircar, Heat of Adsorption of Pure Sulfur Hexafluoride on Micro-Mesoporous Adsorbents, in: 2001st ed., Kluwer Academic Publishers, 2001: pp. 73–80.

[9] R. Yoshimoto, K. Hara, K. Okumura, N. Katada, M. Niwa, Analysis of Toluene Adsorption on Na-Form Zeolite with a Temperature-Programmed Desorption Method, (2006).

[10] M.D. LeVan, T. Vermeulen, Binary Langmuir and Freundlich isotherms for ideal adsorbed solutions, J. Phys. Chem. 85 (1981) 3247–3250.

[11] D.W. Hand, S. Loper, M. Ari, J.C. Crittenden, Prediction of Multicomponent Adsorption Equilibria Using Ideal Adsorbed Solution Theory, Environ. Sci. Technol., 1985, 19 (11), 1037–1043.

[12] M. Sakuth, J. Meyer, J. Gmehling, Measurement and prediction of binary adsorption equilibria of vapors on dealuminated Y-zeolites (DAY), Chem. Eng. Process. Process Intensif. 37 (1998) 267–277.

[13] S. Furmaniak, S. Koter, A.P. Terzyk, P.A. Gauden, P. Kowalczyk, G. Rychlicki, New insights into the ideal adsorbed solution theory, Phys. Chem. Chem. Phys. 17 (2015) 7232–7247.

[14] R. Zhou, E.W. Ping, H.H. Funke, J.L. Falconer, R.D. Noble, Improving SAPO-34

membrane synthesis, J. Memb. Sci. 444 (2013) 384–393.

[15] S. Li, J.L. Falconer, R.D. Noble, SAPO-34 membranes for $CO_2/CH_4$ separations: Effect of Si/Al ratio, Micropor. Mesopor. Mater. 110 (2008) 310–317.

[16] M. Salmasi, S. Fatemi, S.J. Hashemi, MTO reaction over SAPO-34 catalysts synthesized by combination of TEAOH and morpholine templates and different silica sources, Sci. Iran. 19 (2012) 1632–1637.

[17] M. Nagao, Y. Suda, Adsorption of benzene, toluene, and chlorobenzene on titanium dioxide, Langmuir. 5 (1989) 42–47.

[18] T. Morimoto, M. Nagao, Y. Suda, Heat of immersion of zinc oxide in organic liquids. 3. Immersion in benzene, toluene, and chlorobenzene, J. Phys. Chem. 89 (1985) 4881–4883.

[19] J. Garcia-Martinez, K. Li, M.E. Davis, Mesoporous zeolites : preparation, characterization and applications, Wiley, 2015.

[20] R. Krishna, L.J.P. van den Broeke, The Maxwell-Stefan description of mass transport across zeolite membranes, Chem. Eng. J. Biochem. Eng. J. 57 (1995) 155–162.

[21] F. Kapteijn, J.A. Moulijn, R. Krishna, The generalized Maxwell–Stefan model for diffusion in zeolites:, Chem. Eng. Sci. 55 (2000) 2923–2930.

[22] A.L. Myers, J.M. Prausnitz, Thermodynamics of mixed-gas adsorption, AIChE J. 11 (1965) 121–127.

[23] E.L. Cussler, Diffusion : Mass transfer in fluid systems, Cambridge University Press, 2009.

[24] H.Y. Erbil, Y. Avci, Simultaneous Determination of Toluene Diffusion Coefficient in Air from Thin Tube Evaporation and Sessile Drop Evaporation on a Solid Surface, Langmuir, 18 (2002) 5113–5119.

[25] L. Mi, S.-T. Hwang, Correlation of concentration polarization and hydrodynamic parameters in hollow fiber modules, J. Memb. Sci. 159 (1999) 143–165.

[26] J.M.S. Henis, M.K. Tripodi, Composite hollow fiber membranes for gas separation: the

resistance model approach, J. Memb. Sci. 8 (1981) 233–246.

[27] E.D. Snijder, M.J.M. Te Riele, G.F. Versteeg, W.P.M. Van Swaaij, Diffusion Coefficients of CO, COS, N20, and N2 in Ethanol and Toluene, J. Chem. Eng. Data. 40 (1996) 37–39.

[28] P. Luhring, A. Schumpe, Gas Solubilities ($H_2$, He, $N_2$, $CO_2$, $O_2$, Ar, CO,) in Organic Liquids at 293.2 K, J. Chem. Eng. Data. 34 (1989) 250–252.

# Chapter 5 Carbon Dioxide and Alkane Separations in a SSZ-13 Membrane

This chapter will be submitted to the Journal of Membrane Science as: N.O. Chisholm, T. Wu, R. Zhou, H.H. Funke, R.D. Noble, J.L. Falconer, Carbon Dioxide and Alkane Separations in a SSZ-13 membrane.

## 5.1 Abstract

Small alkanes decreased $CO_2$ permeance in an SSZ-13 membrane at 690 kPa and 293 K, but not in order of increasing carbon number. Ethane decreased $CO_2$ permeance significantly more (45%) than $CH_4$ (5%), likely because $C_2H_6$ reduced both $CO_2$ loading and diffusivity more. In contrast, $C_3H_8$ and n-$C_4H_{10}$ only decreased $CO_2$ permeances by 10% and 15%, respectively, even though these molecules adsorb in SSZ-13 crystals to high loadings. This unexpected result is attributed to a barrier on the membrane surface that prevented $C_3H_8$ and n-$C_4H_{10}$ adsorption in the membrane. The small decreases in $CO_2$ permeance were apparently due to $C_3H_8$ and n-$C_4H_{10}$ adsorption on the external surface, since i-$C_4H_{10}$ and n-$C_4H_{10}$ caused similar decreases, even though i-$C_4H_{10}$ is too large to diffuse into SSZ-13 pores. After heating the membrane at 323 K overnight in a mixture of $CO_2$ and $C_3H_8$, $CO_2$ permeance at 293 K decreased by 33%, so propane can slowly enter the membrane pores, but not to a significant extent over the timescale (5 h) of the 293 K experiments.

## Introduction

The permeances and separation selectivities of a SSZ-13 membrane were measured for mixtures of $CO_2$ with $C_1$ to $C_4$ alkanes. SSZ-13 membranes have high $CO_2/CH_4$ separation selectivities and are of interest for natural gas purification [1,2], but alkanes larger than $CH_4$ are also present in natural gas and may affect membrane performance. Wu et al. previously showed that SAPO-34 membranes (same CHA crystal structure as SSZ-13 but different chemical composition) are selective for $CO_2/CH_4$ separations [3,4], but adding $C_3H_8$ or n-$C_4H_{10}$ to the feed significantly decreased both permeances and selectivities over several days as the larger hydrocarbons slowly diffused into the zeolite pores [5]. Propane and n-$C_4H_{10}$ were detrimental for membrane performance at both low and high pressures. The permeances recovered when the adsorbed hydrocarbons were removed at elevated temperatures. Since the membranes were more selective at room temperature, large-scale application may not be feasible unless the natural gas has been pretreated to significantly lower the concentrations of these higher alkanes. Similarly, $C_3H_8$ and n-$C_4H_{10}$ decreased permeances and selectivities in SSZ-13 membranes at low pressures. However, at higher pressures, $C_3H_8$ *increased* the $CO_2$ permeance and *increased* the $CO_2/CH_4$ selectivity.

Thus, in the current study, a SSZ-13 zeolite membrane was used to measure how $CO_2$ permeances were affected by the addition of an alkane to the feed at a $CO_2$ pressure of 690 kPa. The effect of the different alkanes on the $CO_2$ permeances, the magnitudes of the alkane permeances, and the $CO_2$/alkane separation selectivities are of interest. The change in the $CO_2$ permeance when an alkane is added to the feed indicates how readily the alkane adsorbs into the SSZ-13 pores. The values of the alkane permeances indicate how much of the overall flux is through defects larger than the zeolite pores since the alkanes primarily permeate through defects

because their diffusion through the zeolite channels is slow. The permeances of the larger alkanes through a membrane with few defects are often too low to be measured directly, but they can determined from the permeate concentration when feeding binary mixtures with a more permeable molecule such as $CO_2$, which acts to carry the alkane to the GC sample injection loop. The kinetic diameters increase from $C_1$ to $C_3$ ($CH_4$ = 0.38 nm; $C_2H_6$ = 0.39 nm; $C_3H_8$ = 0.43 nm), and n-$C_4H_{10}$ has the same kinetic diameter as $C_3H_8$, but i-$C_4H_{10}$ has a kinetic diameter of 0.49 nm.

The overall trend in $CO_2$ permeance with increasing alkane size was unexpected. $C_2H_6$ decreased the $CO_2$ permeance more than $CH_4$, as expected, because $C_2H_6$ adsorbs more strongly than $CH_4$; however, $C_3H_8$ and n-$C_4H_{10}$ decreased the $CO_2$ permeance less than $C_2H_6$ did, even though both $C_3H_8$ and n-$C_4H_{10}$ have higher equilibrium loadings in SSZ-13. Moreover, when i-$C_4H_{10}$ was added to the $CO_2$ feed, it decreased the $CO_2$ permeance about the same as n-$C_4H_{10}$, even though i-$C_4H_{10}$ is too large to adsorb in the SSZ-13 pores. This suggests that even though both $C_3H_8$ and n-$C_4H_{10}$ adsorb in SSZ-13 crystal samples to high loadings [6], they apparently do not adsorb in the SSZ-13 pores in this membrane on the time scale of the measurements. One possible explanation for this behavior is a diffusion barrier on the external surface of the crystals in the membrane that may not be present in crystals powders.

This decrease in $CO_2$ permeance caused by $C_3H_8$ and n-$C_4H_{10}$ is attributed to adsorption on the external surface of the zeolite crystals, and as a result, i-$C_4H_{10}$ and n-$C_4H_{10}$ had similar effects on the $CO_2$ permeance. External adsorption of toluene on SAPO-34 has been shown to similarly decrease $CO_2$ and $N_2$ permeances by competitive adsorption for surface sites in SAPO-34 membranes [7].

.

## 5.2 Experimental Methods

### 5.2.1 SSZ-13 crystal synthesis and characterization

Seed crystals for membrane synthesis were prepared by mixing deionized water, NaOH, and $Al(OH)_3$ at room temperature for 1 h. Then N,N,N trimethyl-1-adamantammonium hydroxide (TMAdaOH) was added over 15 min, and the solution was stirred another 1 h at room temperature. Colloidal silica was finally added and the mixture was stirred overnight. The gel molar ratios were 1.0 $SiO_2$: 0.10 $Na_2O$: 0.025 $Al_2O_3$: 0.40 TMAdaOH: 44 $H_2O$. The gel was heated to 433 K and held at that temperature for 96 h in a Teflon-lined autoclave. The resulting crystals were collected by centrifugation, washed three time with DI water, dried overnight at 373 K, and calcined in air at 823 K for 10 h to remove the template.

### 5.2.2 SSZ-13 membrane preparation and characterization

The SSZ-13 membrane synthesis was described by Wu el al. [5]. The membrane support, a porous mullite tube (NIKKATO, 12-mm O.D., 1.3-μm pore size), was polished (on its outer surface) with 800# sandpaper, washed in boiling DI water for 30 min, and then dried at 373 K overnight. Seed crystals were deposited on the outside of the support by rub-coating with a 10% seed crystal/water slurry. The support was capped with Teflon plugs to prevent SSZ-13 deposition on the inside and then placed into an autoclave that contained synthesis gel. The gel was prepared with the same chemicals used to make the seed gel, but tetraethylammonium hydroxide (TEAOH) was also added to the synthesis gel. The chemicals were combined in DI water, and the mixture was stirred for 48 h at 333 K. The gel molar ratios were 1.0 $SiO_2$: 0.1 $Na_2O$: 0.025 $Al_2O_3$: 0.05 TMAdaOH: 0.05 TEAOH: 80 $H_2O$.

The zeolite membrane layer was grown by heating the seeded support in the gel to 443 K for 48 h. After synthesis, the membrane was washed with tap water for 15 min, soaked in DI water

overnight, and then dried at 373 K overnight. The template was removed by heating the membrane in air to 753 K for 6 h, with heating and cooling rates of 0.5 K/min, and the membrane was stored at 373 K.

XRD (Scintag PAD-V XRD instrument with Cu Kα radiation) confirmed the SSZ-13 structure on the membrane surface and on powders collected from the autoclave after membrane synthesis. SEM images showed a 10-μm thick zeolite film on the outside of the support, and SSZ-13 crystals likely also grew into the large pores of the mullite support.

### 5.2.3 Permeation and separation measurements

The membrane was mounted in a stainless steel module using two Viton O-rings on each end. Because the membrane layer is on the outside of the tubular support, the ends of the membrane were not glazed, and the o-rings sealed directly on the zeolite layer. A small amount of vacuum grease was applied to the o-rings to improve the seal. The outside of the membrane was pressurized in small increments with $CO_2$ to determine the maximum feed pressure that could be achieved without leaking under the O-ring seals. Leaks were indicated by an increase in permeance. All subsequent measurements were carried out at pressures significantly below where leaks were first observed (1 MPa).

In a typical experiment, the membrane module and a 3A-zeolite trap (to remove moisture) upstream of the membrane module were heated overnight at 323 K, and then cooled to room temperature in flowing $CO_2$. The $CO_2$ permeance was then measured at a feed pressure of 690 kPa, which was controlled with a manual back-pressure regulator and measured with electronic transducers. Methane and $C_2H_6$ were added directly to the $CO_2$ feed with a second flow controller to obtain binary mixtures, whereas $CO_2$/ $C_3H_8$ and $CO_2$/$C_4H_{10}$ mixtures were fed from mixed gas cylinders because the feed pressure exceeded the vapor pressure of the individual hydrocarbon

components. In all cases, when 15% alkane was added to the feed, the total feed pressure was increased to 807 kPa to maintain a $CO_2$ partial pressure of 690 kPa. Retentate and permeate compositions were measured by a GC equipped with both TCD and FID detectors and a Hayesep D column. The retentate and permeate flow rates were measured with soap-film flow meters, which were also used to calibrate the mass flow controllers. A log-mean driving force was used to calculate permeances. The separation selectivities were the ratio of permeances. The larger alkanes had permeate concentrations close to the detection limit of the GC, and thus the accuracies of those alkane permeances and $CO_2$/alkane selectivities were low.

## 5.3 Results and discussion

### 5.3.1 Carbon dioxide/alkane separation selectivities

The $CO_2$/alkane separation selectivity is affected by how strongly an alkane absorbs in the zeolite pores since alkane adsorption decreases the $CO_2$ permeance; a larger alkane is expected to adsorb more strongly and lower the $CO_2$ permeance more than smaller alkanes, and thus a lower selectivity is expected. The selectivity is also affected by how fast an alkane diffuses, and a larger alkane diffuses more slowly in zeolite pores, and this should increase selectivity. As shown in Table 5.1, adsorption appears to be more important for $CH_4$ and $C_2H_6$ since the $CO_2/CH_4$ selectivity is higher than the $CO_2/C_2H_6$ selectivity, even though the $C_2H_6$ permeance is significantly lower than the $CH_4$ permeance. In contrast, the $CO_2$/alkane selectivities for $C_3$ and $C_4$ alkanes are 2 orders of magnitude higher; the alkane permeances were almost two orders of magnitude lower for $C_3$ and $C_4$ alkanes. Because the alkane concentrations in the permeate stream were close to the noise level, they are not accurate; the $C_3$ and $C_4$ permeances should be considered maximum estimates, and the $CO_2$/alkane selectivities for $C_3$ and $C_4$ should be considered minimum values.

The decrease in alkane permeance by a factor of 65 going from $C_2$ to $C_3$ indicates that the number of defects larger than 0.43 nm is small. Essentially all of the $C_3$ and $C_4$ alkane permeances are through defects since $C_3H_8$ and i-$C_4H_{10}$ have similar permeances, and i-$C_4H_{10}$ is much too large to fit into the SSZ-13 pores. This means the percent of the total $CO_2$ flow through defects is probably less than 0.1%, and thus these membranes are of high quality.

**Table 5.1.** $CO_2$/alkane separations in SSZ-13 membrane at 293 K (the $CO_2$ feed pressure was 690 kPa)

| % Alkane in Feed | Alkane Kinetic Diameter (nm) | $CO_2$/Alkane Selectivity | Alkane Permeance x$10^{12}$ (mol/$m^2$ s Pa) |
|---|---|---|---|
| 15.4% $CH_4$ | 0.38 | 177 | 630 |
| 50.8% $CH_4$ | 0.38 | 157 | 510 |
| 15.7% $C_2H_6$ | 0.39 | 167 | 370 |
| 50.1% $C_2H_6$ | 0.39 | 82 | 300 |
| 15.1% $C_3H_8$ | 0.43 | 1.7x$10^4$ | 5.7 |
| 15.1% $C_3H_8$* | 0.43 | 2.1x $10^4$ | 3.1 |
| 15.0% n-$C_4H_{10}$ | 0.43 | 2.8x $10^4$ | 3.4 |
| 15.4% i-$C_4H_{10}$ | 0.49 | 2.5x $10^4$ | 3.4 |

*adsorbed overnight at 323 K

### 5.3.2 Alkane effect on $CO_2$ permeance

Adding 15% $CH_4$ to the $CO_2$ feed only decreased the $CO_2$ permeance by about 5%, as might be expected since $CH_4$ adsorbs more weekly than $CO_2$ on SSZ-13 zeolite [6]. Interestingly, adding 50% $CH_4$ to the $CO_2$ feed decreased the $CO_2$ permeance by 30% (Table 5.2). Apparently when enough $CH_4$ absorbs in the SSZ-13 pores, $CO_2$ diffusion is hindered more, in addition to $CO_2$ loading being lower. Adding 15% $C_2H_6$ to the feed decreased the $CO_2$ permeance by 45%. Ethane decreased the $CO_2$ permeance more than $CH_4$ because $C_2H_6$ both adsorbs more strongly

(and thus reduces $CO_2$ loading more), and is larger and diffuses more slowly through the SSZ-13 pores, which could lower $CO_2$ diffusivity. Similarly, adding 50% $C_2H_6$ decreased the $CO_2$ permeance by 79%.

**Table 5.2.** Decrease in $CO_2$ permeance in SSZ-13 membrane after alkanes were added at 293 K (the $CO_2$ feed pressure was 690 kPa)

| % Alkane in Feed | Alkane Kinetic Diameter (nm) | Percent Decrease in $CO_2$ Permeance |
|---|---|---|
| 15.4% $CH_4$ | 0.38 | 5.4 |
| 50.8% $CH_4$ | 0.38 | 30 |
| 15.7% $C_2H_6$ | 0.39 | 45 |
| 50.1% $C_2H_6$ | 0.39 | 79 |
| 15.1% $C_3H_8$ | 0.43 | 10 |
| 15.1% $C_3H_8$* | 0.43 | 33 |
| 15.0% n-$C_4H_{10}$ | 0.43 | 15 |
| 15.0% n-$C_4H_{10}$** | 0.43 | 28 |
| 15.4% i-$C_4H_{10}$ | 0.49 | 15 |

*membrane held in 15% $C_3H_8$ overnight at 323 K
**membrane held in pure n-$C_4H_{10}$ overnight at 293 K

Although 15% C2H6 decreased the $CO_2$ permeance by 45%, 15% $C_3H_8$ only decreased the $CO_2$ permeance by 10%. This is unexpected since adsorption isotherms [6] show $C_3H_8$ has a significantly higher loading than $C_2H_6$ in SSZ-13, and $C_3H_8$ diffuses dramatically slower than $C_2H_6$ [7]. Indeed, if the results for $C_1$ and $C_2$ in Figure 1 were extrapolated, $C_3H_8$ would be expected to decrease the $CO_2$ permeance by 70 or 80%, and n-$C_4H_{10}$ would be expected to decrease the $CO_2$ permeance even more. n-Butane decreased the $CO_2$ permeance more than $C_3H_8$, but much less than $C_2H_6$.

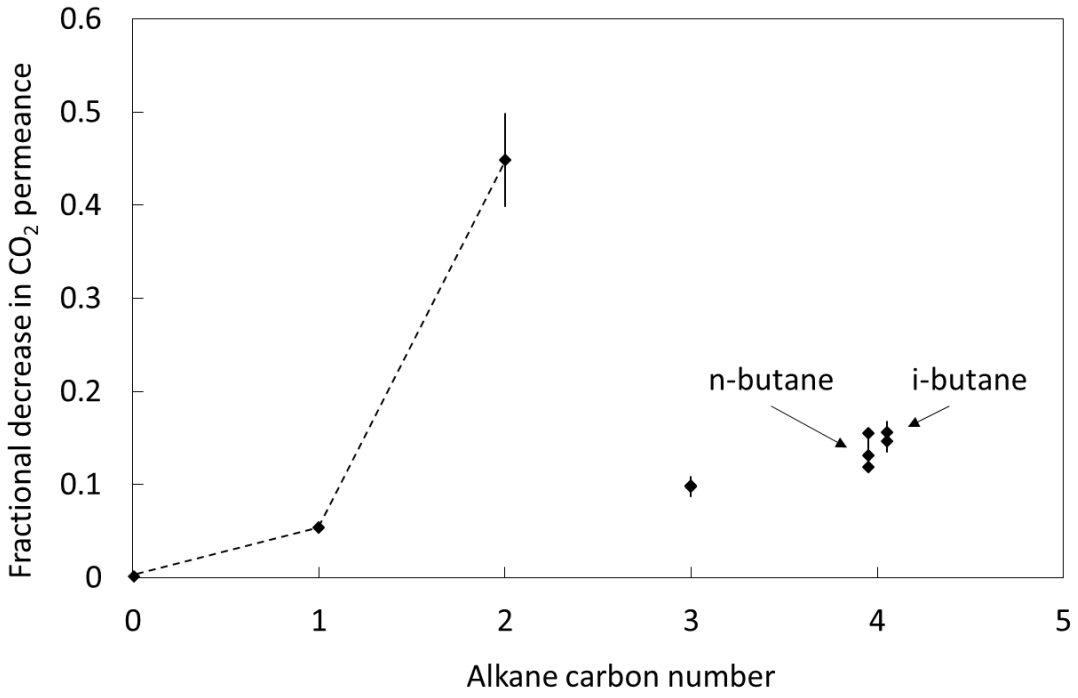


**Figure 5.1.** Percent decrease in $CO_2$ permeance through SSZ-13 membrane after 15% alkane was added to the feed at 293 K and constant $CO_2$ partial pressure of 690 kPa versus alkane carbon number. Vertical lines are error estimates based on several measurements for n-$C_4H_{10}$ (+/- 1 standard deviation).

For the $CO_2$/alkanes measurements, the $CO_2$ permeance decreased within at most 15 min. Measurements were not made at shorter times because the pressure was increased when alkane was added to the feed, and the system pressure and flow rate took about 10 min to stabilize. After about 10 min, the $CO_2$ permeances did not change appreciably for about 5 h. Over longer times, $C_3H_8$ and n-$C_4H_{10}$ could accumulate in the SSZ-13 pores and decrease permeances more than $C_2H_6$, but the permeances were stable over the course of these experiments. Each point in Figure 5.1 is an average of three or more readings taken over several hours; the multiple points for a given alkane represent measurements made on different days and the error bars show that variation.

These unexpected results lead us to conclude that $C_3H_8$ and n-$C_4H_{10}$ did not adsorb in the SSZ-13 membrane pores under these conditions, even though they adsorb in the pores of SSZ-13

crystals at the same temperature and even lower pressures. Instead, $CO_2$ permeances decrease when $C_3H_8$ and $C_4H_{10}$ were added to the $CO_2$ feed because alkanes adsorb on the external surface of the SSZ-13 crystals. This is why n-$C_4H_{10}$ and i-$C_4H_{10}$ decreased the $CO_2$ permeance by the same percent; i-$C_4H_{10}$ is significantly larger than the SSZ-13 pores [8] and can only affect the $CO_2$ permeance by adsorbing on the external surface of SSZ-13 crystals.

Recently we showed that toluene, which is much larger than SAPO-34 pores, can significantly reduce $CO_2$ permeation through SAPO-34 membranes because it adsorbs on the external membrane surface [7]. When 0.65 mol% toluene was added to $CO_2$ at 172-kPa feed pressure, the permeance decreased by about 45%. Permeances were measured for several toluene concentrations, and binary adsorption models for $CO_2$ and toluene were used to calculate changes in $CO_2$ surface coverages. Toluene decreased $CO_2$ permeances approximately in proportion to the lower $CO_2$ concentration on the external membrane surface, which decreased the driving force.

### 5.3.3 Effect of pressure on $CO_2$/propane separations

Propane (15%) reduced the $CO_2$ permeance more at higher $CO_2$ pressure, where $CO_2$ coverages are higher and competitive adsorption with $C_3H_8$ reduces $CO_2$ loading by a greater fraction (table 3). At lower pressure and lower loading there are more empty adsorption sites for the added $C_3H_8$ to occupy so it does not reduce $CO_2$ loading as much. The effect is also expected for internal adsorption, but the effect of $C_3H_8$ was likely due mostly to external adsorption.

**Table 5.3.** Decrease in $CO_2$ permeance in SSZ-13 membrane after 15% propane was added at 293 K for different $CO_2$ pressures

| Pure $CO_2$ Feed Pressure | $CO_2$ Pressure with Propane* | Percent decrease in $CO_2$ permeance |
|---|---|---|
| 201 | 183 | 11 |
| 101 | 96 | 9.8 |
| 49 | 49 | 6.5 |

*Log-mean partial pressure between feed and retentate

### 5.3.4 Carbon dioxide, methane, and propane

When $C_3H_8$ was added to an equimolar feed of $CO_2$ and $CH_4$ at constant $CO_2$ feed pressure of 690 kPa, the $CO_2$ permeances decreased by 1.1% and the $CH_4$ permeance decreased by 3.6% so that the $CO_2/CH_4$ selectivity increased slightly. When $C_3H_8$ was added to just $CO_2$ at the same partial pressure, the $CO_2$ permeance decreased by 9.7%. Because $CO_2$ adsorbs more strongly than $CH_4$ , the $C_3H_8$ likely preferentially displaced $CH_4$, which is why $CH_4$ permeance decreased more. The presence of $CH_4$ in the feed had already reduced the $CO_2$ permeance from about $1.1x10^{-7}$ to $8x10^{-8}$ mol/($m^2$ Pa s) and the decrease from pure $CO_2$ to $CO_2/CH_4/C_3H_6$ (28% decrease) was about the same as the decrease from pure $CO_2$ to $CO_2/CH_4$ (30% from Table 5.2), and it was more than from pure $CO_2$ to $CO_2/C_3H_{10}$ (9.7%). When both $CH_4$ and $C_3H_8$ were added to $CO_2$, the $CO_2$ permeance decreased because $CH_4$ reduced $CO_2$ loading, $CH_4$ reduced $CO_2$ diffusivity, and $C_3H_8$ reduced $CO_2$ coverage on the external surface. However, $C_3H_8$ also reduced the $CH_4$ coverage on the external surface so that less $CH_4$ adsorbed in the SSZ-13 pores. Propane is expected to have negligible loading in the SSZ-13 pores, based on the results in Table 5.1. The slightly smaller decrease in $CO_2$ permeance when both $C_3H_8$ and $CH_4$ are in the feed is within experimental error, but $C_3H_8$ may reduce $CH_4$ loading enough that the $CO_2$ diffusivity is higher in the three-gas system

than in the $CO_2/CH_4$ system; this would counteract the lower permeance due to lower $CO_2$ coverage on the external surface.

### 5.3.5 Propane adsorption at elevated temperature

The permeation measurements indicate that $C_3H_8$ and n-$C_4H_{10}$ do not adsorb into the SSZ-13 pores of the membrane on the timescale of the measurements. However, adsorption isotherms measured on SSZ-13 crystals clearly show that these alkanes adsorb into SSZ-13 pores [6]. A likely explanation for this difference is that the external pores of the SSZ-13 crystals in the membrane are slightly distorted so that the $C_3H_8$ and n-$C_4H_{10}$ cannot easily fit. Since the kinetic diameter of $C_3$ and n-$C_4$ alkanes is 0.43 nm, and the pore diameter of SSZ-13 is 0.38 nm, these alkanes have to wiggle to fit into the SSZ-13 pores. Thus, only a slight change in the external pore opening cross-section or aspect ratio could have a significant effect on adsorption of these alkanes [10,11].

The membrane was exposed to a 15% $C_3H_8$/85% $CO_2$ mixture at 323 K overnight in an effort to adsorb $C_3H_8$ into the SSZ-13 pores. When the membrane was then cooled to room temperature, its $CO_2$ permeance was 33% lower than the pure $CO_2$ permeance (compared to only 10% decrease without heating). That is, $C_3H_8$ apparently absorbed in the SSZ-13 pores in the membrane at 323 K overnight, whereas it did not adsorb at a significant rate at room temperature. When the $C_3H_8$ was removed from the feed side of the membrane after the permeation measurements, the $CO_2$ permeance increased, but it was still 20% below the pure $CO_2$ permeance, even after 26 h. This increase in the $CO_2$ permeance is attributed to $C_3H_8$ desorption from the external surface of the SSZ-13 pores. The $C_3H_8$ that adsorbed in the SSZ-13 pores at 323 K, however, did not readily desorb at room temperature. When the membrane was heated to 323 K overnight with a $CO_2$ feed, the $CO_2$ permeance at room temperature was higher, and when the

membrane was further heated for an additional overnight period, the $CO_2$ permeance at room temperature was about equal to the original $CO_2$ permeance. Heating to 323 K increases $C_3H_8$ diffusion and also decreases the equilibrium loading of $C_3H_8$. Thus, although heating the membrane increased $C_3H_8$ loading, the equilibrium, room-temperature loading is expected to be significantly higher than that achieved in this experiment. Equilibrium $C_3H_8$ loading at room-temperature is expected to reduce $CO_2$ permeance significantly more than $C_2H_6$ did.

### 5.3.6 Surface diffusion barrier

A number of researchers have observed differences in adsorption and diffusion behavior that were attributed to diffusion barriers on the external surface of crystals [12-21]. For example, Wloch increased the rate of n-hexane diffusion into ZSM-5 crystals by two orders of magnitude by using low concentrations of HF to etch away a thin layer of the zeolite external surface [20], and Kortunov et al. showed that i-$C_4H_{10}$ desorbed faster from ZSM-5 after etching the crystals in HF [21]. Repeatedly adsorbing and desorbing i-$C_4H_{10}$ increased the surface barrier, and Kortunov et al. attributed this to immobilized adsorbate molecules on the surface. Similarly, the external surface of our SSZ-13 membrane may have changed during exposures to a variety of gases over the course of numerous experiments.

Kalantzopoulos et al. found that replacing silanols on the surface of silicalite-1 with silanes increased $H_2$ diffusivity [16]. The initial, lower diffusivity was attributed to a higher potential energy barrier for surface diffusion into the pores near the surface and/or a physical obstruction of the pores by immobilized $H_2O$ molecules. Water or organics may have adsorbed and bonded strongly to the surface of our SSZ-13 membrane during years of storage.

Alternatively, the membrane surface structure may have been affected by termination of crystal growth during synthesis. The external surfaces may be different for the SSZ-13 crystals

used for adsorption measurements and the membranes because the crystals were made with one structure-directing agent (TMAdaOH), but the membrane synthesis gel used an additional structure-directing agent (TEAOH). In any case, the pore structure of the membrane external surface could 1) have pores with less than 0.38-nm cross section, or some other distortion, 2) otherwise have some steric blocking of the bent molecules $C_3H_8$ and n-$C_4H_{10}$ (for example short channels <0.43-nm diameter), and/or 3) a surface chemistry that adds a significant energy barrier for $C_3H_8$ and n-$C_4H_{10}$ diffusion from the surface to inside the pore.

Karger et al. measured self-diffusion of $CH_4$ and Xe in NaX, NaCaA, and ZSM-5 and found surface barriers to Xe diffusion in the NaCaA and ZSM-5, but no surface barriers to $CH_4$ in any of the zeolites. They concluded that the probe molecule affects the observed barrier; a surface barrier may have negligible effect on diffusion of small molecules into zeolite while large molecules are significantly slowed. In our SSZ-13 membrane, the external surface may have a structure that prevents $C_3H_8$ and n-$C_4H_{10}$ diffusion but allows appreciable $CH_4$ and $C_2H_6$ diffusion.

We propose that the difference between SSZ-13 crystals prepared homogenously and those in the membrane is subtle; the external surface opening is only slightly different. Computer simulations with hard-sphere ballistic collision models [10] and molecular dynamics simulations [11] have showed that small changes in pore size can change diffusivities by orders of magnitude if the sizes of the diffusing molecules are close to size of the pore openings, which $C_3H_8$ and n-$C_4H_{10}$ certainly are. Our results indicate that adsorption measurements on zeolite crystals may not always be a reliable indicator of how the same molecule adsorbs in membrane crystals.

## 5.4 Conclusions

- SSZ-13 membranes can effectively separate $CO_2/CH_4$ mixtures even in the presence of $C_3H_8$.
- $C_1$ to $C_4$ alkanes reduce $CO_2$ permeance in SSZ-13 membranes but not in order of increasing carbon number – $C_2H_6$ has a much greater effect than $C_3H_8$ and n-$C_4H_{10}$.
- $CO_2/C_3H_8$ selectivities greater than $10^4$ were measured on SSZ-13 membranes, indicating low defect fluxes – less than 0.1% of the $CO_2$ permeation through defects.
- Molecules that are too large to fit into zeolite crystals can significantly affect permeation behavior through zeolite membranes by adsorbing on the external surfaces of the crystals.
- $C_3$ to $C_4$ alkanes permeate almost exclusively through membrane defects.
- Slight changes in the external surface of zeolite crystals can significantly affect adsorption and permeation of molecules that are similar in size to the zeolite pores.
- Adsorption measurements on zeolite crystals may not be a reliable measure of how zeolite crystals behave in a membrane.

## 5.5 Acknowledgements

We gratefully acknowledge support by the National Science Foundation, Grant CBET 1263130 and thank Ting Wu and Rongfei Zhou for supplying the SSZ-13 membrane.

## 5.6 References

[1] Y. Zheng, N. Hu, H. Wang, N. Bu, F. Zhang, R. Zhou, Preparation of steam-stable high-silica CHA (SSZ-13) membranes for $CO_2/CH_4$ and $C_2H_4/C_2H_6$ separation, J. Memb. Sci. 475 (2015) 303–310.

[2] N. Kosinov, C. Auffret, G.J. Borghuis, V.G.P. Sripathi, E.J.M. Hensen, Influence of the Si/Al ratio on the separation properties of SSZ-13 zeolite membranes, J. Memb. Sci. 484

(2015) 140–145.

[3] M.A. Carreon, S. Li, J.L. Falconer, R.D. Noble, Alumina-Supported SAPO-34 Membranes for $CO_2/CH_4$ Separation, J. Am. Chem. Soc. 130 (2008) 5412–5413.

[4] R. Zhou, E.W. Ping, H.H. Funke, J.L. Falconer, R.D. Noble, Improving SAPO-34 membrane synthesis, J. Memb. Sci. 444 (2013) 384–393.

[5] T. Wu, M.C. Diaz, Y. Zheng, R. Zhou, H.H. Funke, J.L. Falconer, et al., Influence of propane on $CO_2/CH_4$ and $N_2/CH_4$ separations in CHA zeolite membranes, J. Membr. Sci. 473 (2015) 201–209.

[6] Y. Luo, H.H. Funke, J.L. Falconer, R.D. Noble, Adsorption of $CO_2$, $CH_4$, $C_3H_8$, and $H_2O$ in SSZ-13, SAPO-34, and T‑Type Zeolites, Ind. Eng. Chem. Res. 55 (2016) 9749–9757.

[7] N. Chisholm, H. Funke, R. Noble, J. Falconer, Effect of toluene on $CO_2$ and $N_2$ permeance in SAPO-34 membranes, in prep.

[8] D.H. Olson, Light hydrocarbon separation using 8-member ring zeolites, US6488741 B2, 2001.

[9] H.H. Funke, M.Z. Chen, A.N. Prakash, J.L. Falconer, R.D. Noble, Separating molecules by size in SAPO-34 membranes, J. Memb. Sci. 456 (2014) 185–191.

[10] D.M. Ford, E.D. Glandt, Steric hindrance at the entrances to small pores, J. Memb. Sci. 107 (1995) 47–57.

[11] D.M. Ford, E.D. Glandt, Molecular Simulation Study of the Surface Barrier Effect. Dilute Gas Limit, J. Phys. Chem. 99 (1995) 11543–11549.

[12] D.A. Newsome, D.S. Sholl, Influences of Interfacial Resistances on Gas Transport through Carbon Nanotube Membranes, NANO Lett. 6 (2006) 2150–2153.

[13] P. Grenier, F. Meunier, P.G. Gray, Diffusion of methanol in NaX crystals: Comparison of i.r., ZLC, and PFG-n.m.r. measurements, Zeolites. 14 (1994) 242–249.

[14] J. Kärger, M. Hunger, H. Freude, H. Pfeifer, J. Caro, M. Bulow, et al., NMR investigations

on molecular transport in ZSM-5 type zeolites containing structural defects, Catal. Today. 3 (1988) 493–499.

[15] J. Karger, H. Pfeifer, F. Stallmach, H. Spindler, 129Xe n.m.r. self-diffusion measurements - a novel method to probe diffusional barriers on the external surface of zeolite crystallites, Zeolites. 10 (1990) 288–292.

[16] G.N. Kalantzopoulos, A. Policicchio, E. Maccallini, I. Krkljus, F. Ciuchi, M. Hirscher, et al., Resistance to the transport of H2 through the external surface of as-made and modified silicalite-1 (MFI), Microporous Mesoporous Mater. 220 (2016) 290–297.

[17] J. Kärger, Measurement of Diffusion in Zeolites—A Never Ending Challenge?, Adsorption. 9 (2003) 29–35.

[18] F. Vigne´-Maeder, S. El Amrani, P. Ge´lin, An approach to the surface barrier concept in diffusion in zeolites by computer simulation, J. Catal. 134 (1992) 536–541.

[19] A.R. Teixeira, C.-C. Chang, T. Coogan, R. Kendall, W. Fan, P.J. Dauenhauer, Dominance of Surface Barriers in Molecular Transport through Silicalite-1, J. Phys. Chem. C. 117 (2013) 25545–25555.

[20] J. Wloch, Effect of surface etching of ZSM-5 zeolite crystals on the rate of n-hexane sorption, Microporous Mesoporous Mater. 62 (2003) 81–86.

[21] P. Kortunov, S. Vasenkov, C. Chmelik, J. Kärger, D.M. Ruthven, J. Wloch, Influence of Defects on the External Crystal Surface on Molecular Uptake into MFI-Type Zeolites, Chem. Mater. 16 (2004) 3552–3558.

# Chapter 6 Conclusions and Recommendations

## 6.1 Conclusions

We studied the effects of small alkanes on $H_2/N_2$ separations in SAPO-34 zeolite membranes by adding ethane, propane, and n-butane to an equimolar feed of $H_2$ and $N_2$. Propane reduced the permeance of both gases by reducing their loadings and diffusivities, but it reduced the $H_2$ permeance less than the $N_2$ permeances so that the $H_2/N_2$ selectivity increased from about 4 to about 9. The effect was less at higher temperatures because loadings of all gases decreased, and thus both $H_2$ and $N_2$ permeances decreased. At 398 K, propane reduced permeances slightly but did not change $H_2/N_2$ selectivity. Propane increased the selectivity more at higher total pressure because loadings of all gases were higher. n-Butane had a similar effect as propane and increased $H_2/N_2$ selectivity, but ethane reduced permeances with no significant change in selectivity. The decreases in $H_2$ and $N_2$ permeances stabilize over 2 d because propane and n-butane diffuse slowly in SAPO-34 pores.

Because $N_2$ has a higher heat of adsorption than $H_2$, competitive adsorption with propane and n-butane decreases $H_2$ loading more than $N_2$ loading. This should decrease $H_2$ flux through the membrane more than $N_2$ flux if adsorption is the main factor that determines transport. However, the $N_2$ permeances decreased more, indicating that $N_2$ diffusivity decreased more than $H_2$ diffusivity, so that diffusivity changes result in higher selectivities in the presence of propane and n-butane. Hydrogen (0.29 nm) is smaller than $N_2$ (0.36 nm) and thus steric hindrance by adsorbed, slowly-diffusing alkanes should affect $H_2$ diffusivity less than $N_2$ diffusivity. Ethane may be too small to significantly reduce diffusivities of the smaller gases. This project showed that

in some cases, adding a third gas in small concentrations to a feed mixture can improve overall microporous membrane separation performance if selectivity is more important than permeance.

We also studied how toluene adsorption on the external surface of SAPO-34 affects $CO_2$ and $N_2$ permeances through SAPO-34 membranes. Toluene, which has a kinetic diameter of 0.59 nm, is too large to fit in SAPO-34 pores (0.38 nm), but it adsorbs on the zeolite external surface. When 0.65 mol% toluene was added to feeds of pure $CO_2$ and pure $N_2$ at 293 K, the $CO_2$ permeance decreased by 45% and the $N_2$ permeance decreased by 50%. The feed pressure was 172 kPa, and the permeate pressure was 82 kPa. At 10-kPa feed pressure and 2-kPa permeate pressure, 8.5% toluene decreased $CO_2$ permeances by 20%. A Langmuir isotherm was used to model binary adsorption at the higher pressure, but the fit for the single-component toluene adsorption isotherm was poor, and extrapolation of the model to the experimental $CO_2$ pressure was required. The Langmuir approach is also not thermodynamically consistent, but it can be used when adsorption data are limited. The ideal adsorbed solution theory (IAST), however, is thermodynamically-consistent for ideal adsorbed mixtures and therefore was used to predict binary adsorption at lower pressure, where measured adsorption isotherm data are available. Both approaches predicted that competitive adsorption between toluene and $CO_2$ reduces the $CO_2$ surface coverage, and thus the driving force for $CO_2$ transport. However, the IAST over-predicted the decrease in $CO_2$ permeance (30% instead of the measured 20% at 10-kPa feed pressure with 8.5% toluene in the feed), likely because of non-ideal adsorption on the membrane surface. Since both models accounted for a large fraction of the observed changes in permeance, the thermodynamic effect of competitive adsorption equilibrium is likely the main reason for the observed changes. Thus, even impurities that are too large to adsorb in the zeolite pores have to be considered when designing membrane

systems because they can competitively adsorb on the external membrane surface and reduce permeances.

Finally, we measured the effect of $C_1$ - $C_4$ alkanes on $CO_2$ permeance through SSZ-13 membranes. Propane and n-butane have kinetic diameters of 0.43 nm, which is larger than the 0.38-nm SSZ-13 pores, but they adsorb at high loadings in SSZ-13 crystals because they are flexible and their smallest cross section is smaller than the zeolite pores, even though their kinetic diameter is larger. When 15% methane was added to a $CO_2$ feed, the $CO_2$ permeance decreased by about 5%. Ethane reduced $CO_2$ permeances by 45% at the same concentration because it adsorbs more strongly than $CH_4$, and it reduced both $CO_2$ loading and $CO_2$ diffusivity more than $CH_4$ did. Propane and n-butane should decrease $CO_2$ permeance even more for the same reasons, but 15% propane in the feed only decreased $CO_2$ permeance by 10%, and n-butane only decreased $CO_2$ permeances by 15%. The other $C_4$ alkane isomer, i-butane (kinetic diameter of 0.49 nm), is too large to diffuse through SSZ-13 pores, and it decreased $CO_2$ permeances by 15%, similar to n-butane. Apparently, propane and n-butane did not adsorb into the SSZ-13 pores, and the reduced $CO_2$ permeances were due to external competitive adsorption, as was observed for toluene in SAPO-34 membranes. These results are not expected, based on the adsorption behavior of the crystals, and suggest that the external pore structure of the membrane is different from that of the powders used for measuring the isotherms. We suspect that a layer with different porosity grew on the external membrane surface during synthesis or during storage, and this layer prevented propane and n-butane from entering the zeolite pores to a significant extent, at least for the duration of the permeation measurement of about 5 h. When the membrane was exposed to 15% propane/85% $CO_2$ at 323 K overnight, and then cooled to 273 K with the same feed composition, the $CO_2$ permeance was 33% lower than that of pure $CO_2$, indicating that propane can diffuse into

the SSZ-13 pores at elevated temperature. Given enough time for diffusion to reach steady-state loadings, propane and n-butane should reduce $CO_2$ loadings more than ethane. The SSZ-13 membrane used for this study had a $CO_2$/i-butane selectivity of more than 25,000, and thus essentially all the $CO_2$ flux was through the zeolite pores.

These results indicate that the properties of zeolite powders may not necessarily reflect the properties of a zeolite membrane with the same crystal structure because of subtle differences in the surface porosity. Also, small alkanes can negatively affect $CO_2$ permeances through chabazite membranes, depending on their size and the specific properties of the membrane, and thus they may have to be removed from the feed for stable membrane performance.

## 6.2 Recommendations

The addition of a third component to binary feed mixtures might also increase separation selectivities of zeolite membranes for other systems and thus would be of interest for potential applications. The effect of propane on other separations in SAPO-34, such as $H_2/CO_2$ and $H_2/C_2H_6$, could be of interest since cost-effective $H_2$ purification for applications such as fuel cells is still challenging. The effect of ion-exchanged SAPO-34 or SSZ-13 could be studied, wherein $H^+$ is replaced by larger $K^+$ or $Ca^{2+}$ to reduce cage volume and increase steric hindrance, which could further improve selectivity for $H_2$ (or He) over larger molecules by reducing their diffusivities. Molecular dynamics simulations could potentially confirm that propane and n-butane sterically hinder $N_2$ movement more than $H_2$ in SAPO-34 pores and cause corresponding changes in diffusivity.

The effects of external adsorption of several compounds on $CO_2$ permeance through SAPO-34 could be studied to determine if higher heat of adsorption of the impurity or larger molecular size correlates with lower $CO_2$ permeance as competitive adsorption reduces $CO_2$

coverage more. Molecules like i-butane and $SF_6$ with lower heats of adsorption could be compared to strongly-adsorbing organics with room-temperature vapor pressures between about 1 and 10 kPa. The effect of toluene (or other components) on $CO_2$ separation selectivity with $H_2$, $N_2$ or $CH_4$ could also be studied. Toluene would possibly reduce the surface coverages of those species more than $CO_2$ and improve the membrane selectivity for $CO_2$. The effect of toluene on permeances of small gases through other small-pore zeolites could also be studied. Perhaps toluene adsorption would have less effect on the more hydrophobic SSZ-13. Screening by single-component $CO_2$ and toluene adsorption isotherms on different zeolites could indicate which zeolites would be affected by externally-adsorbing molecules.

The experiments with $CO_2$ and small alkanes in SSZ-13 (chapter 5) did not explain what on the membrane surface prevents diffusion of propane and n-butane into the zeolite pores. A first step to confirm the existence of a surface barrier would be to try to etch away the outer layer of the membrane to see if propane and n-butane diffusion into the membrane increases. The next step would be to recreate the selective surface barrier in some membranes but not in others. The surface barrier could be due to an amorphous silicoaluminophosphate region, or an external deposition from synthesis precursor (or even some compound in the lab atmosphere), so reproducing the surface structure may be quite difficult. Analysis of the surface composition with EDX could show whether an organic component is present. High-resolution TEM of surface samples could give an idea of the surface structure. Neither of those techniques may be conclusive if the surface barrier is thin, but determining the nature of the surface barrier could suggest further experiments to tune the external pore structure of membranes and adsorbents for improved molecular sieving.

# Bibliography

All references cited in Chapters 1 and 2 are listed below. References cited in Chapters 3, 4, and 5 are listed at the end of their respective chapters, and also by chapter here.


[1] S. Kulprathipanja, Zeolites in industrial separation and catalysis, 2010.

[2] Database of Zeolite Structures, Http://www.iza-Structure.org. (2017). http://www.iza-structure.org/databases/ (accessed July 25, 2017).

[3] R. Szostak, MOLECULAR SIEVES Principles of Synthesis and Identification, in: Springer, NewYork, 1989.

[4] Y. Luo, H.H. Funke, J.L. Falconer, R.D. Noble, Adsorption of $CO_2$ , $CH_4$ , $C_3H_8$ , and $H_2O$ in SSZ-13, SAPO-34, and T‑Type Zeolites, Industrial & Engineering Chemistry Research 2016 55 (36), 9749-9757.

[5] S. Li, J.L. Falconer, R.D. Noble, SAPO-34 membranes for CO2/CH4 separations: Effect of Si/Al ratio, Micropor. Mesopor. Mater. 110 (2008) 310–317.

[6] M. Salmasi, S. Fatemi, S.J. Hashemi, MTO reaction over SAPO-34 catalysts synthesized by combination of TEAOH and morpholine templates and different silica sources, Sci. Iran. 19 (2012) 1632–1637.

[7] L. Sommer, D. Mores, S. Svelle, M. Stöcker, B.M. Weckhuysen, U. Olsbye, Mesopore formation in zeolite H-SSZ-13 by desilication with NaOH, Microporous Mesoporous Mater. 132 (2010) 384–394.

[8] R. GORRING, Diffusion of normal paraffins in zeolite T Occurrence of window effect, J. Catal. 31 (1973) 13–26.

[9] A. Luna-Triguero, J.M. Vicent-Luna, D. Dubbeldam, P. Gómez-Álvarez, S. Calero, Understanding and Exploiting Window Effects for Adsorption and Separations of Hydrocarbons, J. Phys. Chem. C. 119 (2015) 19236–19243.

[10] N.O. Chisholm, G.C. Anderson, J.F. McNally, H.H. Funke, R.D. Noble, J.L. Falconer,

Increasing H2/N2 separation selectivity in CHA zeolite membranes by adding a third gas, J. Memb. Sci. 496 (2015) 118–124.

[11] J. Kärger, S. Vasenkov, S.M. Auerbach, Handbook of Zeolite Science and Technology, 2003.

[12] R. Krishna, S. Li, J.M. van Baten, J.L. Falconer, R.D. Noble, Investigation of slowing-down and speeding-up effects in binary mixture permeation across SAPO-34 and MFI membranes, Sep. Purif. Technol. 60 (2008) 230–236.

[13] R. Krishna, J.M. van Baten, Investigating the influence of diffusional coupling on mixture permeation across porous membranes, J. Memb. Sci. 430 (2013) 113–128.

[14] R. Krishna, THE MAXWELL-STEFAN FORMULATION OF DIFFUSION IN ZEOLITES, Fluid Transport in Nanoporous Materials pp 211-240.

[15] L.J.P. Van Den Broeke, R. Krishna, Experimental verification of the Maxwell-Stefan theory for micropore diffusion, Chem. Eng. Sci. 50 (1995) 2507–2522.

[16] R. Krishna, J.M. van Baten, E. García-Pérez, S. Calero, Incorporating the Loading Dependence of the Maxwell−Stefan Diffusivity in the Modeling of $CH_4$ and $CO_2$ Permeation Across Zeolite Membranes, Ind. Eng. Chem. Res. 46 (2006) 2974–2986.

[17] D.M. Ruthven, Diffusion in zeolites—a continuing saga, Adsorption. 16 (2010) 511–514.

[18] H. Maghsoudi, Defects of Zeolite Membranes: Characterization, Modification and Post-treatment Techniques, Sep. Purif. Rev. 45 (2016) 169–192.

[19] Energy Information Administration, International Energy Outlook 2016, 2016.

[20] Z. Ying Yeo, T. Leng Chew, P. Wei Zhu, A. Rahman Mohamed, S.-P. Chai, Z. Ying Yeo—Ph, Conventional processes and membrane technology for carbon dioxide removal from natural gas: A review, J. Nat. Gas Chem. 21 (2012) 282–298.

[21] B.M. Lok, C.A. Messina, R.L. Patton, R.T. Gajek, T.R. Cannan, E.M. Flanigen, Silicoaluminophosphate molecular sieves: another new class of microporous crystalline inorganic solids, J. Am. Chem. Soc. 106 (1984) 6092–6093.

[22] D.W. Breck, Zeolite molecular sieves : structure, chemistry, and use, 1974.

[23] E.M. FLANIGEN, R.W. GROSE, Phosphorus Substitution in Zeolite Frameworks, in: 1974: pp. 76–101.

[24] S.T. Wilson, B.M. Lok, C.A. Messina, T.R. Cannan, E.M. Flanigen, Aluminophosphate molecular sieves: a new class of microporous crystalline inorganic solids, J. Am. Chem. Soc. 104 (1982) 1146–1147.

[25] Z. Lixiong, J. Mengdong, M. Enze, Synthesis of SAPO-34/ceramic composite membranes, Stud. Surf. Sci. Catal. 105 (1997) 2211–2216.

[26] J.C. Poshusta, V.A. Tuan, E.A. Pape, R.D. Noble, J.L. Falconer, Separation of light gas mixtures using SAPO-34 membranes, AIChE J. 46 (2000) 779–789.

[27] J.C. Poshusta, V.A. Tuan, E.A. Pape, R.D. Noble, J.L. Falconer, Separation of light gas mixtures using SAPO-34 membranes, AIChE J. 46 (2000) 779–789.

[28] S. Li, J.G. Martinek, J.L. Falconer, R.D. Noble, T.Q. Gardner, High-Pressure $CO_2$ /$CH_4$ Separation Using SAPO-34 Membranes, Ind. Eng. Chem. Res. 44 (2005) 3220–3228.

[29] M.A. Carreon, S. Li, J.L. Falconer, R.D. Noble, SAPO-34 Seeds and Membranes Prepared Using Multiple Structure Directing Agents, Adv. Mater. 20 (2008) 729–732.

[30] M.A. Carreon, S. Li, J.L. Falconer, R.D. Noble, Alumina-Supported SAPO-34 Membranes for $CO_2$ /$CH_4$ Separation, J. Am. Chem. Soc. 130 (2008) 5412–5413.

[31] R. Zhou, E.W. Ping, H.H. Funke, J.L. Falconer, R.D. Noble, Improving SAPO-34 membrane synthesis, J. Memb. Sci. 444 (2013) 384–393.

[32] A.M. Avila, H.H. Funke, Y. Zhang, J.L. Falconer, R.D. Noble, Concentration polarization in SAPO-34 membranes at high pressures, J. Memb. Sci. 335 (2009) 32–36.

[33] S.I. Zones, Zeolite SSZ-13 and its method of preparation, US4544538 A, 1983.

[34] H. Kalipcilar, T.C. Bowen, R.D. Noble, J.L. Falconer, Synthesis and separation performance of SSZ-13 zeolite membranes on tubular supports, Chem. Mater. 14 (2002)

3458–3464.

[35] H. Robson, How to read a patent, Microporous Mesoporous Mater. 22 (1998) 551,580.

[36] N. Kosinov, C. Auffret, C. Gücüyener, B.M. Szyja, J. Gascon, F. Kapteijn, et al., High flux high-silica SSZ-13 membrane for $CO_2$ separation, J. Mater. Chem. A. 2 (2014) 13083–13092.

[37] N. Kosinov, C. Auffret, V.G.P. Sripathi, C. Gücüyener, J. Gascon, F. Kapteijn, et al., Influence of support morphology on the detemplation and permeation of ZSM-5 and SSZ-13 zeolite membranes, Microporous Mesoporous Mater. 197 (2014) 268–277.

[38] Y. Zheng, N. Hu, H. Wang, N. Bu, F. Zhang, R. Zhou, Preparation of steam-stable high-silica CHA (SSZ-13) membranes for CO2/CH4 and C2H4/C2H6 separation, J. Memb. Sci. 475 (2015) 303–310.

[39] N. Kosinov, C. Auffret, G.J. Borghuis, V.G.P. Sripathi, E.J.M. Hensen, Influence of the Si/Al ratio on the separation properties of SSZ-13 zeolite membranes, J. Memb. Sci. 484 (2015) 140–145.

[40] J.C. Poshusta, R.D. Noble, J.L. Falconer, Characterization of SAPO-34 membranes by water adsorption, J. Memb. Sci. 186 (2001) 25–40.

[41] S. Li, G. Alvarado, R.D. Noble, J.L. Falconer, Effects of impurities on CO2/CH4 separations through SAPO-34 membranes, J. Membr. Sci. 251 (2005) 59–66.

[42] T. Wu, M.C. Diaz, Y. Zheng, R. Zhou, H.H. Funke, J.L. Falconer, et al., Influence of propane on CO2/CH4 and N2/CH4 separations in CHA zeolite membranes, J. Membr. Sci. 473 (2015) 201–209.

[43] D.M. Ford, E.D. Glandt, Steric hindrance at the entrances to small pores, J. Memb. Sci. 107 (1995) 47–57.

[44] D.M. Ford, E.D. Glandt, Molecular Simulation Study of the Surface Barrier Effect. Dilute Gas Limit, J. Phys. Chem. 99 (1995) 11543–11549.

[45] F. Vigne´-Maeder, S. El Amrani, P. Ge´lin, An approach to the surface barrier concept in

diffusion in zeolites by computer simulation, J. Catal. 134 (1992) 536–541.

[46] D.A. Newsome, D.S. Sholl, Influences of Interfacial Resistances on Gas Transport through Carbon Nanotube Membranes, NANO Lett. 6 (2006) 2150–2153.

[47] P. Grenier, F. Meunier, P.G. Gray, Diffusion of methanol in NaX crystals: Comparison of i.r., ZLC, and PFG-n.m.r. measurements, Zeolites. 14 (1994) 242–249.

[48] J. Kärger, M. Hunger, H. Freude, H. Pfeifer, J. Caro, M. Bulow, et al., NMR investigations on molecular transport in ZSM-5 type zeolites containing structural defects, Catal. Today. 3 (1988) 493–499.

[49] J. Karger, H. Pfeifer, F. Stallmach, H. Spindler, 129Xe n.m.r. self-diffusion measurements - a novel method to probe diffusional barriers on the external surface of zeolite crystallites, Zeolites. 10 (1990) 288–292.

[50] J. Wloch, Effect of surface etching of ZSM-5 zeolite crystals on the rate of n-hexane sorption, Microporous Mesoporous Mater. 62 (2003) 81–86.

[51] P. Kortunov, S. Vasenkov, C. Chmelik, J. Kärger, D.M. Ruthven, J. Wloch, Influence of Defects on the External Crystal Surface on Molecular Uptake into MFI-Type Zeolites, Chem. Mater. 16 (2004) 3552–3558.

[52] A.R. Teixeira, C.-C. Chang, T. Coogan, R. Kendall, W. Fan, P.J. Dauenhauer, Dominance of Surface Barriers in Molecular Transport through Silicalite-1, J. Phys. Chem. C. 117 (2013) 25545–25555.

[53] G.N. Kalantzopoulos, A. Policicchio, E. Maccallini, I. Krkljus, F. Ciuchi, M. Hirscher, et al., Resistance to the transport of H2 through the external surface of as-made and modified silicalite-1 (MFI), Microporous Mesoporous Mater. 220 (2016) 290–297.

[54] R. Szostak, Handbook of molecular sieves, Van Nostrand Reinhold, 1992.

[55] M. Kattula, K. Ponnuru, L. Zhu, E.P. Furlani, Designing ultrathin film composite membranes: The impact of a gutter layer, Sci. Rep. (2015).

**References for Chapter 3**


[1] D.W. Breck, Zeolite molecular sieves : structure, chemistry, and use, 1974, pp. 633–641.

[2] J. Karger, D.M. Ruthven, Diffusion in Zeolites and Other Microporous Solids, John Wiley, New York, NY, 1992.

[3] E.W. Ping, R. Zhou, H.H. Funke, J.L. Falconer, R.D. Noble, Seeded-gel synthesis of SAPO-34 single channel and monolith membranes, for $CO_2/CH_4$ separations, J. Membr. Sci. 415-416 (2012) 770–775.

[4] R. Zhou, E.W. Ping, H.H. Funke, J.L. Falconer, R.D. Noble, Improving SAPO-34 membrane synthesis, J. Memb. Sci. 444 (2013) 384–393.

[5] A.J. Kidney, W.R. Parrish, Fundamentals of Natural Gas Processing, Taylor & Francis Group, Boca Raton, FL, 2006.

[6] E.J. Dung, L.S. Bombom, T.D. Agusomu, The effects of gas flaring on crops in the Niger Delta, Nigeria, GeoJournal. 73 (2008) 297–305.

[7] S. Li, G. Alvarado, R.D. Noble, J.L. Falconer, Effects of impurities on $CO_2/CH_4$ separations through SAPO-34 membranes, J. Membr. Sci. 251 (2005) 59–66.

[8] T. Wu, M.C. Diaz, Y. Zheng, R. Zhou, H.H. Funke, J.L. Falconer, R.D. Noble, Influence of propane on $CO_2/CH_4$ and $N_2/CH_4$ separations in CHA zeolite membranes, J. Membr. Sci. 473 (2015) 201–209.

[9] J.F.M. Denayer, L.I. Devriese, S. Couck, J. Martens, R. Singh, P.A. Webley, G.V. Baron, Cage and window effects in the adsorption of n-alkanes on chabazite and SAPO-34, J. Phys. Chem. C. 112 (2008) 16593–16599.

[10] C. Nicolas, M. Pera-Titus, Nanocomposite MFI-alumina hollow fiber membranes: Influence of $NO_x$ and propane on $CO_2/N_2$ separation properties, Ind. Eng. Chem. Res. 51 (2012) 10451–10461.

[11] J.B. Lee, H.H. Funke, R.D. Noble, J.L. Falconer, High selectivities in defective MFI membranes, J. Memb. Sci. 321 (2008) 309–315.

[12] S. Himeno, T. Tomita, K. Suzuki, K. Nakayama, K. Yajima, S. Yoshida, Synthesis and permeation properties of a DDR-type zeolite membrane for separation of $CO_2/CH_4$ gaseous mixtures, Ind. Eng. Chem. Res. 46 (2007) 6989–6997.

[13] W. Zhu, F. Kapteijn, J.A. Moulijn, Shape selectivity in the adsorption of propane/propene on the all-silica DD3R, Chem. Commun. (1999) 2453–2454.

[14] C.D. Baertsch, H.H. Funke, J.L. Falconer, R.D. Noble, Permeation of aromatic hydrocarbon vapors through silicalite−zeolite membranes, J. Phys. Chem. 100 (1996) 7676–7679.

[15] J.C. Poshusta, V.A. Tuan, E.A. Pape, R.D. Noble, J.L. Falconer, Separation of light gas mixtures using SAPO-34 membranes, AIChE J. 46 (2000) 779–789.

[16] G. Guan, K. Kusakabe, S. Morooka, Synthesis and permeation properties of ion-exchanged ETS-4 tubular membranes, Microporous Mesoporous Mater. 50 (2001) 109–120.

[17] M. Hong, J.L. Falconer, R.D. Noble, Modification of zeolite membranes for $H_2$ separation by catalytic cracking of methyldiethoxysilane, Ind. Eng. Chem. Res. 44 (2005) 4035–4041.

[18] G. Guan, T. Tanaka, K. Kusakabe, K.-I. Sotowa, S. Morooka, Characterization of AlPO4-type molecular sieving membranes formed on a porous a-alumina tube, J. Membr. Sci. 214 (2003) 191–198.

[19] A.M. Avila, H.H. Funke, Y. Zhang, J.L. Falconer, R.D. Noble, Concentration polarization in SAPO-34 membranes at high pressures, J. Membr. Sci. 335 (2009) 32–36.

[20] S. Li, J.L. Falconer, R.D. Noble, SAPO-34 membranes for $CO_2/CH_4$ separations: Effect of Si/Al ratio, Micropor. Mesopor. Mater. 110 (2008) 310–317.

[21] M. Salmasi, S. Fatemi, S.J. Hashemi, MTO reaction over SAPO-34 catalysts synthesized by combination of TEAOH and morpholine templates and different silica sources, Sci. Iran. 19 (2012) 1632–1637.

[22] Y. Luo, N.O. Chisholm, H.H. Funke, M.Z. Chen, J.L. Falconer, R.D. Noble, Adsorption of gases in SAPO-34 and SSZ-13 zeolites, I&ECR Prep. (2014).

[23] M. Hong, S. Li, J.L. Falconer, R.D. Noble, Hydrogen purification using a SAPO-34 membrane, J. Memb. Sci. 307 (2008) 277–283.

[24] H.H. Funke, Y. Luo, M.Z. Chen, G.C. Anderson, J.L. Falconer, R.D. Noble, Measuring mixture adsorption by temperature-programmed desorption, Ind. Eng. Chem. Res. (2015).

[25] R. Krishna, J.M. van Baten, Investigating the influence of diffusional coupling on mixture permeation across porous membranes, J. Memb. Sci. 430 (2013) 113–128.

[26] R. Krishna, S. Li, J.M. van Baten, J.L. Falconer, R.D. Noble, Investigation of slowing-down and speeding-up effects in binary mixture permeation across SAPO-34 and MFI membranes, Sep. Purif. Technol. 60 (2008) 230–236.

**References for Chapter 4**

[1] T. Wu, M.C. Diaz, Y. Zheng, R. Zhou, H.H. Funke, J.L. Falconer, et al., Influence of propane on $CO_2/CH_4$ and $N_2/CH_4$ separations in CHA zeolite membranes, J. Membr. Sci. 473 (2015) 201–209.

[2] N.O. Chisholm, G.C. Anderson, J.F. McNally, H.H. Funke, R.D. Noble, J.L. Falconer, Increasing $H_2/N_2$ separation selectivity in CHA zeolite membranes by adding a third gas, J. Memb. Sci. 496 (2015) 118–124.

[3] J.C. Poshusta, R.D. Noble, J.L. Falconer, Characterization of SAPO-34 membranes by water adsorption, J. Memb. Sci. 186 (2001) 25–40.

[4] S. Li, G. Alvarado, R.D. Noble, J.L. Falconer, Effects of impurities on $CO_2/CH_4$ separations through SAPO-34 membranes, J. Membr. Sci. 251 (2005) 59–66.

[5] K. Keizer, A.J. Burggraafa, Z.A.E.P. Vroon, H. Verweij, Two component permeation through thin zeolite MFI membranes, J. Memb. Sci. 147 (1998) 159–172.

[6] S. Mokhatab, W.A. Poe, J.Y. Mak, Handbook of Natural Gas Transmission and Processing,

3rd editio, Elsevier, Amsterdam, 2015.

[7] A.M. Avila, H.H. Funke, Y. Zhang, J.L. Falconer, R.D. Noble, Concentration polarization in SAPO-34 membranes at high pressures, J. Membr. Sci. 335 (2009) 32–36.

[8] D.V. Cao, S. Sircar, Heat of Adsorption of Pure Sulfur Hexafluoride on Micro-Mesoporous Adsorbents, in: 2001st ed., Kluwer Academic Publishers, 2001: pp. 73–80.

[9] R. Yoshimoto, K. Hara, K. Okumura, N. Katada, M. Niwa, Analysis of Toluene Adsorption on Na-Form Zeolite with a Temperature-Programmed Desorption Method, (2006).

[10] M.D. LeVan, T. Vermeulen, Binary Langmuir and Freundlich isotherms for ideal adsorbed solutions, J. Phys. Chem. 85 (1981) 3247–3250.

[11] D.W. Hand, S. Loper, M. Ari, J.C. Crittenden, Prediction of Multicomponent Adsorption Equilibria Using Ideal Adsorbed Solution Theory, Environ. Sci. Technol., 1985, 19 (11), 1037–1043.

[12] M. Sakuth, J. Meyer, J. Gmehling, Measurement and prediction of binary adsorption equilibria of vapors on dealuminated Y-zeolites (DAY), Chem. Eng. Process. Process Intensif. 37 (1998) 267–277.

[13] S. Furmaniak, S. Koter, A.P. Terzyk, P.A. Gauden, P. Kowalczyk, G. Rychlicki, New insights into the ideal adsorbed solution theory, Phys. Chem. Chem. Phys. 17 (2015) 7232–7247.

[14] R. Zhou, E.W. Ping, H.H. Funke, J.L. Falconer, R.D. Noble, Improving SAPO-34 membrane synthesis, J. Memb. Sci. 444 (2013) 384–393.

[15] S. Li, J.L. Falconer, R.D. Noble, SAPO-34 membranes for $CO_2/CH_4$ separations: Effect of Si/Al ratio, Micropor. Mesopor. Mater. 110 (2008) 310–317.

[16] M. Salmasi, S. Fatemi, S.J. Hashemi, MTO reaction over SAPO-34 catalysts synthesized by combination of TEAOH and morpholine templates and different silica sources, Sci. Iran. 19 (2012) 1632–1637.

[17] M. Nagao, Y. Suda, Adsorption of benzene, toluene, and chlorobenzene on titanium

dioxide, Langmuir. 5 (1989) 42–47.

[18] T. Morimoto, M. Nagao, Y. Suda, Heat of immersion of zinc oxide in organic liquids. 3. Immersion in benzene, toluene, and chlorobenzene, J. Phys. Chem. 89 (1985) 4881–4883.

[19] J. Garcia-Martinez, K. Li, M.E. Davis, Mesoporous zeolites : preparation, characterization and applications, Wiley, 2015.

[20] R. Krishna, L.J.P. van den Broeke, The Maxwell-Stefan description of mass transport across zeolite membranes, Chem. Eng. J. Biochem. Eng. J. 57 (1995) 155–162.

[21] F. Kapteijn, J.A. Moulijn, R. Krishna, The generalized Maxwell–Stefan model for diffusion in zeolites:, Chem. Eng. Sci. 55 (2000) 2923–2930.

[22] A.L. Myers, J.M. Prausnitz, Thermodynamics of mixed-gas adsorption, AIChE J. 11 (1965) 121–127.

[23] E.L. Cussler, Diffusion : Mass transfer in fluid systems, Cambridge University Press, 2009.

[24] H.Y. Erbil, Y. Avci, Simultaneous Determination of Toluene Diffusion Coefficient in Air from Thin Tube Evaporation and Sessile Drop Evaporation on a Solid Surface, Langmuir, 18 (2002) 5113–5119.

[25] L. Mi, S.-T. Hwang, Correlation of concentration polarization and hydrodynamic parameters in hollow fiber modules, J. Memb. Sci. 159 (1999) 143–165.

[26] J.M.S. Henis, M.K. Tripodi, Composite hollow fiber membranes for gas separation: the resistance model approach, J. Memb. Sci. 8 (1981) 233–246.

[27] E.D. Snijder, M.J.M. Te Riele, G.F. Versteeg, W.P.M. Van Swaaij, Diffusion Coefficients of CO, COS, N20, and N2 in Ethanol and Toluene, J. Chem. Eng. Data. 40 (1996) 37–39.

[28] P. Luhring, A. Schumpe, Gas Solubilities ($H_2$, He, $N_2$, $CO_2$, $O_2$, Ar, CO,) in Organic Liquids at 293.2 K, J. Chem. Eng. Data. 34 (1989) 250–252.

**References for Chapter 5**

[1] Y. Zheng, N. Hu, H. Wang, N. Bu, F. Zhang, R. Zhou, Preparation of steam-stable high-

silica CHA (SSZ-13) membranes for $CO_2/CH_4$ and $C_2H_4/C_2H_6$ separation, J. Memb. Sci. 475 (2015) 303–310.

[2] N. Kosinov, C. Auffret, G.J. Borghuis, V.G.P. Sripathi, E.J.M. Hensen, Influence of the Si/Al ratio on the separation properties of SSZ-13 zeolite membranes, J. Memb. Sci. 484 (2015) 140–145.

[3] M.A. Carreon, S. Li, J.L. Falconer, R.D. Noble, Alumina-Supported SAPO-34 Membranes for $CO_2/CH_4$ Separation, J. Am. Chem. Soc. 130 (2008) 5412–5413.

[4] R. Zhou, E.W. Ping, H.H. Funke, J.L. Falconer, R.D. Noble, Improving SAPO-34 membrane synthesis, J. Memb. Sci. 444 (2013) 384–393.

[5] T. Wu, M.C. Diaz, Y. Zheng, R. Zhou, H.H. Funke, J.L. Falconer, et al., Influence of propane on $CO_2/CH_4$ and $N_2/CH_4$ separations in CHA zeolite membranes, J. Membr. Sci. 473 (2015) 201–209.

[6] Y. Luo, H.H. Funke, J.L. Falconer, R.D. Noble, Adsorption of $CO_2$, $CH_4$, $C_3H_8$, and $H_2O$ in SSZ-13, SAPO-34, and T‑Type Zeolites, Ind. Eng. Chem. Res. 55 (2016) 9749–9757.

[7] N. Chisholm, H. Funke, R. Noble, J. Falconer, Effect of toluene on $CO_2$ and $N_2$ permeance in SAPO-34 membranes, in prep.

[8] D.H. Olson, Light hydrocarbon separation using 8-member ring zeolites, US6488741 B2, 2001.

[9] H.H. Funke, M.Z. Chen, A.N. Prakash, J.L. Falconer, R.D. Noble, Separating molecules by size in SAPO-34 membranes, J. Memb. Sci. 456 (2014) 185–191.

[10] D.M. Ford, E.D. Glandt, Steric hindrance at the entrances to small pores, J. Memb. Sci. 107 (1995) 47–57.

[11] D.M. Ford, E.D. Glandt, Molecular Simulation Study of the Surface Barrier Effect. Dilute Gas Limit, J. Phys. Chem. 99 (1995) 11543–11549.

[12] D.A. Newsome, D.S. Sholl, Influences of Interfacial Resistances on Gas Transport through

Carbon Nanotube Membranes, NANO Lett. 6 (2006) 2150–2153.

[13] P. Grenier, F. Meunier, P.G. Gray, Diffusion of methanol in NaX crystals: Comparison of i.r., ZLC, and PFG-n.m.r. measurements, Zeolites. 14 (1994) 242–249.

[14] J. Kärger, M. Hunger, H. Freude, H. Pfeifer, J. Caro, M. Bulow, et al., NMR investigations on molecular transport in ZSM-5 type zeolites containing structural defects, Catal. Today. 3 (1988) 493–499.

[15] J. Karger, H. Pfeifer, F. Stallmach, H. Spindler, 129Xe n.m.r. self-diffusion measurements - a novel method to probe diffusional barriers on the external surface of zeolite crystallites, Zeolites. 10 (1990) 288–292.

[16] G.N. Kalantzopoulos, A. Policicchio, E. Maccallini, I. Krkljus, F. Ciuchi, M. Hirscher, et al., Resistance to the transport of H2 through the external surface of as-made and modified silicalite-1 (MFI), Microporous Mesoporous Mater. 220 (2016) 290–297.

[17] J. Kärger, Measurement of Diffusion in Zeolites—A Never Ending Challenge?, Adsorption. 9 (2003) 29–35.

[18] F. Vigne´-Maeder, S. El Amrani, P. Ge´lin, An approach to the surface barrier concept in diffusion in zeolites by computer simulation, J. Catal. 134 (1992) 536–541.

[19] A.R. Teixeira, C.-C. Chang, T. Coogan, R. Kendall, W. Fan, P.J. Dauenhauer, Dominance of Surface Barriers in Molecular Transport through Silicalite-1, J. Phys. Chem. C. 117 (2013) 25545–25555.

[20] J. Wloch, Effect of surface etching of ZSM-5 zeolite crystals on the rate of n-hexane sorption, Microporous Mesoporous Mater. 62 (2003) 81–86.

[21] P. Kortunov, S. Vasenkov, C. Chmelik, J. Kärger, D.M. Ruthven, J. Wloch, Influence of Defects on the External Crystal Surface on Molecular Uptake into MFI-Type Zeolites, Chem. Mater. 16 (2004) 3552–3558.

# Appendix A

The following publication was a collaboration with colleagues from the Chemical and Biological Engineering Department at CU. Will McDanel, with help from Matthew Cowan, synthesized novel polymer membranes in Doug Gin and Rich Noble's lab. Our lab helped design and build a flow system with water bubblers and sweep gas to measure $CO_2$ and $N_2$ permeances at low feed pressures in a hydrated environment, and worked with them to calibrate and run the system. The membranes have applications in $CO_2$ removal from power plant flue gases.

## Fixed-site-carrier Facilitated Transport of Carbon Dioxide through Ionic-liquid-based Epoxy-amine Ion Gel Membranes

*William M. McDanel,§ Matthew G. Cowan,§,‡ Nicholas O. Chisholm, § Douglas L. Gin,§, ‡*and Richard D. Noble§**

§Department of Chemical and Biological Engineering, and ‡Department of Chemistry and Biochemistry, University of Colorado, Boulder, CO 80309, USA

**Abstract:**

The amine functional groups in room-temperature ionic liquid (RTIL)-based epoxy-amine ion gel membranes allow for the fixed-site-carrier facilitated transport of $CO_2$. These membranes were tested under humidified mixed-gas ($CO_2/N_2$) feeds in order to evaluate the effects of relative

humidity, $CO_2$ partial pressure, and hydrophobicity of the added free RTIL on $CO_2/N_2$ separation performance. Changes in relative humidity were found to have little effect on $CO_2/N_2$ separation performance at constant $CO_2$ partial pressure. However, comparison to dry-gas measurements showed that the presence of water vapor is necessary to observe facilitated $CO_2$ transport in these systems. Increased $CO_2$ permeability and $CO_2/N_2$ selectivity were observed for these epoxy-amine ion gel membranes with decreasing $CO_2$ partial pressure, as expected for materials operating via the fixed-site-carrier facilitated transport mechanism. The hydrophilicity of the free RTIL was found to influence $CO_2$ transport, with a more hydrophilic RTIL able to facilitate $CO_2$ transport at lower relative humidity. Facilitated transport enhances the $CO_2/N_2$ separation performance of these epoxy-amine ion gel membranes and enables them to exceed the 2008 Robeson Plot upper bound.

## 1. Introduction

Carbon dioxide ($CO_2$) gas accounts for roughly 80% of anthropogenic greenhouse gas emissions and has been associated with both global climate change and ocean acidification.[1] To mitigate the unavoidable environmental consequences related to these phenomena, it is desirable to prevent or limit atmospheric $CO_2$ emissions from large point sources, such as coal and natural gas-fired power plants. This can be achieved by post-combustion carbon capture and sequestration (CCS). CCS involves the capture, and purification of $CO_2$, followed by sequestration and/or utilization of the captured $CO_2$.[2]

The first step in post-combustion CCS technology requires an inexpensive, large-scale method of separating $CO_2$ from the other light gases present in flue gas (primarily $N_2$).[2, 3] Conventional technologies to separate $CO_2$ from flue gas streams include amine adsorption, cryogenic separations, pressure swing adsorption, and membrane separations.[4] Polymeric gas separation membranes offer the relative advantages of low operating and capital costs, ease of

operation, and modularity, due to their smaller size.[5, 6] For these reasons, there has been considerable scientific and industrial effort to design and develop polymeric membrane materials for post-combustion CCS.

Gas transport in dense polymer membranes proceeds via the solution-diffusion transport mechanism. Gas molecules transport across a partial pressure gradient by dissolving at the upstream (feed) interface, diffusing through the membrane and desorbing at the downstream (permeate) interface.[7, 8] All polymers have an inherent gas permeability and selectivity. Gas permeability is defined as the gas flux, normalized to the membrane thickness and transmembrane pressure difference. Gas selectivity is the ratio of the permeability of the faster gas species through the membrane to that of the slower gas penetrant.[7]

For polymer membranes, a permeability-selectivity trade-off is typically observed, (i.e., as polymers become more permeable they also become less selective). This trade-off is represented by the empirically-derived Robeson upper bound, which has been explained by Freeman.[8-10] In general, a membrane material with permeability-selectivity behavior close to or above the $CO_2/N_2$ upper bound has excellent separation potential for post-combustion CCS. A major challenge for membrane-based $CO_2$ separation is to produce membranes with both high $CO_2$ permeance and high $CO_2/N_2$ selectivity in order to compete with traditional separation technologies.[5]

Room-temperature ionic liquid (RTIL)-based materials have been explored for $CO_2/N_2$ separations because of their negligible vapor pressure, inherently good $CO_2$/light gas solubility selectivity, and high $CO_2$ diffusivity compared to most polymer membranes.[11, 12] RTIL-based ion gels are defined as solid-liquid composite materials that utilize cross-linked, polymerized room-temperature ionic liquids (poly(RTIL)s) to physically entrap added free RTIL.[13-16] Many groups have investigated the formation RTIL-based ion gels because the free, “unbound” RTIL provides

advantageous gas diffusivity while maintaining the mechanical properties of a solid material.[13-15, 17-19] Many RTIL-based membranes have permeability-selectivity performance for $CO_2/N_2$ separation that lies near or above the 2008 Robeson upper bound.[13-17, 20] Therefore, these materials are promising candidates for preparing high-performance membranes for CCS.[21]

Facilitated transport refers to a transport mechanism that can occur in conjunction with the solution-diffusion mechanism.[22] Facilitated transport operates by either "mobile" or "fixed-site" carriers, which are chemical functional groups capable of a reversible chemical interaction (chemical or physical) with a specific gas molecule (e.g., the reversible reaction of amines with $CO_2$). Relevant to this work are fixed-site-carrier facilitated transport membranes, in which the interactive/reactive carrier groups are fixed (i.e., covalently bonded) to the membrane.[23-25]

Fixed-site-carrier facilitated transport of $CO_2$ has been reported for many different membrane compositions.[26-30] Amine-containing polymers and small molecules are the most common $CO_2$ carriers. Humidified, mixed-gas permeation tests are generally required to effectively evaluate whether or not facilitated transport occurs in these membranes. The role of humidification (i.e., presence of water vapor) for the amine-facilitated transport of $CO_2$ is depicted in Figure 1.[31, 32] Reactions 1–4 in Figure 1 make up the zwitterion mechanism in which water acts as a co-reagent with primary (1°) or secondary (2°) amines to react with $CO_2$.[33] $CO_2$ first reacts with either a 1° or 2° amine to form a zwitterion intermediate (reaction 1). The zwitterion is then deprotonated by another amine or $H_2O$ to form a carbamate salt (reactions 2 and 3). Lastly, the carbamate ion can react with $H_2O$ to form bicarbonate, ($HCO_3^-$). $CO_2$ transport can be facilitated in the form of bound carbamate and $HCO_3^-$. Lastly, the presence of tertiary (3°) amines can facilitate the transport of $CO_2$ via reaction 5, wherein $CO_2$ and $H_2O$ react with a 3° amine to form ammonium and $HCO_3^-$.

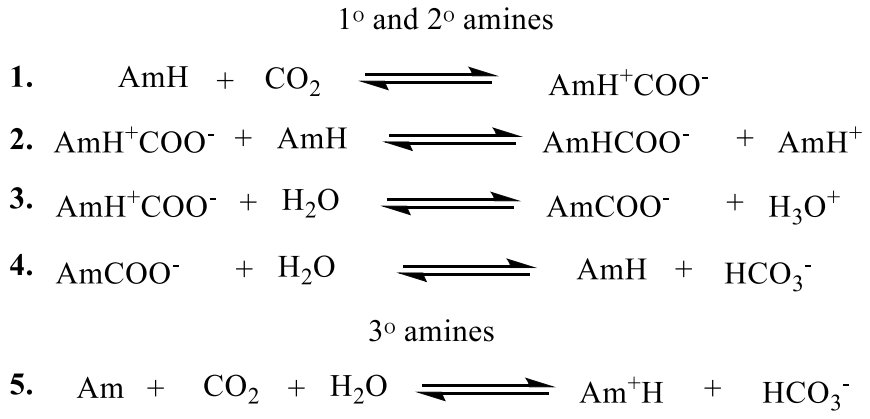


**Figure 2:** The typical reactions that occur between amines (Am) with $CO_2$. $CO_2$ transport can be facilitated by either the bound carbamate or the bicarbonate ion.

Facilitated transport operates when the carrier concentration in the membrane is similar to the solute concentration in the gas feed. At higher solute concentrations, the carrier sites become saturated, and the solution-diffusion mechanism dominates. At low solute concentrations, facilitated transport can occur and results in enhanced transport behavior. This non-linear transport behavior with solute concentration is an identifying feature of facilitated transport.[22] Since the $CO_2$ content in post-combustion flue gases is low (4–10% for natural gas-fired, and ~13% for coal-fired power plants, respectively) and contains water vapor, the facilitated transport mechanism has great potential for this separation.

Our group recently reported the use of epoxy-amine chemistry to prepare ion gel membranes containing up to 75 wt. % free RTIL (Figures 2 and 3). [15, 16] These materials possess amine functional groups in the poly(RTIL) matrix and have high $CO_2$ solubility under ideal (dry, single gas) conditions. These amine functional groups should also allow for fixed-site facilitated transport of $CO_2$ to occur.[26-30, 34] Compared to conventional materials used for fixed-site-carrier

facilitated transport, epoxy-amine ion gel membranes have higher ideal $CO_2$ permeability. [15, 16, 27, 34-36]

To our knowledge, there have been no previous literature reports of fixed-site-carrier facilitated transport in RTIL-based ion gel membranes. In this study, we report the observation of facilitated transport in epoxy-amine ion gel membranes. Humidified, mixed-gas feed streams were used to evaluate the key parameters of relative humidity (RH), $CO_2$ partial pressure, and the relative hydrophobicity of the added free RTIL on the $CO_2/N_2$ separation performance. Herein, we show that water vapor is necessary to observe facilitated transport in RTIL-based epoxy-amine ion gel membranes; that the $CO_2$ permeability and $CO_2/N_2$ selectivity of some epoxy-amine ion gel membranes increases with decreasing $CO_2$ partial pressure, indicative of facilitated transport; that a more hydrophilic free RTIL results in larger enhancements in $CO_2/N_2$ separation performance; and that higher amounts water vapor and higher amine loading are necessary to observe facilitated transport when a hydrophobic RTIL is used. The $CO_2/N_2$ separation performance of these systems falls near or above the 2008 Robeson upper bound.

## 2. Experimental

### 2.1 Materials and Instrumentation

Helium, $CO_2$, and $N_2$ gas cylinders were purchased from Airgas (Randor, PA) with gas purities of ≥99.99%. Omnipore™ (porous poly(tetrafluoroethylene) (PTFE), average pore size 0.2 μm, and 80% porosity) membrane filters were purchased from EMD Millipore. Hydrophobic PTFE membrane filters were purchased from Advantec (cat. no. T020A047A, average pore size 0.2 μm, and 74% porosity). $^{1}H$ and $^{13}C$ NMR spectra were acquired using a Bruker Avance-III 300 spectrometer. Membrane thicknesses were measured with a digital micrometer. FT-IR spectra

were obtained using a Nicolet 6700 FT-IR spectrometer in attenuated total reflectance (ATR) mode. A Hewlett Packard 5890 gas chromatography instrument equipped with a HayeSep D column and a thermal conductivity detector was used to analyze the feed and sweep stream compositions for the mixed-gas permeation studies. The membrane materials displayed in Figure 2 were synthesized as previously described in the literature, and their characterization and purity data agree with those reported.[12, 14, 15, 37]

## 2.2 Mixed-gas permeation tests

Figure S1 in the Supporting Information displays a schematic of the mixed-gas permeation system used in this study. A membrane area of 11 $cm^2$ was used for the permeation tests. The active membranes were placed on top of a hydrophobic PTFE filter to provide additional support and prevent RTIL contamination in the system.[20] The feed flow rate was held at either 50 or 100 $cm^3$ (STP)/min, and the sweep flow rate was held at 7 $cm^3$ (STP)/min. All measurements were collected at room temperature with a feed pressure of 102 kPa and a sweep/permeate pressure of 85 kPa. The membranes were allowed to equilibrate for at least 3 h after changing any experimental parameter to ensure data was collected under steady-state. The feed flow rate was much higher than the permeate flow rate ensuring that the stage cut was <1 %. Gas chromatography samples were collected every 6 min over 2 h and used to calculate the gas permeability of component *i* using Eq. 1:

$$P_i = \frac{x_i^p \, S \, l}{A \, \emptyset \, \Delta p_i} \qquad \text{(Eq. 1)}$$

where $P_i$ is the permeability of component *i*, $x_i^p$ is the mole fraction of component *i* in the sweep stream, $S$ is the helium sweep flow rate, $l$ is the membrane thickness, $x_{he}^p$ is the mole fraction of

helium in the sweep stream, $A$ is the area of the film, $\emptyset$ is the porosity of the membrane support, and $\Delta p_i$ is the partial pressure difference across the membrane for component $i$.[38]

## 2.3 Fabrication of epoxy-amine ion-gel membranes

The components used to prepare the ion gel membranes in this study are shown in Figure 2. To prepare the ion gel membranes, the bis(epoxide) RTIL monomer was first massed in a small glass vial and then free RTIL was added at a ratio to achieve 75 wt. % free RTIL. Amine monomer was then added to the vial via a micropipette, and the homogenous mixture was vortexed for 1 min. The vial was allowed to sit until the air bubbles escaped from the solution. The liquid mixture was then poured onto a 47-mm-diameter Omnipore™ support and clamped between two Rain-X-treated glass plates with binder clips. The plates were placed in a 50 °C oven for at least 3 h to ensure complete monomer conversion. After cooling to room temperature, the glass plates were separated and the excess material was removed from the edges of the membrane with a razor blade. This method produced supported membranes with thicknesses that ranged between 45–55 μm.

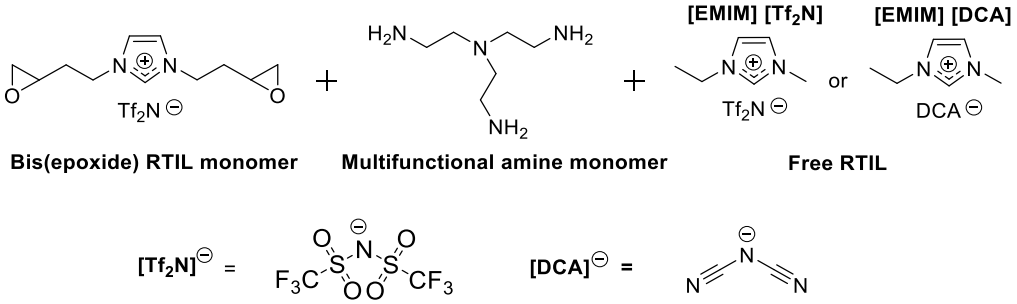


**Figure 3:** The RTIL components used to form the epoxy-amine ion gel membranes in this study.

Membranes were prepared with either a 3:2 or 3:1 bis(epoxide) monomer-to-amine monomer mole ratio (hypothetical structures are displayed in Figure 3). Epoxy-amine resins with 3:2 stoichiometries have more lower order (i.e., 1° and 2°) amine functionality present in the

formed poly(RTIL) matrix and interact more strongly with $CO_2$.[15, 16] FT-IR analysis of the ion gel membranes showed epoxide group conversions between 65–75%.

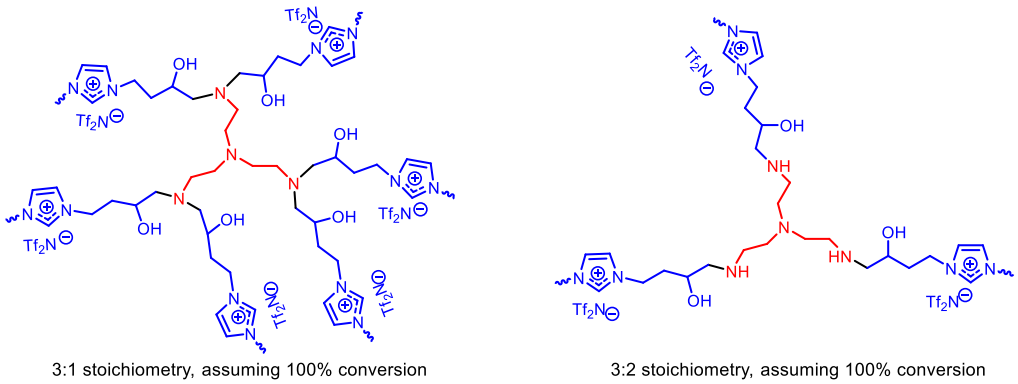


**Figure 4:** Idealized representations of the repeat units in fully cured (i.e.,100% conversion) networks produced using 3:1 and 3:2 mole ratios of the bis(epoxide) RTIL monomer and multifunctional amine monomer shown in Figure 2 (no added free RTIL shown). These network structures propagate indefinitely in three dimensions. Reproduced from reference 15 with permission. Copyright, Elsevier 2014.

## 3. Results and Discussion

### 3.1 Selection and preparation of epoxy-amine ion gels

The RTIL-based membrane materials in this study are displayed in Figure 2. The bis(epoxide) monomer and amine monomers were chosen because they can form ion gel membranes with up to 75 wt. % free RTIL and have the highest $CO_2$ permeability of the previously reported epoxy-amine ion gel membranes.[15, 16]

The free RTIL 1-ethyl-3-methylimidazolium bis(trifluoromethylsulfonyl)imide ([EMIM] [$Tf_2N$]) was selected for this study because it is the most commonly used RTIL in ion gels.[14-16, 18, 19] Additionally, 1-ethyl-3-methylimidazolium dicyanamide ([EMIM] [DCA]) was chosen because this RTIL is miscible with water and has excellent ideal $CO_2/N_2$ separation performance.[20] Comparison of [EMIM] [$Tf_2N$] and [EMIM] [DCA] in the ion gel membranes allows for the

evaluation of the effect of the added free RTIL hydrophobicity on $CO_2/N_2$ separation performance. In all cases, the bis(epoxide) RTIL monomer shown in Figure 2 (with a [$Tf_2N$] anion) was used, so only the hydrophilicity of the free RTIL component was varied.

The 3:1 and 3:2 epoxide:amine monomer ratios were chosen because they allow comparison of materials comprised of largely 2° amines (3:2 epoxide:amine monomer ratio) vs. 3° amines (3:1 epoxide:amine monomer ratio) on the facilitated transport of $CO_2$ (Figure 3).[15, 16] Further, 3:2 membranes have twice the number of amine sites and therefore, since carrier concentration is an important parameter for facilitated transport, this comparison will provide useful information regarding the facilitated transport potential of these materials.[22-25]

The primary mixed-gas permeation experiments of this study involve the testing of 4 different membrane compositions. Two membranes contained [EMIM] [$Tf_2N$] as the free RTIL with either a 3:2 or 3:1 monomer stoichiometry, and the other two membranes contained [EMIM] [DCA] with either 3:2 or 3:1 monomer stoichiometry. "Control" ion gel membranes were prepared with [EMIM] [DCA] and [EMIM] [$Tf_2N$] and a poly(RTIL) matrix that does not contain amines (see Figure S2 in the Supporting Information).[14]

## 3.2 Mixed-gas permeation results

### 3.2.1 Effect of RH on ion gel membrane $CO_2/N_2$ permeability and selectivity

The RH was varied from 40–95% to determine its effect on $CO_2/N_2$ separation performance at a constant $CO_2$ partial pressure of 20 kPa. Figure 4A displays the measured $CO_2$ permeability values and Figure 4B displays the $CO_2/N_2$ permeability selectivity values.

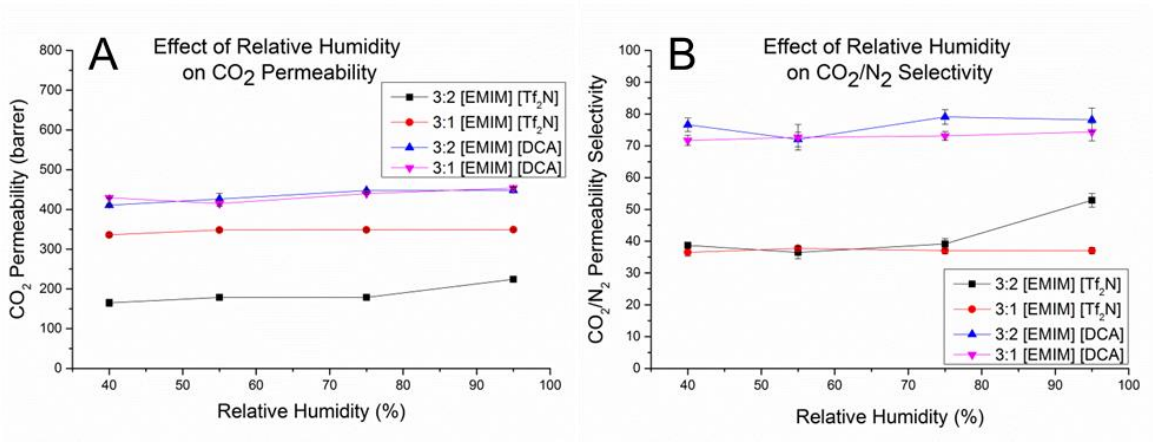


**Figure 5:** Effect of RH on: A) the $CO_2$ permeability and B) the $CO_2/N_2$ permeability selectivity for the epoxy-amine ion gel membranes studied. 1 barrer = $10^{-10}$ (($cm^3$ (STP) cm)/($cm^2$ s cmHg)).

As shown, ion gel membranes prepared with [EMIM] [DCA] have higher $CO_2$ permeability and $CO_2/N_2$ selectivity compared to the [EMIM] [$Tf_2N$]-containing ion gel membranes over the RH range studied (Figures 4A and 4B). Similar to dry gas measurements, [EMIM] [DCA]-containing ion gels have higher $CO_2/N_2$ selectivity. In contrast to dry-gas measurements (where [EMIM] [DCA] has a lower permeability than [EMIM] [$Tf_2N$]), the hydrophilic [EMIM] [DCA]-containing ion gels display higher $CO_2$ permeability than the hydrophobic [EMIM] [$Tf_2N$].[20] Previous studies suggest that this is due to greater swelling and water absorption in the [EMIM] [DCA]-based ion gel.[26]

The 3:1 and 3:2 membranes containing [EMIM] [DCA] have $CO_2$ permeabilities (410—450 barrer) that are very similar and change little over the RH range studied. The $CO_2$ permeability of the 3:1 [EMIM] [$Tf_2N$] membrane (335—350 barrer) remains relatively constant, while the $CO_2$ permeability of the 3:2 [EMIM] [$Tf_2N$] membrane increases by a factor of 1.36 (from 165—225 barrer) over the RH range studied. The higher permeability for 3:1 [EMIM] [$Tf_2N$] membranes, compared to the 3:2 [EMIM] [$Tf_2N$] membrane, is consistent with previously reported data on

these materials under ideal conditions.[15] 3:1 [EMIM] [$Tf_2N$] membranes are more permeable than 3:2 materials due to less cross-linking and the presence of higher-order (i.e., 3°) amines that interact less strongly with $CO_2$, thus improving $CO_2$ diffusivity.

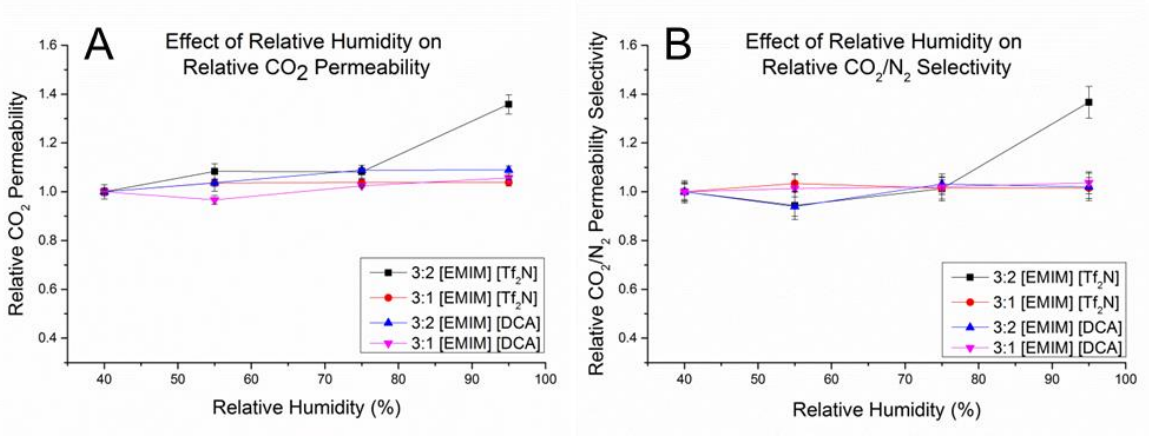


**Figure 6:** Effect of RH on A) the relative $CO_2$ permeability and B) the relative $CO_2/N_2$ permeability selectivity for the epoxy-amine ion gel membranes studied. The permeability and selectivity values are normalized to their values at RH = 40% to evaluate the effect of increasing humidity on performance.

Figures 5A and 5B show the $CO_2$ permeability and $CO_2/N_2$ selectivity data for the epoxy-amine ion gel membranes normalized to the values for each membrane at 40% RH. This allows for the evaluation of the dimensionless facilitation factor with increasing RH. As evidenced in Figures 5A and 5B, the 3:2 membrane with [EMIM] [$Tf_2N$] is most affected by changes in RH. The $CO_2$ permeability and $CO_2/N_2$ selectivity values of this membrane are increased by factors of 1.36 and 1.37 at 95% RH. The constant facilitation factor for the 3:2 [EMIM] [$Tf_2N$] membrane until 95% RH suggests that a threshold RH value is reached that allows facilitated transport to occur. This observation can be attributed to the hydrophobic nature of [EMIM] [$Tf_2N$], which limits the amount of absorbed water in the membrane. In contrast, the hydrophilic [EMIM] [DCA] promotes water absorption, enabling facilitated transport at lower RH.

### 3.2.2 Effect of $CO_2$ partial pressure at either 40% or 95% RH

#### 3.2.2.1 Permeation studies at 40% RH

The effect of $CO_2$ partial pressure was evaluated at either 40% or 95% RH by varying the $CO_2$ partial pressure from 2.5 to 50 kPa. Figure 6A displays the $CO_2$ permeability vs. $CO_2$ partial pressure and Figure 6B displays the $CO_2/N_2$ selectivity vs. $CO_2$ partial pressure at 40% RH.

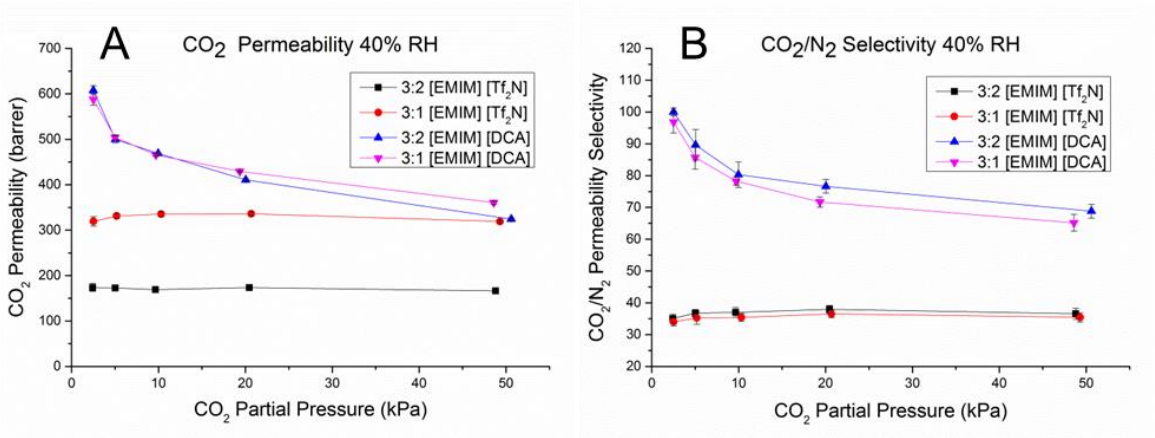


**Figure 7:** Effect of $CO_2$ partial pressure at 40% RH on A) the $CO_2$ permeability and B) the $CO_2/N_2$ permeability selectivity of the epoxy-amine ion gel membranes studied.

[EMIM] [DCA]-containing membranes show enhanced $CO_2$ permeability and $CO_2/N_2$ selectivity with decreasing $CO_2$ partial pressure while [EMIM] [$Tf_2N$]-containing membranes do not. This demonstrates that ion gels incorporating the hydrophilic [EMIM] [DCA] are capable of facilitated transport at 40% RH, whereas the hydrophobic [EMIM] [$Tf_2N$]-containing ion gels are not. Therefore, this suggests that hydrophilic free RTILs are better candidates for obtaining facilitated transport at low RH. The 2–3 times higher $CO_2/N_2$ selectivity of the [EMIM] [DCA]-containing membranes at 40% RH is explained in Section 3.2.1.

At higher $CO_2$ feed partial pressures, the amine carrier sites on the poly(RTIL) matrix become saturated, and facilitated transport contributes less than solution-diffusion to the observed permeability. This phenomenon is demonstrated by the $CO_2$ permeability of the ion gel membranes containing [EMIM] [DCA] decreasing from 600 to ca. 350 barrer over the range of 2.5 to 50 kPa of $CO_2$ partial pressure. At high $CO_2$ partial pressures in the feed, the permeability of the 3:1 [EMIM] [$Tf_2N$] membrane is comparable to that of the membranes prepared with [EMIM] [DCA] (ca. 350 barrer), where facilitated transport plays a minor role.

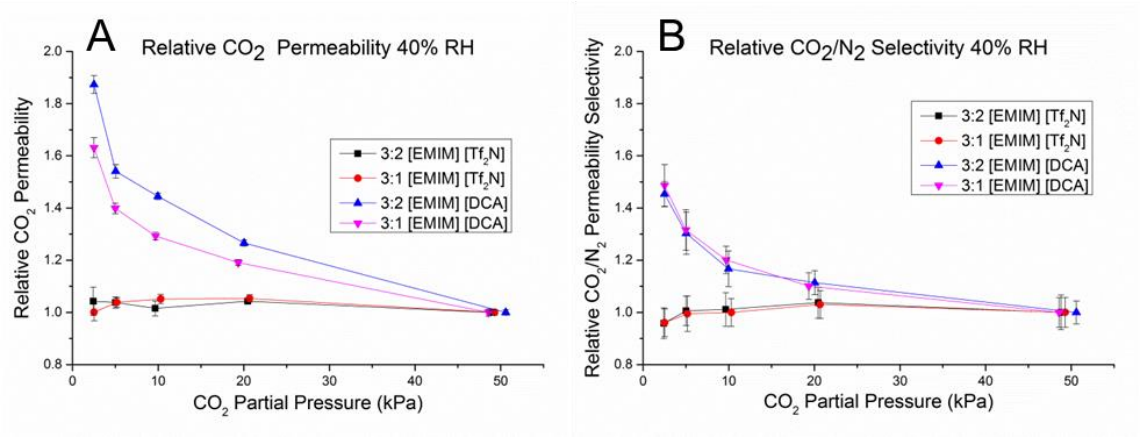


**Figure 8:** Effect of $CO_2$ partial pressure in the feed on A) the relative $CO_2$ permeability and B) the relative $CO_2/N_2$ permeability selectivity at 40% RH for the epoxy-amine ion gel membranes studied. The permeability and selectivity values are normalized to their values at 50 kPa $CO_2$ partial pressure.

Figures 7A and 7B show the permeation data for each membrane at 40% RH normalized to the $CO_2$ permeability and $CO_2/N_2$ selectivity at 50 kPa $CO_2$ partial pressure. The largest enhancements in $CO_2/N_2$ separation behavior were observed for the 3:2 [EMIM] [DCA] system, where the $CO_2$ permeability and the $CO_2/N_2$ selectivity increased by factors of 1.87 and 1.45 with decreasing partial pressure, respectively. Significant increases are also seen for the 3:1 [EMIM] [DCA] membrane (i.e., enhancements of 1.63 and 1.49 for $CO_2$ permeability and $CO_2/N_2$

selectivity, respectively). These trends are consistent with and suggest that the transport of $CO_2$ is being facilitated at low $CO_2$ partial pressure. In contrast, the 3:1 membrane with [EMIM] [$Tf_2N$] (factors of 1.00 and 0.96, respectively) and the 3:2 membrane with [EMIM] [$Tf_2N$] (factors of 1.04 and 0.96, respectively) show small changes in $CO_2/N_2$ separation performance with decreasing partial pressure. The absence of facilitated transport for the [EMIM] [$Tf_2N$]-containing membranes at 40% RH is likely due to the relative hydrophobicity of these systems compared to the relatively hydrophilic [EMIM] [DCA] membranes, which limits the water content in the membranes.

**3.2.2.2 Permeation studies at 95% RH**

At 95% RH, $CO_2$ permeability and $CO_2/N_2$ selectivity measurements show that both the [EMIM] [DCA] (3:1 and 3:2 membranes) and the 3:2 membrane with [EMIM] [$Tf_2N$] display facilitated transport of $CO_2$ (Figures 8A and 8B).Whereas at 40% RH (Figures 6 and 7), the hydrophobic 3:2 membrane with [EMIM] [$Tf_2N$] showed no increase in permeability with decreasing $CO_2$ partial pressure. The trend for 95% RH suggests that a threshold RH is required to achieve facilitated $CO_2$ transport in that membrane composition.

The 3:1 membrane with [EMIM] [$Tf_2N$] did not display facilitated transport, even at 95% RH. The 3:1 systems have higher order amines in the poly(RTIL) structure (i.e., more 3° amines) than the 3:2 systems, that require water to react with and facilitate $CO_2$ transport (Figure 1).[33, 34] Since the 3:1 [EMIM] [$Tf_2N$]-containing membrane is hydrophobic, we assume that the water content in this membrane is below that required to activate this reaction pathway for facilitated $CO_2$ transport.

The benefit of facilitated transport is clear when analyzing the membranes prepared with [EMIM] [$Tf_2N$] (Figures 8A and 8B). At low $CO_2$ partial pressures, the 3:2 [EMIM] [$Tf_2N$] membrane (which exhibits facilitated transport), has a $CO_2/N_2$ selectivity that is double (74 vs. 37)

that of the 3:1 [EMIM] [$Tf_2N$] membrane—which does not display facilitated transport—while achieving comparable $CO_2$ permeabilities (approximately 380 barrer).

Both [EMIM] [DCA]-containing membranes show increased $CO_2$ permeability and $CO_2/N_2$ selectivity with decreasing $CO_2$ partial pressure. The 3:2 membrane with [EMIM] [DCA] outperforms the 3:1 [EMIM] [DCA] membrane at low $CO_2$ partial pressures in the feed, with $CO_2$ permeability and $CO_2/N_2$ selectivity values of 900 barrer and 140, compared to 800 barrer and 120, respectively, for the 3:1 [EMIM] [DCA]-containing membrane.

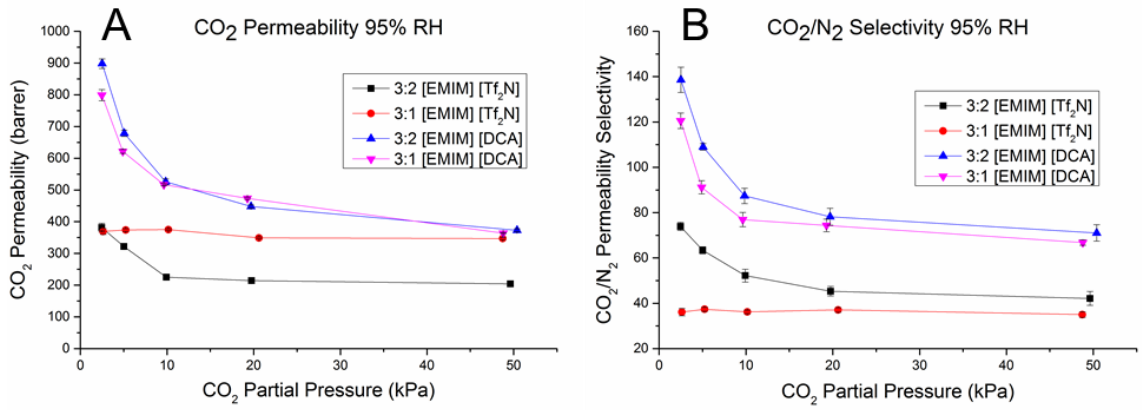


**Figure 9:** Effect of $CO_2$ partial pressure at 95% RH on A) the $CO_2$ permeability and B) the $CO_2/N_2$ permeability selectivity of the epoxy-amine ion gel membranes studied.

Figures 9A and 9B display the permeation data for the epoxy-amine ion gel membranes at 95% RH, normalized to the $CO_2$ permeability and $CO_2/N_2$ selectivity at 50 kPa $CO_2$ partial pressure. The facilitation factors for these membranes at 2.5 kPa and 95% RH are included in Table 1 (see Section 3.3). The $CO_2$ permeability and the $CO_2/N_2$ selectivity of the 3:2 [EMIM] [$Tf_2N$] membrane are facilitated by factors of 1.87 and 1.75, respectively. Similarly, the 3:2 [EMIM] [DCA] membrane exhibits facilitation factors of 2.41 and 1.95. The larger facilitation factors for the membranes prepared with [EMIM] [DCA] suggests that even at high RH, more

hydrophilic RTILs are better for the facilitated transport of $CO_2$ through epoxy-amine ion gel membranes.

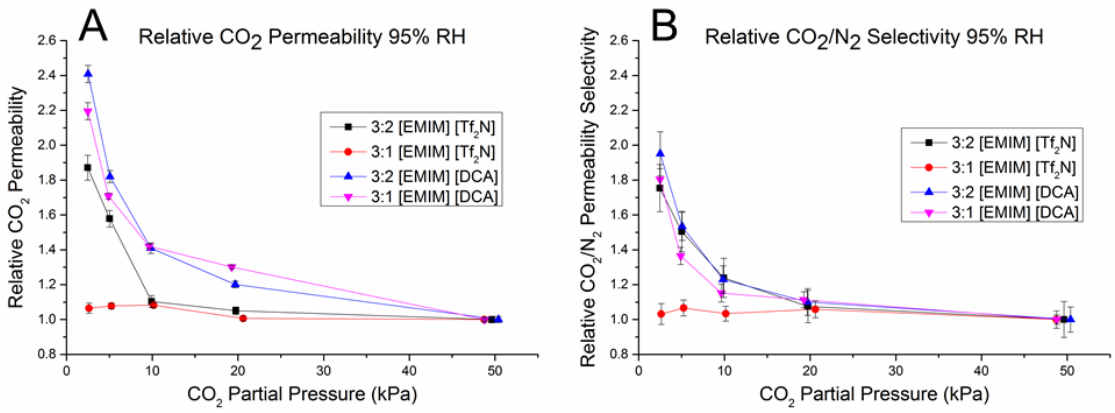


**Figure 10:** Effect of $CO_2$ partial pressure on A) the relative $CO_2$ permeability and B) the relative $CO_2/N_2$ permeability selectivity at 95% RH for the epoxy-amine ion gel membranes studied. The permeability and selectivity values are normalized to their values at 50 kPa $CO_2$ partial pressure in the feed.

The onset of $CO_2$ facilitated transport occurs at higher $CO_2$ partial pressures for the [EMIM] [DCA]-containing membranes compared to the 3:2 [EMIM] [$Tf_2N$] membrane (20 kPa vs. ~10 kPa). These concentrations are within the typical range for post-combustion flue gas streams. Therefore, assuming these systems are stable to the contaminants in flue gas, we can expect the performance of these membranes in flue gas to be comparable or better than observed under dry single-gas testing conditions.

### 3.2.2.3 Effect of $CO_2$ partial pressure on dry mixed-gas permeation studies

It was suggested in Sections 3.2.2.1 and 3.2.2.2 that a threshold amount of RH is required to facilitate $CO_2$ transport in the 3:2 [EMIM] [$Tf_2N$] membranes. We anticipated that a similar threshold is necessary for 3:2 [EMIM] [DCA] membranes. To test this hypothesis, a 3:2 [EMIM]

[DCA]-containing membrane was tested over the same feed $CO_2$ partial pressure range without water vapor (Figures 10A and 10B). Under dry conditions, the [EMIM] [DCA]-containing membrane does not display evidence of the facilitated transport of $CO_2$. Therefore, it is clear that water vapor is necessary to observe facilitate transport with either [EMIM] [DCA] or [EMIM] [$Tf_2N$]-containing epoxy-amine ion gel membranes.

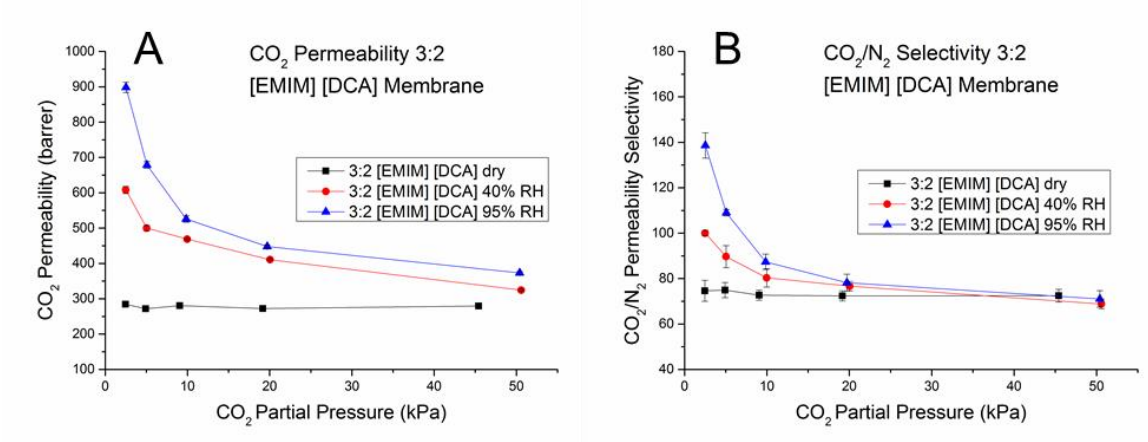


**Figure 11:** Effect of $CO_2$ partial pressure on A) the $CO_2$ permeability and B) the $CO_2/N_2$ selectivity for 3:2 [EMIM] [DCA]-containing membranes with dry, mixed-gas $CO_2/N_2$ feeds compared to values at 40% and 95% RH.

### 3.3 Discussion of the effect of free RTIL on permeation data

The results in Section 3.2 demonstrate that the free RTIL component has a significant effect on the $CO_2$ permeability and $CO_2/N_2$ separation performance of the facilitated transport membranes. Table 1 compiles the facilitation factors for both $CO_2$ permeability and $CO_2/N_2$ selectivity for the epoxy-amine ion gel membranes. We observed that membranes containing the hydrophilic [EMIM] [DCA] show facilitated transport of $CO_2$ at both 40% and 95% RH whereas the more hydrophobic [EMIM] [$Tf_2N$] does not. We attribute this to higher water content in the [EMIM] [DCA] membranes, allowing the reactions between amine and $CO_2$ to occur and resulting

in the facilitated transport of $CO_2$. This result suggests that hydrophilic RTILs will be useful for enhancing facilitated transport to separations in which the feed stream has relatively low RH.

**Table 4:** Tabulated facilitation factors for $CO_2$ permeability and $CO_2/N_2$ selectivity for the 4 epoxy-amine ion gel membranes at 95% RH and 2.5 kPa $CO_2$ partial pressure.

| Membrane | $CO_2$ Permeability Facilitation Factor | $CO_2/N_2$ Selectivity Facilitation Factor |
|---|---|---|
| **3:1 [EMIM] [$Tf_2N$]** | 1.06 | 1.03 |
| **3:2 [EMIM] [$Tf_2N$]** | 1.87 | 1.75 |
| **3:1 [EMIM] [DCA]** | 2.20 | 1.80 |
| **3:2 [EMIM] [DCA]** | 2.41 | 1.95 |

Control ion gel membranes were prepared and tested with either 75 wt. % [EMIM] [$Tf_2N$] or [EMIM] [DCA] with a poly(RTIL) network that does not contain amine functional groups (see Figure S2 in the Supporting Information).[14] The transport data for these membranes tested at 95% RH are displayed in Figures S3 and S4 in the Supporting Information. The $CO_2$ permeability of the control membrane no amines containing [EMIM] [DCA] increased by a factor of 1.3 with decreasing $CO_2$ partial pressure. However, the $CO_2/N_2$ selectivity of this membrane remained constant. This result suggests that water swells the membrane and acts as an equally selective $CO_2$ plasticizer. Therefore, we can attribute the $CO_2/N_2$ selectivity increases for the epoxy-amine ion gel membranes to the presence of amines in these networks, while $CO_2$ permeability is affected by both polymer network and free RTIL contributions.

### 3.4 Discussion of the effect of epoxy-amine stoichiometry

The epoxy-amine monomer ratio determines the nature of amines present in the membrane and is affects the facilitated transport through these systems. The 3:2 [EMIM] [DCA]-containing membrane has higher facilitation factors than the 3:1 [EMIM] [DCA] membrane at 95% RH (i.e., 2.41 vs. 2.20 for $CO_2$ permeability and 1.95 vs. 1.80 for $CO_2/N_2$ selectivity). This result suggests

that lower-order amines in the membrane are better at the facilitating transport of $CO_2$ under the conditions tested.

A more significant difference was seen for the [EMIM] [$Tf_2N$]-containing membranes. No evidence of facilitated transport was observed at 40% RH. However, at 95% RH, the 3:2 [EMIM] [$Tf_2N$] membrane displays transport behavior consistent with the facilitated transport of $CO_2$. This resulted the enhancement of $CO_2$ permeability by a factor of 1.87 (i.e., 200 to 380 barrer) with decreasing $CO_2$ partial pressure (from 50 to 2.5 kPa). Concurrently, the $CO_2/N_2$ selectivity of this membrane increased from 42 to 74, a factor of 1.75. In contrast, the $CO_2$ permeability and $CO_2/N_2$ selectivity values of the 3:1 [EMIM] [$Tf_2N$] membrane varied less than 10 % over the same $CO_2$ partial pressure range. Combined with the result from the [EMIM] [DCA] membranes, the gas transport data suggest that lower-order amines in the epoxy-amine ion gels are better at enhancing $CO_2$ transport under the conditions studied.

### 3.5 Comparison to ideal data and Robeson plot

In order to visualize and compare the data presented in this study to data previously reported for epoxy-amine membranes,[15] a Robeson plot has been prepared and is included as Figure 11. The $CO_2/N_2$ separation data of membranes containing 50, 60, and 75 wt. % [EMIM] [$Tf_2N$] under ideal conditions are displayed as triangles.[15] The data from the humidified mixed-gas permeation tests conducted in this work are included on the Robeson plot as squares. All of the epoxy-amine membranes have performance near or above the 2008 $CO_2/N_2$ Robeson upper bound.

As seen in Figure 11, as the partial pressure of $CO_2$ decreases and RH increases, the data progresses toward the upper right corner of the $CO_2/N_2$ Robeson plot, as both $CO_2$ permeability and selectivity increase due to facilitated $CO_2$ transport. Therefore, facilitated transport is an

effective mechanism for "overcoming" the limitations of the permeability-selectivity trade-off for polymer membranes represented by the Robeson upper-bound relationship.

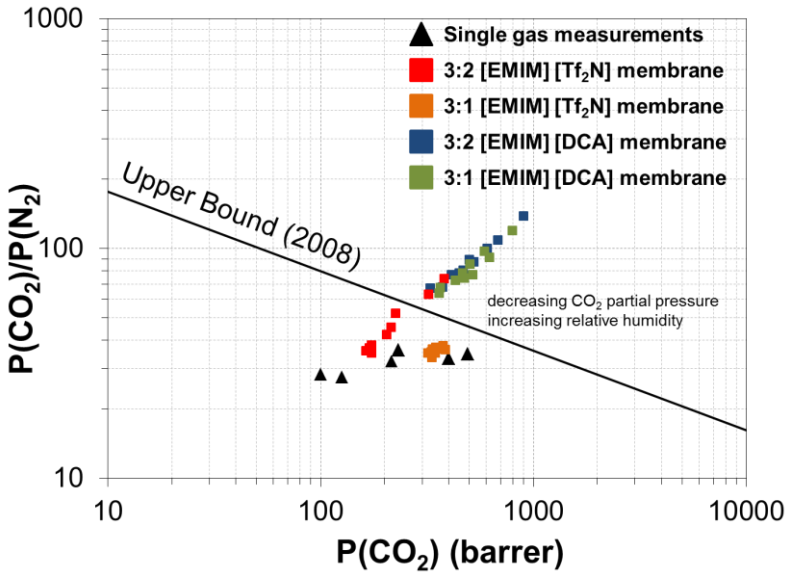


**Figure 12:** $CO_2/N_2$ Robeson plot with data for epoxy-amine ion gels tested in this study with humidified mixed-gas feeds (□) compared to previously reported single gas data (▲).[15] It should be noted that Robeson plots are typically used to compare materials tested under ideal (i.e., single-gas) conditions.

## 4. Conclusions

The fixed-site-carrier facilitated transport of $CO_2$ is possible with RTIL-based step-growth epoxy-amine ion gel membranes. When added to these ion gel membranes, the hydrophilic RTIL, [EMIM] [DCA], was found to require a lower RH to facilitate $CO_2$ transport than the hydrophobic RTIL, [EMIM] [$Tf_2N$]. Permeation behavior consistent with facilitated transport was observed over the same $CO_2$ partial pressure range for both [EMIM] [DCA] and [EMIM] [$Tf_2N$]-containing membranes. This work demonstrates that RTIL-based epoxy-amine ion gel membranes are capable of facilitated $CO_2$ transport at feed $CO_2$ partial pressures less than 20 kPa. The membranes reported herein achieved permeability selectivity above the 2008 Robeson upper bound and are attractive

candidates as $CO_2/N_2$ separation materials, especially where the target gas streams contain water vapor and low $CO_2$ concentrations. To further develop this work, future studies will focus on investigating the effect of temperature on the facilitated transport of $CO_2$ through these materials and the ability to process these materials into thin films.

## 5. Author Information

(D.L.G)* Corresponding author at: Department of Chemical and Biological Engineering, and Department of Chemistry and Biochemistry, University of Colorado, University of Colorado, CO 80309, United States. Tel.: +1 303 492 7640. E-mail address: douglas.gin@colorado.edu

(R.D.N)* Corresponding author at: Department of Chemical and Biological Engineering, University of Colorado, University of Colorado, CO 80309, United States. Tel.: +1 303 492 6100. E-mail address: nobler@colorado.edu

## 6. Acknowledgments

The authors gratefully acknowledge financial support from Total S.A. (France) for this work. We also thank Dr. A. L. Miller for synthesizing the [EMIM] [DCA] and Prof. H. H. Funke for assistance with the mixed-gas permeation apparatus.

## 7. Supporting information

A schematic of the mixed-gas permeation apparatus is included in the supporting information as well as relative permeability and relative $CO_2/N_2$ permeability selectivity data for the varying RH and $CO_2$ partial pressure experiments.

## 8. References

1. Ansolobehere, S.; Beer, J.; Deutch, J.; Ellerman, D.; Friedmann, J.; Herzog, H.; Jacoby, H.; Joskow, P.; McRae, G.; Lester, R.; Moniz, E.; Steinfeld, E.; Katzer, J. *The Future of Coal: Options for a Carbon-constrained World*; MIT: Cambridge, MA, 2007.

2. Figueroa, J. D.; Fout, T.; Plasynski, S.; McIlvried, H.; Srivastava, R. D. Advances in $CO_2$ capture technology—The U.S. Department of Energy's Carbon Sequestration Program. *Int. J. Greenh. Gas Control* **2008,** *2* (1), 9-20.

3. Aaron, D.; Tsouris, C. Separation of $CO_2$ from Flue Gas: A Review. *Sep. Sci. Technol.* **2005,** *40* (1-3), 321-348.

4. Kenarsari, S. D.; Yang, D.; Jiang, G.; Zhang, S.; Wang, J.; Russell, A. G.; Wei, Q.; Fan, M. Review of recent advances in carbon dioxide separation and capture. *RSC Adv.* **2013,** *3* (45), 22739-22773.

5. Merkel, T. C.; Lin, H.; Wei, X.; Baker, R. Power plant post-combustion carbon dioxide capture: An opportunity for membranes. *J. Membr. Sci.* **2010,** *359* (1–2), 126-139.

6. Brunetti, A.; Scura, F.; Barbieri, G.; Drioli, E. Membrane technologies for $CO_2$ separation. *J. Membr. Sci.* **2010,** *359* (1–2), 115-125.

7. Baker, R. W. *Membrane Technology and Applications*; *2nd ed.*; John Wiley & Sons: West Sussex, England, 2004.

8. Freeman, B. D. Basis of Permeability/Selectivity Tradeoff Relations in Polymeric Gas Separation Membranes. *Macromolecules* **1999,** *32* (2), 375-380.

9. Robeson, L. M. Correlation of separation factor versus permeability for polymeric membranes. *J. Membr. Sci.* **1991,** *62* (2), 165-185.

10. Robeson, L. M. The upper bound revisited. *J. Membr. Sci.* **2008,** *320* (1–2), 390-400.

11. Cadena, C.; Anthony, J. L.; Shah, J. K.; Morrow, T. I.; Brennecke, J. F.; Maginn, E. J. Why Is $CO_2$ So Soluble in Imidazolium-Based Ionic Liquids? *J. Am. Chem. Soc.* **2004,** *126* (16), 5300-5308.

12. Finotello, A.; Bara, J. E.; Camper, D.; Noble, R. D. Room-Temperature Ionic Liquids: Temperature Dependence of Gas Solubility Selectivity. *Ind. Eng. Chem. Res.* **2007,** *47* (10), 3453-3459.

13. Li, P.; Pramoda, K. P.; Chung, T.-S. $CO_2$ Separation from Flue Gas Using Polyvinyl-(Room Temperature Ionic Liquid)–Room Temperature Ionic Liquid Composite Membranes. *Ind. Eng. Chem. Res.* **2011,** *50* (15), 9344-9353.

14. Carlisle, T. K.; Nicodemus, G. D.; Gin, D. L.; Noble, R. D. $CO_2$/light gas separation performance of cross-linked poly(vinylimidazolium) gel membranes as a function of ionic liquid loading and cross-linker content. *J. Membr. Sci.* **2012,** *397–398*, 24-37.

15. McDanel, W. M.; Cowan, M. G.; Carlisle, T. K.; Swanson, A. K.; Noble, R. D.; Gin, D. L. Cross-linked ionic resins and gels from epoxide-functionalized imidazolium ionic liquid monomers. *Polymer* **2014,** *55* (16), 3305-3313.

16. McDanel, W. M.; Cowan, M. G.; Barton, J. A.; Gin, D. L.; Noble, R. D. Effect of Monomer Structure on Curing Behavior, $CO_2$ Solubility, and Gas Permeability of Ionic Liquid-Based Epoxy–Amine Resins and Ion-Gels. *Ind. Eng. Chem. Res.* **2014**, Article ASAP.

17. Gu, Y.; Lodge, T. P. Synthesis and Gas Separation Performance of Triblock Copolymer Ion Gels with a Polymerized Ionic Liquid Mid-Block. *Macromolecules* **2011,** *44* (7), 1732-1736.

18. Jansen, J. C.; Friess, K.; Clarizia, G.; Schauer, J.; Izák, P. High Ionic Liquid Content Polymeric Gel Membranes: Preparation and Performance. *Macromolecules* **2011,** *44* (1), 39-45.

19. Friess, K.; Jansen, J. C.; Bazzarelli, F.; Izák, P.; Jarmarová, V.; Kačírková, M.; Schauer, J.; Clarizia, G.; Bernardo, P. High ionic liquid content polymeric gel membranes: Correlation of membrane structure with gas and vapour transport properties. *J. Membr. Sci.* **2012,** *415–416* (0), 801-809.

20. Scovazzo, P. Determination of the upper limits, benchmarks, and critical properties for gas separations using stabilized room temperature ionic liquid membranes (SILMs) for the purpose of guiding future research. *J. Membr. Sci.* **2009,** *343* (1–2), 199-211.

21. Zhou, J.; Mok, M. M.; Cowan, M. G.; McDanel, W. M.; Carlisle, T. K.; Gin, D. L.; Noble, R. D. High-Permeance Room-Temperature Ionic-Liquid-Based Membranes for $CO_2/N_2$ Separation. *Ind. Eng. Chem. Res.* **2014,** *53* (51), 20064-20067.

22. Cussler, E. L. Facilitated and Active Transport. In *Polymeric Gas Separation Membranes*, Paul, D. R.; Yampol'skii, Y. P., Eds. CRC Press: Boca Raton, FL, 1994; pp 273-300.

23. Noble, R. D. Analysis of facilitated transport with fixed site carrier membranes. *J. Membr. Sci.* **1990,** *50* (2), 207-214.

24. Noble, R. D. Facilitated transport mechanism in fixed site carrier membranes. *J. Membr. Sci.* **1991,** *60* (2–3), 297-306.

25. Noble, R. D. Generalized microscopic mechanism of facilitated transport in fixed site carrier membranes. *J. Membr. Sci.* **1992,** *75* (1–2), 121-129.

26. Kim, T.-J.; Li, B.; Hägg, M.-B. Novel fixed-site–carrier polyvinylamine membrane for carbon dioxide capture. *J. Polym. Sci. B: Polym. Phys.* **2004,** *42* (23), 4326-4336.

27. Huang, J.; Zou, J.; Ho, W. S. Carbon Dioxide Capture Using a $CO_2$-Selective Facilitated Transport Membrane. *Ind. Eng. Chem. Res.* **2008,** *47* (4), 1261-1267.

28. Deng, L.; Kim, T.-J.; Hägg, M.-B. Facilitated transport of $CO_2$ in novel PVAm/PVA blend membrane. *J. Membr. Sci.* **2009,** *340* (1–2), 154-163.

29. Hussain, A.; Hägg, M.-B. A feasibility study of $CO_2$ capture from flue gas by a facilitated transport membrane. *J. Membr. Sci.* **2010,** *359* (1–2), 140-148.

30. Zhao, Y.; Ho, W. S. Steric hindrance effect on amine demonstrated in solid polymer membranes for $CO_2$ transport. *J. Membr. Sci.* **2012,** *415–416* (0), 132-138.

31. Caplow, M. Kinetics of carbamate formation and breakdown. *J. Am. Chem. Soc.* **1968,** *90* (24), 6795-6803.

32. Danckwerts, P. V. The reaction of $CO_2$ with ethanolamines. *Chem. Eng. Sci.* **1979,** *34* (4), 443-446.

33. Vaidya, P. D.; Kenig, E. Y. $CO_2$-Alkanolamine Reaction Kinetics: A Review of Recent Studies. *Chem. Eng. Technol.* **2007,** *30* (11), 1467-1474.

34. Li, Y.; Wang, S.; He, G.; Wu, H.; Pan, F.; Jiang, Z. Facilitated transport of small molecules and ions for energy-efficient membranes. *Chem. Soc. Rev.* **2015,** *44* (1), 103-118.

35. Kasahara, S.; Kamio, E.; Ishigami, T.; Matsuyama, H. Effect of water in ionic liquids on $CO_2$ permeability in amino acid ionic liquid-based facilitated transport membranes. *J. Membr. Sci.* **2012,** *415–416* (0), 168-175.

36. Kasahara, S.; Kamio, E.; Otani, A.; Matsuyama, H. Fundamental Investigation of the Factors Controlling the $CO_2$ Permeability of Facilitated Transport Membranes Containing Amine-Functionalized Task-Specific Ionic Liquids. *Ind. Eng. Chem. Res.* **2014,** *53* (6), 2422-2431.

37. MacFarlane, D. R.; Forsyth, S. A.; Golding, J.; Deacon, G. B. Ionic liquids based on imidazolium, ammonium and pyrrolidinium salts of the dicyanamide anion. *Green Chem.* **2002,** *4* (5), 444-448.

38. Merkel, T. C.; Gupta, R. P.; Turk, B. S.; Freeman, B. D. Mixed-gas permeation of syngas components in poly(dimethylsiloxane) and poly(1-trimethylsilyl-1-propyne) at elevated temperatures. *J. Membr. Sci.* **2001,** *191* (1–2), 85-94.

# Appendix B

The following report discusses synthesis and testing of multilayered dye-sensitized solar cells, which was the first research project I worked on in the Falconer/Noble lab. The following report is my Masters bypass paper for the chemical engineering department. The project involved building a solar simulator test system and learning how to construct standard solar cells with comparable quality to reports in the literature, before testing a variety of multilayer structures of dye-sensitized $TiO_2$ and conductive indium tin oxide, which had the potential to increase photocurrent by adsorbing a larger amount of light. Ultimately, we found that the novel structures tested could not produce significantly more power than the standard cells because of reduced open circuit voltage.

## $TiO_2$/ITO Layered Structure Dye-Sensitized Solar Cells


### Abstract

Dye sensitized solar cells (DSSCs) were constructed with multiple layers of mesoporous $TiO_2$ separated by a thin layer of porous indium tin oxide (ITO) particles. The ITO layer is in electrical contact with a dense ITO-coated glass slide, and acts to extend the electrode into the $TiO_2$. The ITO layer is porous to allow electrolyte to permeate though the internal $TiO_2$ layer. This structure allows for increasing the total $TiO_2$ thickness while maintaining a moderate electron diffusion distance to the nearest ITO contact point, either the internal layer or the conductive glass. By increasing the effective $TiO_2$ thickness more light can be absorbed, especially in the low-absorbance regions of the sensitizer dye, which can significantly increase short circuit current ($I_{sc}$).

When a 1 μm ITO layer was deposited between two 10 μm $TiO_2$ films on a dense ITO-glass substrate, the $I_{sc}$ was 20% larger than a standard cell with 10 μm $TiO_2$ on an ITO-glass substrate. The electrolyte/conductor contact in the porous ITO layer leads to electron/hole recombination, which causes the open circuit voltage ($V_{oc}$) to be 0.4V in the layered cell. A standard cell with only a dense ITO-glass contact has $V_{oc}$ of 0.7V. Passivation of the ITO particle layer by coating with $TiO_2$ was also studied. A 10-μm film of ITO nanoparticles was deposited on ITO-glass, and then atomic layer deposition (ALD) cycles were used to deposit a nanometer shell of $TiO_2$ throughout the film. DSSCs constructed with this core-shell architecture showed some increase in $I_{sc}$ over cells made with dyed, uncoated ITO particles, and the $V_{oc}$ increased from 0.22V to 0.4V. Depositing ALD coating of $TiO_2$ on layered cells to passivate the ITO layer may improve the layered cells' overall performance.

**Introduction**

Dye sensitized solar cells (DSSCs) are a potential alternative to the traditional solid state photovoltaic cell. They are thin film devices that may be produced from low cost materials in mass quantity. DSSCs are different from conventional PV devices in that the light absorption and charge transport functions are performed by separate material; in previous generations of solar cells, both processes occur in a bulk semiconductor layer. In the DSSC, photons are absorbed by sensitizer molecules that are chemically absorbed to the surface of a porous particle network. The most common sensitizers are Ruthenium-pyridine dyes, although other dyes can be used[1-3]. Because the absorption of a monolayer of dye is weak, films with roughness factors of 1000 are common in order to capture sufficient incident light. The particles that make up the high surface area film are

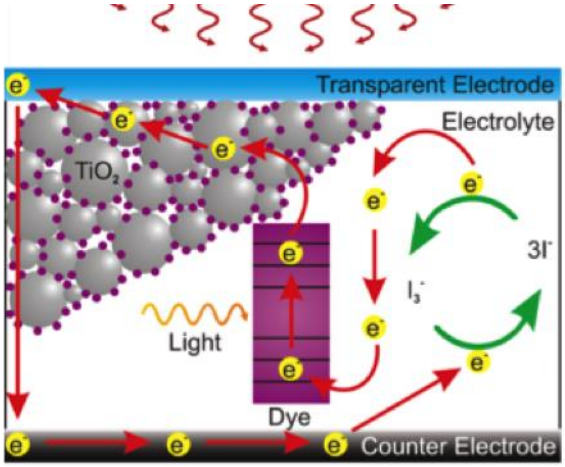


Figure 1

wide band gap semiconductors. $TiO_2$ is the most common material choice because it is stable, cheap, and the conduction band energy matches well with the dye injection energies[4,5]. Charge transfer occurs at the dye/particle interface through a bond to the semiconductor surface. Injected electrons must diffuse through the porous film before they are collected at the anode.

Researches have made incremental improvements to DSSCs since they were first reported by Gratzel[6] two decades ago. The highest published laboratory efficiency is 12.3% using a cobalt electrolyte[7], with typical $TiO_2$/iodine cells giving 4% – 10% efficiency depending on materials and construction. Several loss mechanisms prevent DSSCs from obtaining their theoretical maximum power output of 33%[8]: overpotential losses in the redox couple, internal resistance, incomplete light harvesting, and electron recombination.

Without the macroscopic charge gradient of bulk semiconductor/liquid junction interface, electron transport in the mesoporous $TiO_2$ film is described by random diffusion with characteristic diffusion length given by recombination rate (which depends on the surface coverage of the dye and ligands, and electrolyte kinetics) and electronic properties of the semiconductor[9]. For typical $TiO_2$ films, increasing the film thickness increases power output linearly from 0 to 10 μm, and maximum efficiency occurs around 15 μm[10]. This is due to the total film thickness exceeding the effective diffusion distance, which is about 10 to 15 μm[11], in thicker cells.

Attempts to improve electron transport by making structural changes to the semiconductor layer include incorporating small concentrations of carbon nanotubes[12], growing semiconductor nanowires[13], or coating areogels in $TiO_2$[14]. These approaches all involve modifying the entire semiconductor film. Our approach focuses on improving electron capture to reduce recombination by introducing an intermediate transparent conducing oxide layer into the $TiO_2$ film. Figure 2 depicts the anode of a layered DSSC. The porous ITO is in electrical contact with the ITO-glass substrate and acts as part of the electrode. This layered cell should increase the total effective $TiO_2$ thickness while simultaneously not increasing electron diffusion distance above 10 μm.

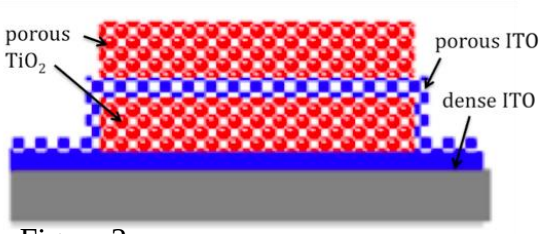

Figure 2

**Materials and Methods**

Glass coated with dense fluorine doped tin oxide (FTO) or indium tin oxide (ITO) (Aldrich) was used for the electrodes. A commercial dispersion of $TiO_2$ nanoparticles (Degussa P25 and Solaronix Ti-Nanoxide D) was applied by drawing the paste across ITO-glass with a razor blade. The glass was masked with clear adhesive tape. The anode was heated to 450°C for one hour to sinter the particles. The anode was then soaked in 0.5 mM dye solution (N719 dye from Everlight Chemical in pure ethanol) overnight. It was rinsed in pure ethanol for 30 s and then dried at 50°C. Before the dye soaking step, further layers of $TiO_2$ or porous ITO (30 wt% nanoparticle in isopropanol from Aldrich) could be added to make a layered cell.

Atomic layer deposition (ALD) was used to coat the ITO particle layer with a shell of $TiO_2$. First the ITO particles were spread on ITO-glass and sintered to make the film conductive. The anode was placed into an ALD reactor where ALD cycles deposited a conformal coating of $TiO_2$

of nanometer thickness. In a typical cycle precursor titanium isopropoxide was dosed to a pressure of 90 Pa; it reacted for 2 min; the system was vacuum pumped to 3 Pa, purged with $N_2$, and vacuum pumped again; then the same steps were repeated with 30 wt% $H_2O_2$ in water. The reaction was run at 100°C[15]. After the ALD the particles were sintered at 450°C for 1 hr to crystallize the amorphous $TiO_2$.

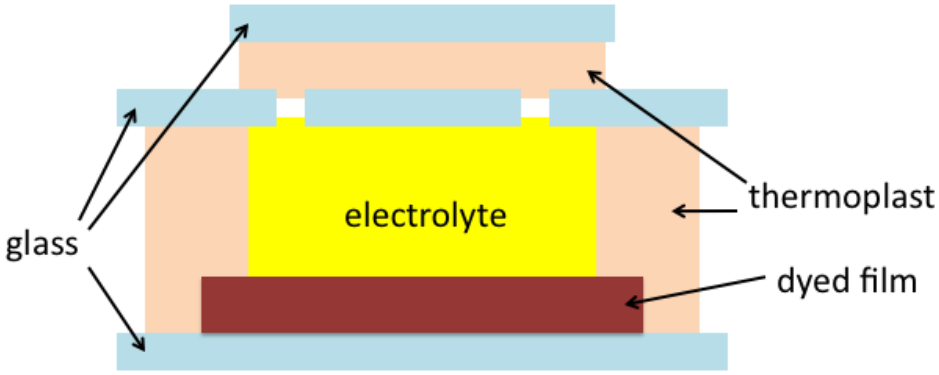


Figure 3

The counter electrode was made by drop coating $H_2PtCl_6$ on ITO-glass and heating in the oven at 400°C for 15 min. The electrolyte was 0.04 M $I_2$, 0.8 M LiI, and 0.2 M 4-tert-butylpyridine in acetonitrile. Two holes were drilled into the cathode. The dry anode and cathode were sealed together with a thermoplast (Meltonix from Solaronix) by heating and applying pressure, and then electrolyte was injected into the cavity. The thermoplast spaces a 60-µm gap between the glass slides. More thermplast was used to cover the holes with another piece of glass. A representation of a sealed DSSC is shown in figure 3.

Power curves were taken with an ABET 10500 solar simulator with AM1.5 spectrum sunlight and irradiance of 1000 $W/m^2$. The current voltage scan was done using a source meter (Pine 2200). Scanning electron microscope and transition electron microscope images were taken to observe porosity and ALD coating thickness. Profilometry gave total film thicknesses.

**Results and Discussion**

Figure 2 compares the layered cell with a standard cell. The standard cell has a 10 μm-thick film of mesoporous $TiO_2$ on an ITO-glass substrate. The layered cell has a 10-μm layer of $TiO_2$, a 1-μm layer of ITO, and another 10-μm layer of $TiO_2$ on an ITO-glass substrate. The data from figure 4 (a) were recorded by Dr. Miao Yu on a multimeter under roughly 500 W/m$^2$ illumination from a halogen lamp. The data from (b) we taken by Nicholas Chisholm on a labview-connected potentiometer under 1000 W/m$^2$ illumination from a solar simulator. The power curves indicate that more current is collected at short circuit from the layered cell than from the standard, but the mesoporous ITO layer causes a drop in the available electrical potential. The standard cell in figure 2 (b) has a maximum efficiency of about 0.9% and the layer cell has an efficiency of 0.3%.

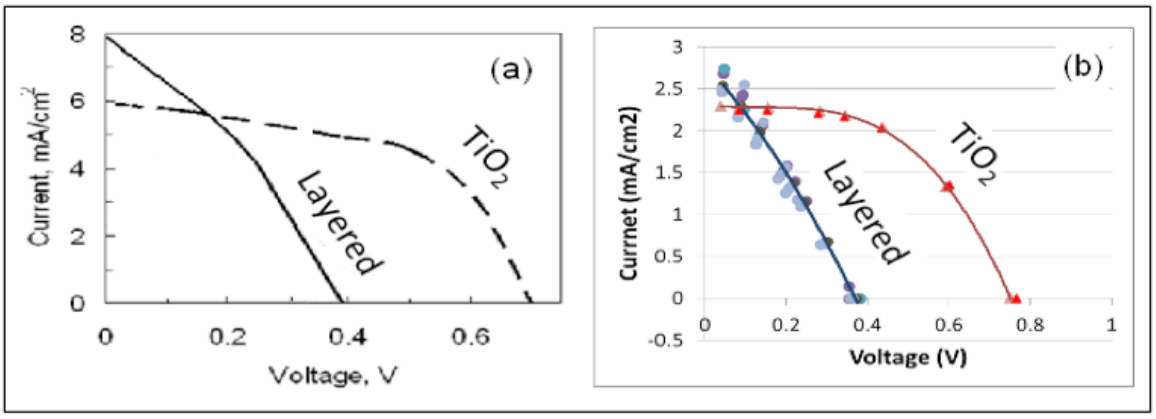


Figure 4 a) results by Dr. Miao Yu using a halogen lamp; b) results for Chisholm fall 2011 using solar simulator and applied resistances to measure data points.

Figure 5 shows cells consisting of a 10-μm thick ITO particle layer on ITO-glass. Zero to 200 ALD cycles were performed to grow conformal films of varied thickness and create so-called core-shell cells. Anodes made with a 50, 100, and 200-cycle ALD film on ITO gave higher open circuit voltage than the control, uncoated ITO with dye (labeled 0 cycles in figure 3). The maximum voltage is about 0.4 V, which is much lower than the voltage for a standard $TiO_2$ cell, 0.7 V. The

maximum efficiency for the 100-cycle cell is 0.1%. The thicker the $TiO_2$ film, the more the electronic properties will be like bulk $TiO_2$. However the coating thickness is limited by the pore size of the ITO film. In the figure, the current for the 200-cycle core-shell cells is low because the ALD-deposited $TiO_2$ closed off pores and little dye could be deposited. This was visually apparent; the 200-cycle film was yellowish after soaking in dye instead of the typical deep purple of a well-dyed film. It is not possible to passivate the ITO with ALD to the point that the core-shell structure gives a DSSC with the same open circuit voltage as generated by standard $TiO_2$ cells, but these results indicate an opportunity to improve on open circuit voltage of the layered cells via $TiO_2$ ALD.

The efficiencies of the cell discussed above are all less than 1%. In the literature, cells made from similar materials have significantly higher power output of at least 4%, and the control cells from our lab should be in that range. Since partway though the spring semester, the layered cells and ALD part of the project has been put on hold while improvements were made to the standard cells. Once these $TiO_2$/iodine cells are sufficiently improved, the experiments will be repeated with more variations on the layered structure.

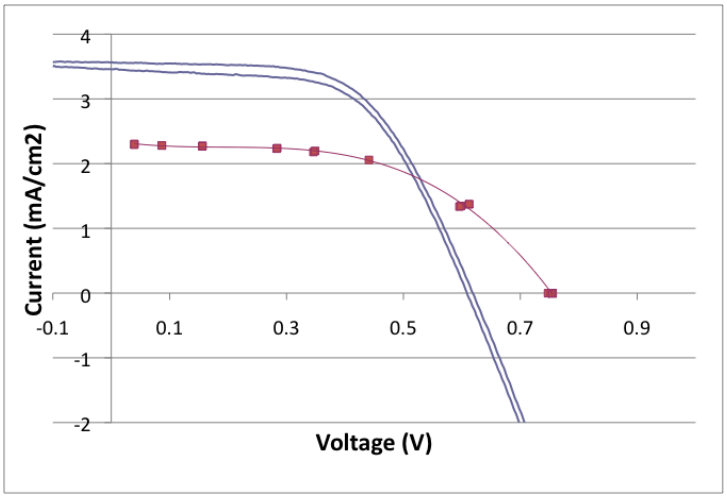

Figure 5

Several methods for creating anodes and constructing cells were attempted over the past few months with both failures and progress. A simpler form of sealing using a metal spacer with O-rings was abandoned because of internal resistance and leakage. The doctor blade method for

casting the $TiO_2$ was refined, but still needs some work to give reproducible film thicknesses. This may be accomplished by using larger area electrodes. The sealing process requires care and precise craftsmanship, which will improve with practice and new equipment.

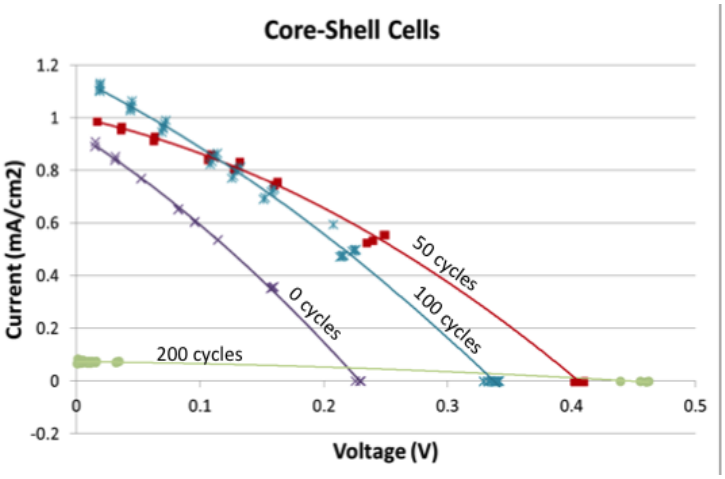


Figure 6

The best standard cell produced so far had an efficiency of 4.1%, which is a vast improvement over the previous cells. This cell is shown below with the standard cell from figure 2. The open circuit voltage of this cell is lower than previous cells, and deviation from cell to cell is still quite large – upwards of 40%. Present work has been to identify differences between good and poor cells that come from the same batch of anodes. Also, ways to standardize the fabrication process are being considered, such as buying a heat press to control heat and pressure during sealing, and vacuum filling with electrolyte to avoid air bubbles in the cell.

**Conclusions**

Though the preliminary results show that the layered structure is a potentially beneficial semiconductor film construct, these cells must be constructed and tested in the same manor that gave 4% efficiency for the standard cells. Most of the time since the spring semester has been testing new materials and methods to improve the base efficiency of standard cells to a level similar to literature values. Progress has been made toward this goal, but more consistency is needed before the previous work is repeated.

## References


1. Sun, Y., Onicha, A.C., Myahkostupov, M. & Castellano, F.N. Viable alternative to N719 for dye-sensitized solar cells. *ACS applied materials interfaces* **2**, 2039-2045 (2010).

2. Nazeeruddin, M.K. et al. Engineering of Efficient Panchromatic Sensitizers for Nanocrystalline TiO2-Based Solar Cells. *Journal of the American Chemical Society* **123**, 1613-1624 (2001).

3. Campbell, W.M. et al. Highly Efficient Porphyrin Sensitizers for Dye-Sensitized Solar Cells. *Journal of Physical Chemistry B* **111**, 11760-11762 (2007).

4. Gratzel, M. Dye-sensitized solar cells. *Journal of Photochemistry and Photobiology C Photochemistry Reviews* **4**, 145-153 (2003).

5. Sayama, K., Sugihara, H. & Arakawa, H. Photoelectrochemical properties of a porous Nb2O5 electrode sensitized by a ruthenium dye. *Chemistry of Materials* **10**, 3825-3832 (1998).

6. O'Regan, B. & Gratzel, M. A low-cost, high-efficiency solar cell based on dye-sensitized colloidal TiO2 films. *Nature* **353**, 737-740 (1991).

7. Yella, A. et al. Porphyrin-Sensitized Solar Cells with Cobalt (II/III)-Based Redox Electrolyte Exceed 12 Percent Efficiency. *Science* **334**, 629-634 (2011).

8. Snaith, H.J. Estimating the Maximum Attainable Efficiency in Dye-Sensitized Solar Cells. *Advanced Functional Materials* **20**, 13-19 (2010).

9. Benkstein, K.D., Kopidakis, N., Van De Lagemaat, J. & Frank, A.J. Influence of the Percolation Network Geometry on Electron Transport in Dye-Sensitized Titanium Dioxide Solar Cells. *The Journal of Physical Chemistry B* **107**, 7759-7767 (2003).

10. Section, E. & Tio, T. Dependence of TiO 2 Film Thickness on Photocurrent-Voltage Characteristics of Dye-Sensitized Solar Cells. *Notes* **25**, 742-744 (2004).

11. Nakade, S. et al. Dependence of TiO 2 Nanoparticle Preparation Methods and Annealing Temperature on the Efficiency of Dye-Sensitized Solar Cells. *The Journal of Physical Chemistry B* **106**, 10004-10010 (2002).

12. Lee, T., Alegaonkar, P. & Yoo, J. Fabrication of dye sensitized solar cell using TiO2 coated carbon nanotubes. *Thin Solid Films* **515**, 5131-5135 (2007).

13. Tan, B. & Wu, Y. Dye-sensitized solar cells based on anatase TiO2 nanoparticle/nanowire composites. *The Journal of Physical Chemistry B* **110**, 15932-15938 (2006).

14. Hamann, T.W., Martinson, A.B.F., Elam, J.W., Pellin, M.J. & Hupp, J.T. Atomic Layer Deposition of TiO2 on Aerogel Templates: New Photoanodes for Dye-Sensitized Solar Cells. *Journal of Physical Chemistry B* **112**, 10303-10307 (2008).

15. Ferguson, J.D., Yoder, A.R., Weimer, A.W. & George, S.M. TiO2 atomic layer deposition on ZrO2 particles using alternating exposures of TiCl4 and H2O. *Applied Surface Science* **226**, 393-404 (2004).

# Appendix C

Appendices C and D concern molecular layer deposition (MLD) to grow ultra-thin-film, high-flux membranes on microporous ceramic supports for small gas separations, which was another research project I worked on in the Falconer/Noble lab. This section is the final report to the MAST Center for project grant 13-4, and the next appendix is the last summary report to NSF on continuing work. MLD membranes were made by depositing several nm of dense aluminum alkoxide (from several chemistries) on zeolite membranes, $TiO_2$ nanowire sheets, and anodic alumina substrates (these supports were tested after the final MAST report was submitted) followed by calcination to remove the organic component and produce a porous film. The membranes we tested did not have ideal selectivities significantly different than Knudsen selectivity for a variety of small gases, and analysis of the films could not determine if defects were due to cracking or the native pore-size distribution of the films.

## MEMBRANE SCIENCE, ENGINEERING & TECHNOLOGY CENTER RESEARCH PROJECT PROGRESS FINAL REPORT

**PROJECT TITLE: A New Ceramic Membrane for Gas Separation and Organic Solvent Recovery**

**PROPOSAL: #: 13-4:**

**PROJECT INITIATION DATE: 10/12** **PERIOD OF THIS REVIEW: 5/14 – 10/14**

**PRINCIPAL INVESTIGATORS:** R. D. Noble, J.L. Falconer and H.H. Funke

**STUDENTS/RESEARCHERS:** Nicholas Chisholm

**PROJECT DESCRIPTION:** The goal of this proposed I/UCRC project is to develop a new category of ceramic membranes targeting two extremely important membrane markets - gas separation and organic solvent recovery. The membrane product will be thin inorganic membranes based on

metal-organic nanomaterials that are highly selective and have fluxes that are at least an order of magnitude higher than fluxes of previously-reported membranes.

Metal–organic nanomaterials (MON) are a novel class of functional nanomaterials used to fabricate nanostructures with various combinations of metals and organics. This new class of nanomaterials allows researchers to develop unique sensors, catalysts and separation membranes. Of particular interest is the ability to integrate metal-organic nanomaterials with support surfaces to produce useful products that utilize nanomaterial functional properties and have superior mechanical, chemical and thermal properties.

The proposed membrane will be fabricated by depositing a thin layer of metal-organic materials, dense or with pores less than 1nm, onto Novarials bendable ceramic nanowire membranes. The research program will consist of developing methods to form a robust MON coating, and to control and optimize the selectivity and permeation rate properties of the resulting membranes. The thin layer of ceramic materials will be prepared using molecular layer deposition (MLD) procedure developed at NSF MAST center at University of Colorado. During the process, thin, conformal, dense, metal-organic layers with various compositions will be firstly deposited onto our porous support membranes and then converted into dense or small pore membranes by calcination.

Molecular layer deposition can form ultrathin layers of inorganic-organic hybrid materials on a variety of substrates. The layers are produced by sequentially conducting a series of half-reactions at the surface of a substrate

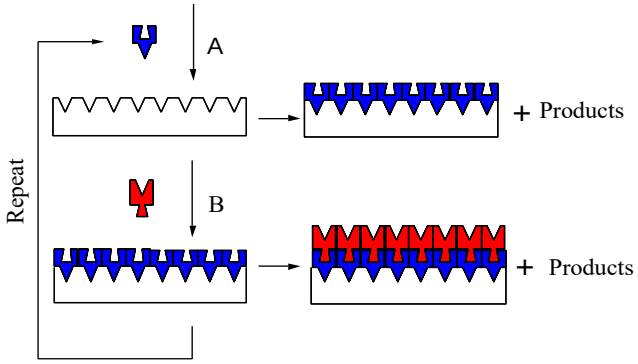


Fig. 1 Conceptual schematic of MLD half reactions.

(shown schematically in Fig. 1). Each set of half-reactions deposits a layer that conforms to the surface of the underlying substrate. A layer of any thickness can be deposited by repeating the reaction sequence. The film thickness can be controlled at the sub-nanometer level because each half reaction is self-limiting. *This is a significant advantage over other methods to form ultrathin films that are defect free.*

Molecular layer deposition has been used to form thin film coatings on nonporous nanoparticles. Figure 2 shows a scanning transmission electron microscopy (STEM) image of a spherical, nonporous silica particle coated with a conformal aluminum alkoxide (alucone) film that was formed by 50 MLD cycles at 373 K. The film was 25 ± 0.5 nm thick, which represents a growth rate of ~0.50 nm per cycle. Alucone films were also coated on titania and silica nanoparticles using alternating reactions of trimethylaluminium (TMA) and ethylene glycol in a fluidized bed reactor. In these reactions, surface OH groups react with TMA in the first step:

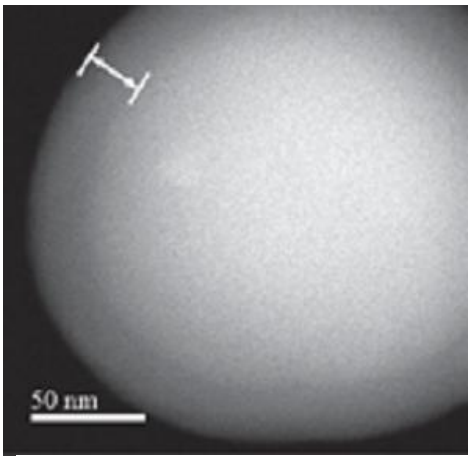


**Fig. 2** STEM image of alucone MLD-coated, 250-nm silica particles after 50 cycles at 100

$$-OH + Al(CH_3)_3 \rightarrow -O-Al(CH_3)_2 + CH_4\ (g)$$

The surface sites containing $Al(CH_3)_2$ then react with ethylene glycol:

$$-O-Al(CH_3)_2 + 2\ HOC_2H_4OH \rightarrow -O-Al((OC_2H_4OH)_2 + 2\ CH_4\ (g)$$

The remaining OH groups are then available to react with TMA to deposit additional Al and this sequence of self-limiting reactions can build up multilayers.

The MLD layer thickness is determined by the number of MLD cycles and can be precisely controlled because the reactions are self-limiting. The alucone layers prior to oxidation are not porous, but they can be oxidized to form a porous layer. The layer can be made porous by mild water etching at room temperature or by calcination in air at elevated temperatures. Because of the layer-by-layer growth process, the deposited MLD hybrid films have a regular structure, and oxidation of these hybrid films produces interconnected, highly-porous structures with small pores and high surface area. These proposed membranes have a number of advantages over other types of membranes, including exquisite control of the membrane properties. Because many oxides/nitrides can be formed and different organic precursors can be used, the pore sizes and size distributions and the chemical properties of the membranes can potentially be controlled.

Novarials ceramic membranes are made by a simple wet lay process using Novarials advanced ceramic nanowires. Unlike the usual bulky ceramic monolith supports, these are manufactured as thin sheets and can be manipulated to produce compact membrane modules with high area to volume ratios.

The importance of the support should be recognized. Not only does the support have to have chemical, thermal and physical properties sufficiently robust to withstand use conditions for a length of time, which may be on the order of years, but other properties are important for optimal membrane formation. The support pore size cannot be too large or the thin layer will tend to break through. A rule of thumb used in composite membranes is that the support pore size should be no larger than the coating thickness. On the other hand, too small a pore size will retard productivity. A high support surface porosity is desired to increase permeation. Defects and surface roughness must of course be controlled to minimize defects during coating formation, and to allow thinner coatings to be used. In addition, chemical compatibility between

the coating and the support is necessary to obtain good bonding, and in applications at high temperatures, it may be necessary to match thermal expansion properties.

**RESEARCH PLAN:** Deposition process is outlined above. After calcination of the alucone layer the membranes will be mounted into two-gas permeation systems to determine selectivity and permeances for combinations of $N_2$, $H_2$, $CH_4$, $CO_2$.

**PREVIOUS RELATED WORK:** In a previous study microporous alumina thin films were grown via MLD on SAPO-34 zeolite membranes which improved selectivity for hydrogen gas separations dramatically.[1] The SAPO-34 membranes were hydrothermally grown on commercial supports in our lab and had a $H_2/N_2$ selectivity of 8 and a $H_2/CO_2$ selectivity of about 2. As described above, a conformal MLD film was grown on the zeolite by alternate dosing of TMA and ethylene glycol. The MLD layer was then oxidized to leave a 10nm microporous coating on the zeolite surface. Figure 3 shows a schematic of the MLD process and an SEM cross-section of the composite membrane. These composite membranes were highly selective for $H_2/N_2$ separations even at elevated temperature and pressure. The $H_2/N_2$ selectivity was 580 at 0.33MPa and 400K with the selectivity increasing to 1040 at 1 MPa and 400K. The selectivity for $H_2/CO_2$ was about 20 for the composite membrane. The selectivity for $H_2/CO_2$ was significantly lower indicating MLD pore sizes between the kinetic diameter of $N_2$ and $CO_2$. The increase in $H_2$ selectivity after alumina deposition occurs either because the pores in the alumina layer are less than .36nm or the alumina slightly narrowed the SAPO-34 pores which are nominally .38nm.

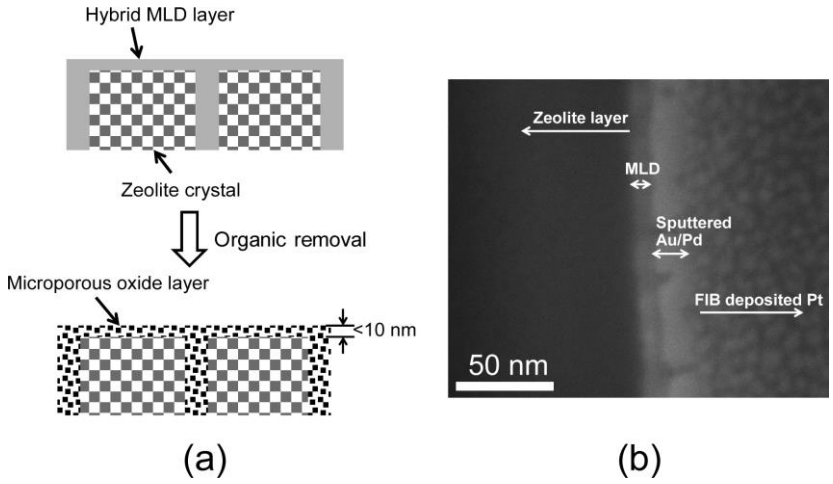


Figure 3 (a) Schematic illustration of the inorganic composite membrane preparation process. The hybrid material is first deposited on and between zeolite crystals, and subsequent removal of the organic component generates a porous composite membrane. (b) FIB SEM image showing a cross section of a SAPO-34 zeolite layer coated with an MLD layer.

**RELATED MAST CENTER RESEARCH: None applicable**

**WHY THE CURRENT RESEARCH IS DIFFERENT AND IMPORTANT:** High-flux, high-selectivity ceramic membranes would be valuable in numerous applications. The pore sizes would need to be tuned for specific gas compositions, but this work is in H2/N2 separation as a proof of concept.

**DISCLOSURE HISTORY AND PLANS: None**

**BUDGET HISTORY & CURRENT ACCOUNT BALANCE: Not applicable**

**IAB INTERACTION HISTORY: None**

**POTENTIAL BENEFIT TO MEMBRANE COMPANIES:** The combined U.S. market for membranes used in liquid and gas separating applications is estimated at approximately $1.7 billion in 2010, and is forecast to grow at a compound annual growth rate (CAGR) of 6.9% during the 5-year forecast period to reach $2.3 billion in 2015.

By one estimate, the separation of nitrogen from air, carbon dioxide from methane, and hydrogen from nitrogen, argon, or methane comprises about 90% of gas separation membrane applications. However, the development of suitable membranes will uncover a large potential market for membrane gas separation in refineries. Challenging separations of hydrogen/hydrocarbon and olefin/paraffin, as well as olefin/parafin separations are available to the developer of a proper membrane. High temperature hydrogen separations nowadays require platinum or palladium coated metal tubes. A compact ceramic membrane system for this application would revolutionize this business.

There are many solvent separation processes that cannot be addressed with current polymeric RO or nanofiltration membranes. A sturdy ceramic nanofilter having a small footprint would be readily accepted in pharmaceutical and biotech manufacturing industries.

The proposed new category of ceramic membranes, if successfully developed, will have significant impacts on the engineering of current gas separation and organic solvent recovery processes. It can be expected that incorporation of such novel membranes will reduce waste and increase sustainability in the chemical, petroleum and pharmaceutical industries.

**SUMMARY OF RESULTS DURING THIS REVIEW PERIOD:** Due to problems with the MLD reactor detailed in the last report (MAST report September 2013), the reactor system was rebuilt. The pneumatic control valves were replaced with high-temperature versions so that the lines could be heated to 100 C up from 60 C. The metal lines were cleaned by soaking in 2M NaOH for two days to dissolve any metal-oxide build-up inside them. Molecular sieve beads were heated then added to the ethylene glycol precursor to remove trace amounts of water, and the glycol was vacuum distilled when it was connected to the reactor lines.

MLD films were grown on silicon wafers and XRR was used to determine film thickness and density. The measured film after 25 cycles had a thickness of 12nm and density of 1.8g/cm$^3$ which matches reported literature values for alucone growth. This along with mass spectrometer readings during reaction cycles, indicate that the reactor system is properly growing alucone.

Zeolite support

MLD was performed on SAPO-34 tube membranes. The membranes were wrapped in Teflon tape to prevent deposition on the outside of the support and placed in our static dose reactor. Reactions were run at 100C with 2 minute precursor dose times, a nitrogen purge, and 10 minute evacuations down to <0.02 torr.

During membrane testing the flow meters were recalibrated and the gas chromatograph peak area correlation was recalculated. The mass balance was closed to 95%. Several of the tested membranes showed poor selectivity after MLD coating and calcination. These were shown to flow single gas isobutane. Because isobutane does not flow through uncoated zeolite, these membranes somehow became defective after being put into the reactor. We do not have an explanation for what happened to these membranes (RF237 and RF250 below).

After calcination at 100C membrane RF80 showed a $H_2/N_2$ selectivity of 150 at 20 C for a feed pressure of 380 kPa and permeate pressure of 83 kPa. The $H_2$ permeance was about $7*10^{-8}$ mol/m$^2$sPa and $N_2$ permeance was about $4.5*10^{-10}$. This selectivity is better than what was previously reported in 2011 (M1 and M2) while the permeance is higher. Membrane RF82 also performed better than previous membranes at room temperature.

These membranes became selective after calcination as low as 100C – much lower than previously reported. Because the first membrane (RF82) showed a drop in selectivity when heated

to 250 C it was hypothesized that the pore structure changes with subsequent oxidations at higher temperature. XRR on oxidize films also shows that density and thickness can change with heating. We made several more membranes and tested performance after heating to higher and higher final oxidation temperatures. There is a general trend of high selectivity and permeance after the initial oxidation after which the selectivity drops sharply somewhere between 100C and 250C. It was expected that a change in MLD pore structure that would cause this sharp drop in selectivity would occur over a much narrower temperature range so there may be another effect at play. Thermal cycling could cause cracks to from in the MLD layer or a high temperature could cause the MLD layer to restructure, shrinking and cracking.

| Membrane | H2/N2 selectivity | H2 Permeance ($mol/m^2 s Pa$) | Oxidation Temperature |
|---|---|---|---|
| **M1*** | 75 | $2.5*10^{-8}$ | 300 C |
| **M2*** | 125 | $3.0*10^{-8}$ | 300 C |
| **100*** | 5.4 | $3.0*10^{-7}$ | 300 C |
| **RF241** | 25 | $2.7*10^{-8}$ | 200 C |
| **RF82** | 150 | $9.7*10^{-8}$ | 200 C |
| **RF82** | 18 | $3.5*10^{-7}$ | 250 C |
| **RF237** | ~1 | | uncalcined |
| **RF250** | ~1 | | uncalcined |
| **RF80** | 145 | $8.6*10^{-8}$ | 100 C |
| **RF80** | 145 | $7.0*10^{-8}$ | 125 C |
| **RF80** | 150 | $3.6*10^{-8}$ | 150 C |
| **RF83** | 60 | $7.8*10^{-8}$ | 50 C |
| **RF83** | 90 | $1.8*10^{-8}$ | 100 C |

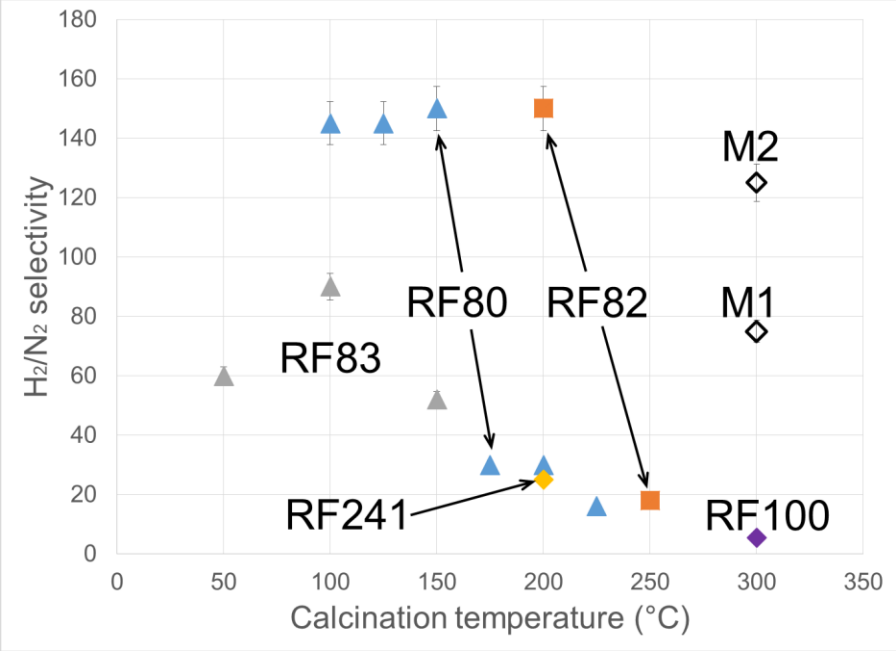


**Fig. 4** Hydrogen/nitrogen selectivity for several composite MLD-alumina/SSZ-13 membranes after calcination at different temperatures.

We know from previous experiments the zeolite support may crack above 350C but this may not be the case for MON supports. We also observe a decrease in $H_2$ permeance after repeated oxidations which could mean pores are closed off due to film shrinking and becoming more dense.

Novarials Support

The main goal of this project is a develop a selective but very high flux membrane. We have studied composite MLD-zeolite membranes because they are a simpler system because the MLD precursors do not fit in the zeolite pores. The Novarials ceramic nanowire material (MON) is more desirable as a support than zeolite because it has larger pore size and should give much higher fluxes. Even though it is theoretically a good support, there are physical and practical limitations to using this particular substrate.

We have developed a procedure for mounting the brittle, paper-like material on porous alumina frits with high-temperature epoxy that can withstand heating to 200 C. The epoxy and hardener are mixed then heated to 80 C for 10 minutes to harden into a viscous state. This helps prevent the epoxy from wicking into pores. Some if the membranes are damaged by handling during the epoxy mounting and must be discarded. Other membranes have most of the membrane area covered in epoxy because it flows into the porous film even after thickening the epoxy. Fewer than 20% of membranes are usable after mounting in this method. Once the MON is mounted the whole piece is placed into the reactor for 300 cycles of MLD growth. After reaction more epoxy is applied to ensure a seal. Initial experiments showed leaks in the membrane system. It was not clear whether the leaks were due to incomplete sealing by the epoxy or defects in the membrane.

We have made one membrane that holds pressure in our single gas flow system. We made single gas flux measurements for the fours gases listed. The data is presented below in the form of ideal selectivities and these are compared to Knudsen selectivity.

| Gas pair | H2/N2 | H2/CH4 | H2/CO2 | N2/CH4 | CH4/CO2 | N2/CO2 |
|---|---|---|---|---|---|---|
| Ideal Novarials Selectivity | 3.5 | 2.8 | 4.7 | 1.3 | 1.7 | 1.3 |
| Knudsen Selectivity | 3.7 | 2.8 | 4.7 | 1.1 | 1.7 | 1.2 |

The $H_2/N_2$ selectivity of 3.5 is comparable to that in unmodified SAPO-34 zeolite. We have not achieved the separation possible in the case of a uniform MLD film, as shown on zeolite, of >100. We expect that film shrinkage during the oxidation step causes cracking the MLD layer. The permeance is estimated to be about 2 orders of magnitude higher than in our composite MLD-zeolite membranes, but it is hard to determine the active membrane surface area because of

coverage by epoxy. This membrane may be useful for ultrafiltration purposes but we are not equipped in lab to test it in that capacity.

We ran a series of reaction/oxidation cycles in an attempt to make a new membrane that has a complete MLD layer with no cracking. The idea is to fill in pores and cracks that form in the relatively thick MON layer by growing a second, third, or fourth layer after each oxidation. These experiments did not yield any membranes that had higher than Knudsen selectivity.

We mounted the Novarials film in a HPLC filter gasket to see if that system would work better than the expoxy/frit one, but all membranes mounted this way tore open during testing. Even with a metal backing on the low pressure side, the membranes could not hold 20 psi of pressure.

We believe that the pore size of the MON substrate for MLD composite high-flux ceramic membranes should be in the range of 5nm to 50nm. On the few membranes that made it to testing, we never observed completely blocked pores. For a good membrane, there should be minimal gas flow after the dense MLD film is grown and selective flow after calcination opens up pores. Even after days of reactor growth we were not able to close off the pores of the Novarials material.

We have unfortunately concluded that this material is a poor substrate for making MLD films for gas separations. It is difficult to seal into a membrane module because it is brittle and prone to cracking when bent, there must be a support immediately touching the back side to prevent holes from forming when pressurized, and the material absorbs epoxies needed to attach it to such a support. A more durable substrate is recommended for any future work.

**REFERENCES:**

1. Yu, M., Funke, H. H., Noble, R. D., & Falconer, J. L. (2011). H(2) Separation Using Defect-Free, Inorganic Composite Membranes. *Journal of the American Chemical Society*, *133*(6), 4-6.

# Appendix D

As explained in Appendix C, this section contains a project summary NSF report on MLD composite membranes. It also covers some work on improving selectivity specificity of VOC sensors by coating the sensor material with a thin, porous MLD-grown film.

## NSF Report on MLD Composite Membranes – April 2017

### *Introduction*

The project goal was to prepare ultra-thin (<100 nm) microporous ceramic membranes that are highly selective for the separation of differently-sized small molecules because of their narrow pore size distribution. High fluxes were expected as a result of the thin separation layer and synthesis conditions were expected to affect both fluxes and selectivity and thus provide a means to fine-tune the membrane performance.

The membrane layers were formed by molecular layer deposition (MLD) where an inorganic/organic hybrid layer is grown on the surface of a porous support by sequential exposure to different precursors from the gas phase. The reaction of the gas-phase precursors with the functional groups on the membrane surface (OH, $CH_4$, etc.) is self-limiting and thus each deposition cycle increases the layer thickness by <0.5 nm. After completion of the deposition process, oxidation in air or water at elevated temperatures removes the organic segments of the hybrid layer, resulting in a porous inorganic film.

Previous work indicated that zeolite membranes (such as SAPO-34 membranes) with their small pores and narrow pore size distribution might provide ideal supports where the MLD later increases the intrinsic selectivity of the zeolite membranes for small molecules such as $H_2$ over $N_2$. The MLD pores are expected to be smaller than the zeolite pores (~0.4 nm).

***Results***

Alucone (Trimethylaluminum+Ethylene glycol) MLD films grown on SAPO-34 membranes. Several SAPO-34 membranes previously synthesized in our laboratory were exposed sequentially to trimethylaluminum (TMA) followed by ethylene glycol, resulting in a thin 'alucone' MLD film on the external surface of the zeolite crystals. After 30 MLD cycles, the membranes were heated in air to temperatures ranging from between 323 to 573 K to remove the organic components in the MLD layer and create the desired pore structure. The best membrane had a $H_2/N_2$ selectivity of 150 at 293 K for a feed pressure of 380 kPa and permeate pressure of 83 kPa. The $H_2/N_2$ selectivity of the SAPO-34 membranes without the MLD layer were about 8. The $H_2$ permeance decreased from $1x10^{-6}$ mol/($m^2$sPa) for the untreated membrane to about $7x10^{-8}$ mol/($m^2$sPa).

Even though the $H_2/N_2$ selectivity improved for all coated membranes, changes in the oxidation conditions (rate of heating, final temperature) to create the separation pores did not affect the separation performance reproducibly. Some membranes that had high selectivity after heating to lower temperatures (<473 K) showed a decrease in selectivity by >80% when they were reheated to higher temperatures likely because cracks in the separation layer and the SAPO-34 substructure formed due to thermal expansion mismatches. All membranes showed a significant decrease in flux after coating. Apparently, small differences in the SAPO-34 membrane morphology and differences in susceptibility to damage after repeated heating

affected the separation properties more than variations in the MLD film with changing synthesis conditions.

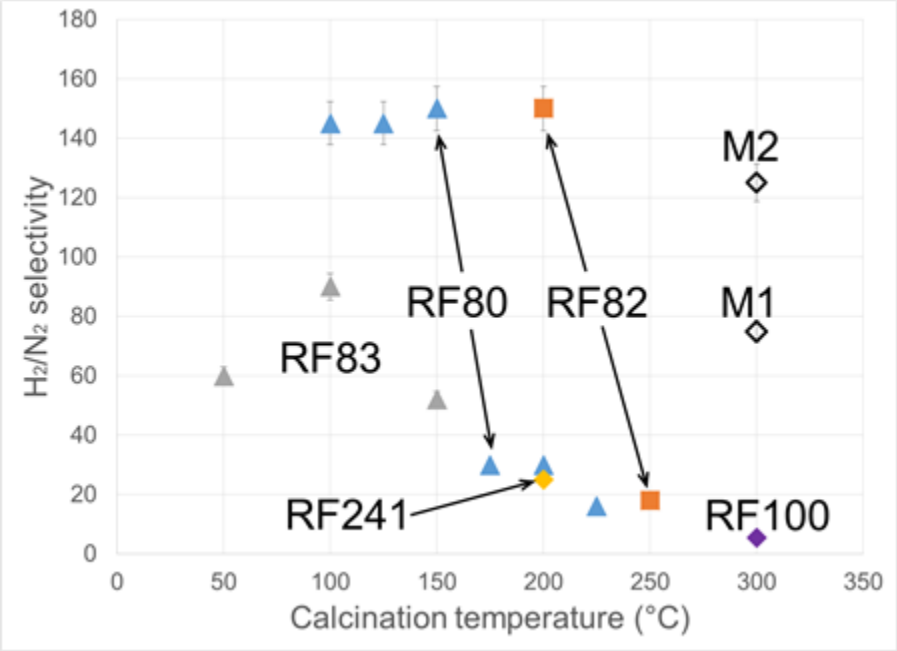


Figure 1: $H_2/N_2$ selectivity of Alucone-coated SAPO-34 membranes at different calcination temperatures

MLD-alucone grown on Novarials $TiO_2$ nanowire paper

Commercially available $TiO_2$ nanowire 'paper' (Novarials) was studied as a potential support materials for MLD membranes. Even though the pores of the Novarials material (~10-100 nm estimated based on the nanowire diameters) may be nominally small enough to be bridged by a sufficiently thick MLD film, all attempts to fill the three-dimensional irregular pore structure of the interlinked fibers by MLD to obtain a gas-tight film before oxidation were unsuccessful. In addition, the substrate was very brittle and could not be sealed directly with standard o-ring seals. Small fragments of the nanowire paper were thus glued with epoxy to ¼" VCR filter gaskets to obtain supports that could be coated with the MLD films and then sealed in a gas permeation module. Even 100 cycles (>50 nm) of MLD growth were not sufficient to fill

all gaps between the fibers likely because the larges pores were still more than two times larger than the MLD film thickness or because cracks formed as a result of thermal expansion mismatch between the substrate and the separation layer. The ideal selectivity of the coated films were close to Knudsen selectivity and thus, the remaining pores were still too large for size exclusion of small molecules (Table below). The overall thickness of the TiO2 paper was about 0.5 mm and thus, a dense MLD separation layer that would be obtained after filling most of the support pores would be too thick to provide high fluxes. Attempts to mask the inner porosity with a removable template so that MLD will only coat the external surface were abandoned due to a lack of feasible filler template materials.

| | Ideal Selectivity | Knudsen Selectivity |
|---|---|---|
| $H_2/N_2$ | 3.5 | 3.7 |
| $H_2/CH_4$ | 2.8 | 2.8 |
| $H_2/CO_2$ | 4.7 | 4.7 |
| $N_2/CH_4$ | 1.3 | 0.7 |
| $CH_4/CO_2$ | 1.7 | 1.7 |
| $N_2/CO_2$ | 1.3 | 1.3 |

Table 1: Composite membrane from MLD-alucone grown on Novarials $TiO_2$ nanowire paper

MLD-alucone grown on anodized aluminum oxide

Anodized aluminum oxide (AAO) membranes with pores ranging from 5 nm to several 100 nm are commercially available and could provide well-characterized uniform supports for MLD membranes. Synker, Inc. AAO membranes with 5 nm pores were thus used as supports for MLD films. Between 15 and 100 cycles of AB (TMA/ethylene glycol) or ABC (TMA/ethanol amine/maleic anhydride) MLD films were deposited to block the support pores. After 60 cycles

most membranes were impermeable to $N_2$ before calcination, suggesting that about 3 nm of growth is necessary to completely cover the 5 nm pores. However, after oxidation of the MLD film either with water at ambient temperature or with air at 534 K to form pores only Knudsen selectivity was found for all gas pairs studied (Table). In addition, the permeance for $H_2$ after oxidation was much higher than expected for a few nm thick MLD film and, within the accuracy of the measurement, close to the permeance of the uncoated support. Apparently, after oxidation, many cracks formed, possibly due to thermal expansion mismatch between the MLD film and the AAO support. In addition, previous studies have shown that during removal of the organic segment of the MLD films, significant shrinkage is possible and the formation of large defects may be the result of such shrinkage. SEM imaging indicated some larger cracks in the oxidized film but the results were not conclusive because the conductive coating material used for SEM (gold or carbon) can also crack, giving a false indication of a cracked substrate.

Another challenge is deposition in the larger support pores that could potentially result in a much larger film thickness than intended. Attempts to block access to the larger support pores on the opposite side of the AAO support with Teflon tape prior to deposition did improve the separation performance.

| Membrane | # MLD cycles | Calcinded (250C) | H2 perm | H2/N2 sel. | H2/CO2 sel. |
|---|---|---|---|---|---|
| 13 | 0 | No | 1.4E-04 | 3.4 | 4.0 |
| 7 | 15 | No | 1.2E-04 | - | 3.0 |
| 8 | 15 | Yes | 2.2E-04 | - | 4.3 |
| 10 | 30 | Yes | 2.1E-05 | - | 2.9 |
| 11 | 30* | No | 2.9E-04 | 3.7 | 4.4 |
| 12 | 30* | Yes | 7.7E-04 | 2.6 | 4.3 |
| 3 | 100 | No | 0 | - | - |
| 4 | 100 | Yes | 0 | - | - |

Table 2: MLD coated Synkera AAO membranes

MLD gas sensors

Semiconductor-based gas sensors (e.g $SnO_2$) are highly sensitive to organic molecules in air but are not very specific to different species. A selective membrane coating that could distinguish between small and large molecules thus has the potential to improve the specificity of such sensors. An MLD-coated gas sensor may also provide a means to characterize the MLD films by exposing the sensor to differently sized molecules. Organic components too large for the MLD pores would not be detected on the sensor surface and thus pore sizes cold be estimated. The sensors operate at elevated temperature (>423 K) and thus MLD coatings may behave differently than under ambient operating conditions. Initial results with MLD coated sensors provided by Synkera, Inc. show that increasing the coating thickness by increasing the number of cycles from 0-30 decreases the sensor response for small molecules such as CO and HCHO, but increases the response to the larger i-butane (Figure 2). These counterintuitive results suggest that the films do not provide any size exclusion but that the MLD deposition chemically alters the sensor surface by doping the semiconductor structure and thus changes the response to different chemical species differently.

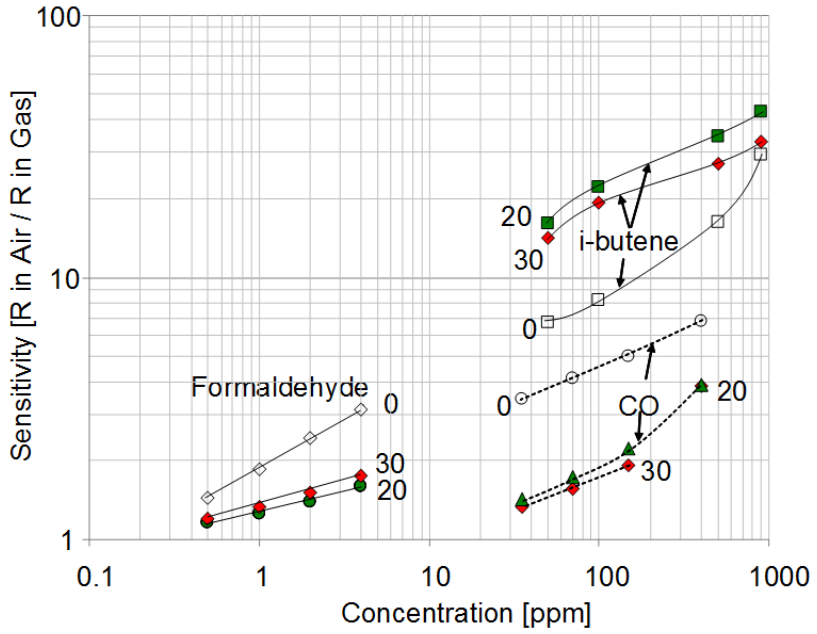


Figure 2: Response of MLD-coated Synkera Sensor to different organic molecules

**Summary**

Molecular layer deposition was used to grow microporous oxide films on several different substrates to obtain membranes that are selective for small gas molecules based on size. The MLD films improved the $H_2/N_2$ separation of SAPO-34, as previously reported and used as justification for the proposed work, but variation of the film deposition procedures did not provide a reproducible means to controllably alter the separation properties. Based on our findings, we conclude that subtle differences in the properties of the SAPO-34 membranes used as substrate have a larger influence on the final composite membrane properties than changes in the MLD deposition procedure. In addition recent results by other groups suggest that the initial premise wherein a thin MLD layer with smaller pores coated on the 0.4 nm zeolite pores improves the selectivity because of the smaller MLD pores may not be correct. The referenced work suggest that MLD pores are too large to distinguish between smaller molecules and the observed selectivity improvements are mainly due to stresses at the MLD/zeolite interface that

slightly distorts the zeolite pores and thus decreases their size, or by miss-matched zeolite/MLD-film pores.

Other substrates such as TiO2 nanowire paper or anodized alumina did not show improved selectivity after deposition of MLD layers because the substrate pores were too large to be covered by a continuous MLD film, and/or because cracks formed during oxidation of the MLD film that is required to form the pores for separation.